VNIVERSITAT ID VALÈNCIA

Facultad de Física

Departamento de Física Aplicada

Integration of Perylenediimides and metal nanoparticles in polymer waveguides for photonics

---

Ph.D. Thesis

Programa de Doctorado en Física

Author:
Mattia Signoretto

Supervisors:
Dr. Isaac Suárez
Prof. Juan P. Martínez Pastor

Valencia, September 2017

Acknowledgment

Resumen

Actualmente la implementación de nuevos dispositivos fotónicos capaces de integrar nuevas funcionalidades ópticas en dimensiones nanométricas despierta un gran interés. Por ello, la presente Tesis Doctoral propone desarrollar una nueva tecnología fotónica basada en la combinación de nanopartículas metálicas (MNPs) con moléculas orgánicas, en particular perilenos (PDI).

El objetivo principal de este trabajo ha sido la incorporación de PDI y/o MNPs en guías de ondas poliméricas, con el fin de usar sus propiedades activas/plasmónicas para construir nuevos dispositivos ópticos integrados. Para ello, en primer lugar, se explotaron las excelentes propiedades emisoras de luz de los PDI para demostrar amplificación óptica en guías de onda multicapa, demostrando un umbral tan bajo como 0,9 μJ y un ancho de línea de 2 *nm*. Paralelamente, se incorporaron MNPs en guías ópticas para aprovechar sus propiedades de dispersión de luz para acoplar ésta en el interior de guías ópticas en un amplio rango de longitud de onda (404-750 *nm*) con una eficiencia de hasta el 1 *%*. Posteriormente, se combinaron PDI y MNPs en este tipo de guías poliméricas para mejorar la emisión de luz de las moléculas orgánicas por medio de un proceso de acoplamiento débil excitón-plasmón; para este fin, la interacción se optimizó mediante los parámetros geométricos que rigen el acoplamiento PDI-MNPs obteniéndose un factor Purcell de hasta 10 cuando este sistema se integra en guía óptica. Finalmente, en esta Tesis Doctoral se propuso la implementación de un láser de realimentación aleatoria integrando MNPs con elevada sección transversal de dispersión junto con moléculas orgánicas (PDI) capaces de proveer la suficiente ganancia para obtener emisión estimulada. Este trabajo de

investigación condujo a tres publicaciones en revistas internacionales de primer cuartil, y un cuarto artículo que está en preparación.

Abstract

Currently there is a great concern to implement new photonic devices able to integrate several functionalities in nanoscale dimensions in a CMOs compatible platform. For this purpose, this Ph.D. project proposes to develop a new photonic technology based in the combination of metal nanoparticles (MNPs) with organic molecules, mainly perylenediimides (PDI) derivatives.

The main target of this Ph.D. was the incorporation of PDI-derivatives and/or MNPs into polymer waveguides in order to use their active/plasmonic properties to construct novel integrated optical devices. In this way, the excellent properties of PDI-derivatives were firstly exploited to demonstrate optical amplification in the single pass propagation of PL signal along the optical waveguide, with a demonstrated threshold as low as 0.9 *μJ* and a linewidth of 2 *nm*. In parallel, the high scattering cross section of MNPs was designed to couple light inside optical waveguides, demonstrating light coupling in a wide wavelength range (404-750 *nm*) with an efficiency up to 1 *%*. The combination of both PDI and MNPs integrated in polymer waveguides was used to enhance the emission of light of PDI by exciton-plasmon weak coupling; the interaction was optimized by the geometrical parameters of the PDI-MNPs coupling structures and by their integration in an optical waveguide, where a Purcell factor of 10 was achieved. Finally, a random distributed feedback laser was fabricated by integrating MNPs with high scattering cross section together with amplification of the stimulated emission by PDI. The present research work led to three peer-

reviewed publications in international journals of high impact factor, and a fourth

article is now under preparation.

Contents

1   Introducción (Castellano)

El nacimiento de la era moderna de las Telecomunicaciones Ópticas puede atribuirse al desarrollo de los láseres en 1958 y de las fibras ópticas en los años 90. Estos descubrimientos, junto a la utilización de las técnicas de fabricación microelectrónicas para implementar dispositivos ópticos semiconductores, han dado lugar a una nueva rama de la ciencia conocida como Fotónica [1]. Ejemplos de aplicaciones fotónicas incluyen la capacidad de transmitir y recibir información con velocidades de hasta 1 *Tbps* [2], la implementación de redes de comunicaciones totalmente ópticas [3], o la fabricación de sensores de alta sensibilidad [4]. Además, en los últimos años, la Plasmónica ha surgido como una nueva rama de la Fotónica capaz de manipulación la luz con nanoestructuras metálicas. Dicha rama se basa en el acoplamiento de la luz con los electrones libres presentes en la superficie metálica (o interface metal-dieléctrico) [5, 6]. Hoy en día, la plasmónica se está aplicando en una amplia gama de aplicaciones, como por ejemplo espectroscopia [7], absorción infrarroja [8], fluorescencia molecular [9, 10] y diagnóstico y fototerapia contra el cáncer [11].

1.1   Óptica Integrada

Las ventajas de la Fotónica se derivan de la alta velocidad y masa nula de los fotones, lo que permite procesar la información en el régimen de THz con un bajo tiempo de respuesta.

La Óptica Integrada es la rama de la Fotónica que trata de la incorporación de uno o varios dispositivos ópticos en el mismo substrato, de la misma manera que lo hace la Microelectrónica con circuitos y dispositivos electrónicos [1]. Así,

un circuito de óptica integrado ("photonic integrated circuit", PIC) es capaz de integrar una o varias funciones ópticas (emisión de luz, filtrado, modulación, acoplamiento, detección, etc.) en un "chip óptico", que sería el equivalente fotónico del Chip electrónico en Microelectrónica.

Sin embargo, la difracción de la luz limita las dimensiones de los dispositivos fotónicos a $\lambda/2n$, mientras que el tamaño critico de los componentes electrónicos han ido disminuyendo hasta los nanómetros [12], fabricación de transistores de $\approx 10\ nm$ obtenida hoy en día. De esta manera, la Plasmónica ha recibido mucha atención en los últimos años [13, 14], gracias a su capacidad de hacer unir las ventajas de ambas disciplinas: la Electrónica y la Fotónica. Es decir, mantener el rendimiento de velocidad de los dispositivos fotónicos, junto con las pequeñas dimensiones de los componentes electrónicos típicos [15].

1.1.1 Guía de ondas

Las guías de ondas son componentes indispensables para construir la mayoría de las funcionalidades de la Óptica Integrada. Una guía de ondas es una estructura óptica que permite el confinamiento y la propagación de la luz. Su implementación consiste en la utilización de dos o más materiales dieléctricos con diferente índice de refracción, de manera que la luz es confinada en la región de mayor índice de refracción (núcleo de la guía de ondas) por reflexión total interna [1]. Generalmente, la capa superior se denomina cubierta y la capa inferior substrato.

Las guías de onda se pueden clasificar en diferentes tipos dependiendo del confinamiento de la luz o de la variación del índice de refracción. De acuerdo con el confinamiento de la luz, las guías de onda se dividen en unidimensionales (guías de ondas planas) o bidimensionales. En el primer tipo (mostrado en la Figura 1(a) y (b)) el índice de refracción varía en la dirección perpendicular al

substrato, mientras que en el segundo tipo (mostrado en la Figura 1(c)) el índice de refracción varia en las dos direcciones. De esta manera, la propagación de la luz se mantiene confinada en una dirección mientras la densidad de potencia óptica se incrementa.
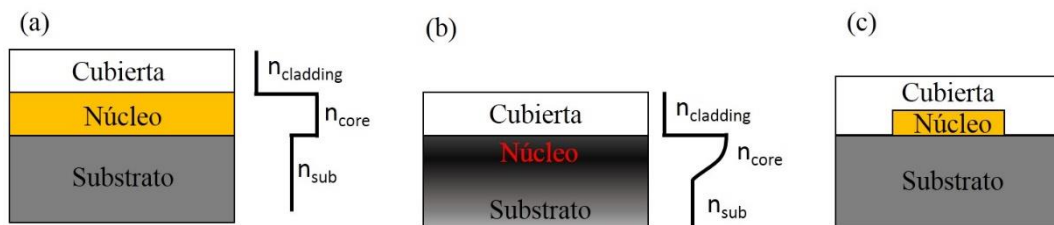
Figura 1. Esquema de (a) guía de ondas plana, (b) guía de ondas de índice gradual y (c) guía de ondas de salto de índice.

El perfil de índice de refracción se genera durante el proceso de fabricación de las guías de ondas. Por lo tanto, las guías de onda también se pueden clasificar de acuerdo con la variación del índice de refracción en guía de salto de índice (Figura 1(a)) y guías de onda de índice gradual (Figura 1(b)). Las guías de ondas de salto de índice están compuestas por capas uniformes con índice de refracción constante, en los que la capa central (núcleo de la guía de ondas) tiene un índice de refracción n_{core} mayor que los medios circundantes (n_{sub} y $n_{cladding}$). En los guías de ondas con perfil de índice gradual, el índice de refracción en el núcleo de la guía de ondas no es constante, sino que es (usualmente) máximo en la interfaz con la cubierta, y va disminuyendo progresivamente con la profundidad hasta llegar al valor del índice de refracción del substrato.

1.1.2 Guías de ondas activas y pasivas

Las guías de onda sirven como arquitectura base para implementar diferentes dispositivos ópticos integrados, como amplificadores [16], interferómetros [17] y divisores de haz [18], entre otros. Dichos dispositivos se pueden dividir en activos y pasivos, en función de si presentan o no la capacidad de generar luz. Un dispositivo pasivo la relación entre la entrada y la salida es fija,

tal y como ocurre en atenuadores o divisores de haz. Sin embargo, los dispositivos activos se caracterizan por la emisión de fotones cuando se bombean ópticamente o eléctricamente, como sucede en láseres y amplificadores ópticos.

En particular, la incorporación de materiales activos procesados en forma de disoluciones químicas (moléculas orgánicas luminiscentes [19-22], puntos cuánticos coloidales [23, 24], pozos cuánticos coloidales (nanoláminas) [25], perovskitas semiconductoras orgánicas e inorgánicas [26], etc.) para la fabricación de guías ópticas, ha demostrado una plataforma muy interesante para la integración de propiedades activas en diferentes tipos de substratos y plataformas [27].

1.2 Combinación de moléculas fotoluminiscentes y polímeros para la Óptica Integrada

Los polímeros son cadenas largas de moléculas monómeras orgánicas que, dependiendo del tipo de polímero, se unen para formar redes lineales, bidimensionales o tridimensionales. Estos materiales son particularmente atractivos para la óptica integrada debido a su relativamente buena estabilidad térmica, su transparencia en las regiones visible e infrarroja y su gran versatilidad tecnológica [2-4, 18]. Por ejemplo, una de las ventajas de los dispositivos basados en polímeros radica en su facilidad para ser depositados en forma de capas delgadas sobre una amplia variedad de substratos. Además, es posible cubrir grandes áreas a un costo relativamente bajo [28]. Otra ventaja es la posibilidad de hacer estructuras bidimensionales a través de técnicas litográficas, como la nanoimpresión [4], la fotolitografía UV [29] o la litografía por haz de electrones [30].

Por último, los polímeros pueden servir como mastrices de otros (nano)materiales, tales como colorantes o moléculas orgánicas fluorescentes [19-

22], puntos cuánticos [23, 24], o nanopartículas metálicas [31]. Esto tipo de "multi-material" recibe el nombre de "nanocomposite" [32] si al menos uno de sus componentes tiene dimensiones nanometricas [33]. Estos materiales artificiales presentan la ventaja de combinar las propiedades de los nanocomponentes con las flexibilidades tecnológicas de la matriz polimérica [34].

En particular, los "nanocomposites" formados por moléculas orgánicas embebidas en una matriz polimérica han suscitado un gran interés para la realización de dispositivos activos. Ejemplos de diferentes aplicaciones incluyen biosensores [32], OLEDs [35], OFETs [35], células solares [35], amplificadores ópticos [22] y láseres [19-21]. En consecuencia, el nanocomposite molécula-polímero se ha elegido como elemento activo para implementar los dispositivos propuestos en el presente trabajo de Tesis Doctoral.

1.2.1 Moléculas orgánicas fluorescentes

La estructura electrónica de las moléculas fluorescentes o fotoluminiscentes se corresponde al esquema general mostrado en la Figura 2. En el estado fundamental los electrones se asignan hasta ocupar el orbital molecular más alto ("highest occupied molecular orbital", HOMO). Estos estados electrónicos están separados por un intervalo de energía (Ep) del orbital molecular de más baja energía que no está ocupado ("lowest unoccupied molecular orbital", LUMO). En consecuencia, una molécula de este tipo puede absorber un fotón con energía $hv \geq E_p$ y así promover un electrón desde los estados HOMO a LUMO, lo que sería equivalente a la generación de un par electrón-hueco (excitón) en un semiconductor. Sucesivamente, este par electrón-hueco fotogenerado puede recombinarse radiativamente mediante la emisión de un fotón, proceso que se conoce con el nombre de fotoluminiscencia ("Photoluminescence", PL). Por

supuesto, el par electrón-hueco también puede perderse por recombinación no radiactiva desintegrándose mediante la emisión de fonones.
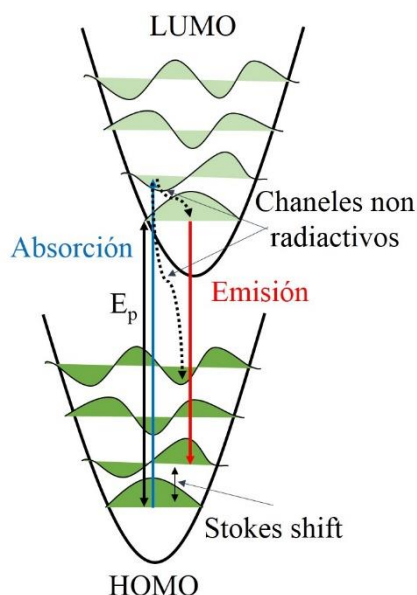
Figura 2. Ilustración esquemática del proceso de fotoluminiscencia en una molécula.

1.2.2 ¿Por qué Perilenos?

En esta Tesis Doctoral se eligieron los perilinos ("Perylenediimides", PDI) como elementos activos a incorporar en las guías de ondas. La Figura 3 muestra la estructura del dianhídrido perileno-3,4,9,10-tetracarboxílico (PTCDA), el cual puede considerarse como el padre de esta clase de compuestos primeramente obtenidos en 1913 [36].

Utilizando esta estructura molecular como punto de partida se han llegado a sintetizar una gran variedad de PDI. De hecho, con un procedimiento de síntesis adecuado, es posible fabricar compuestos con excelentes propiedades químicas y térmicas, alta estabilidad fotoquímica, rendimiento cuántico de FL/PL cercano a uno (todos los fotones absorbidos por el compuesto a una determinada longitud de onda se transforman en fotones emitidos a otra longitud de onda más larga), y un fuerte carácter como aceptor de electrones [37-46].

6
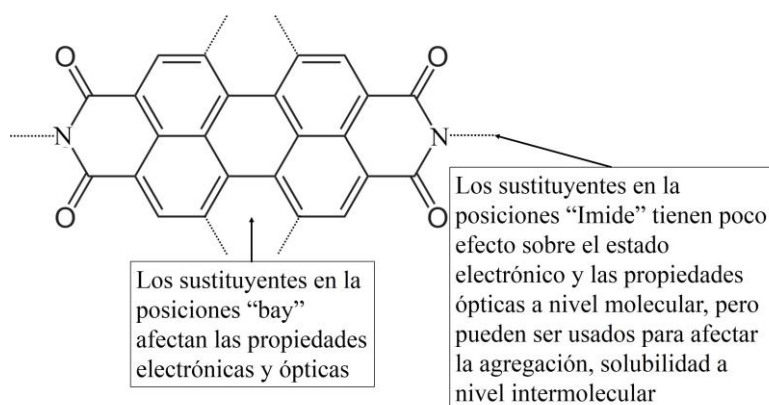
Figura 3. Estructura química del PTCDA. Se indica la posición típica en la que se colocan habitualmente los sustituyentes químicos y se describe su efecto.

Como consecuencia, los PDI son de gran interés para una amplia gama de aplicaciones, tales como células solares [47], transistores orgánicos [48], sensores ópticos [49] y láseres de estado sólido [50].

1.3   Algunos antecedentes sobre la Plasmonica

En el presente trabajo de Tesis Doctoral se propone la integración de nanopartículas metálicas ("metal nanoparticles", MNPs) en guías de ondas con el fin de explotar sus propiedades ópticas particulares en diversas aplicaciones fotónicas. De esta manera, esta sección describe las principales propiedades ópticas de estas nanopartículas.

1.3.1   ¿Qué es un plasmón?

Los polaritones de plasmón de superficie ("surface plasmon polaritons", SPPs) son excitaciones electromagnéticas que se propagan en la interfaz entre un dieléctrico y un metal, y están confinadas en la dirección perpendicular a esa interfaz por campos evanescentes. Estas ondas electromagnéticas superficiales surgen a través del acoplamiento de los campos electromagnéticos a las oscilaciones del plasma de electrones en el metal [51].
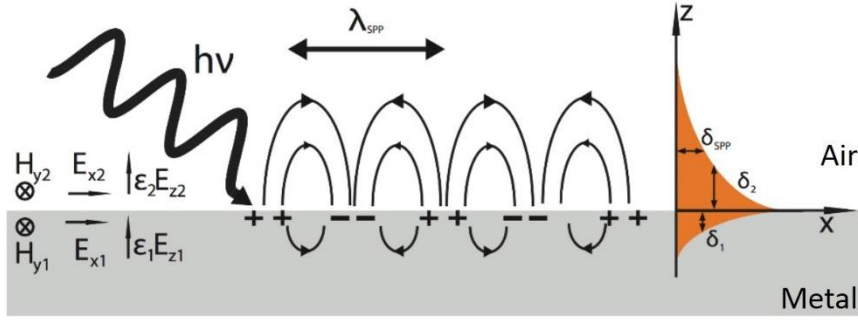
Figura 4. Ilustración esquemática de la propagación SPP en una sola interfaz entre un metal y un dieléctrico.

La geometría más simple para estudiar el SPP es una interfaz plana (Figura 4) entre un medio dieléctrico no absorbente ($z > 0$ en la Figura 4), caracterizada por una constante dieléctrica real y positiva ε_2, y el medio adyacente ($z < 0$ en la Figura 4), normalmente un metal, descrito a través de una función dieléctrica compleja $\varepsilon_1(\omega)$, con parte real negativa y parte imaginaria positiva. Para los metales esta condición ($Re[\varepsilon_1(\omega)] < 0$) se cumple a frecuencias por debajo de la frecuencia de plasmón ω_p definida como [51]:

$$\omega_p = \sqrt{\frac{ne^2}{\varepsilon_0 m}}$$

(1.1)

donde ε_0 es la permitividad dieléctrica del vacío, n la densidad de electrones, e la carga elemental de los electrones y m su masa efectiva en el metal.

En el caso de las nanopartículas metálicas, el acoplamiento entre electrones libres y un campo electromagnético externo da lugar a una excitación no propagante nominada Resonancia de Plasmon Superficial Localizada ("Localized Surface Plasmons Resonance", LSPR), tal como se ilustra esquemáticamente en la Figura 5. Estas oscilaciones se pueden estudiar analizando la dispersión de luz producida por una nanopartícula pequeña (menor a la de longitud de onda) [51]. Así, la superficie curvada de estas nanopartículas ejerce una fuerza de

restauración efectiva sobre los electrones, produciendo así una resonancia que resulta en la amplificación del campo electromagnético cercano a la nanoestructura metálica [51].
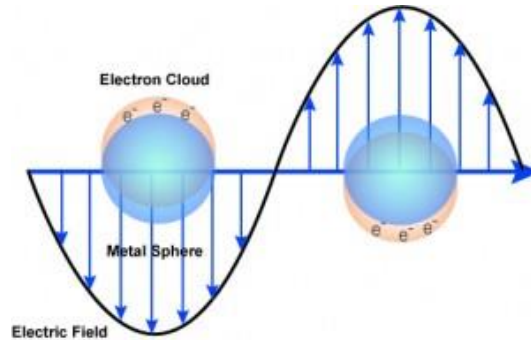
Figura 5. Ilustración del LSPR en una nanoesfera metálica.

Un parámetro importante para estudiar las MNPs es su polarizabilidad, α. En el caso de nanopartículas metálicas esféricas que presentan un tamaño mucho menor que la longitud de onda de la luz usada para inducir el LSPR, las oscilaciones de plasmón de superficie están dominadas por el modo dipolar, y por tanto la polarizabilidad se puede calcular, en base a la teoría de Mie, a partir de la ecuación [5]:

$$\alpha = 3\varepsilon_0 V \left(\frac{\varepsilon_1 - \varepsilon_m}{\varepsilon_1 + 2\varepsilon_m} \right)$$

(1.2)

donde V es el volumen de partículas, $\varepsilon_1(\omega) = \varepsilon_r(\omega) + i\varepsilon_i(\omega)$ es la función dieléctrica compleja del metal (dependiente de la frecuencia), y ε_m es la constante dieléctrica del medio circundante. La frecuencia de resonancia se define cuando se cumple la condición $\varepsilon_r(\omega_{SPR}) = -2\varepsilon_m$ (es decir, α tiende a infinito). Para el oro (Au), la plata (Ag) y el cobre (Cu), esta condición se cumple en el rango de longitudes de onda del visible [5] y, por tanto, estos metales son una opción apropiada para aplicaciones ópticas.

1.3.2 Propiedades/aplicaciones de las nanoparticolas plasmónicas

Las nanopartículas metálicas presentan unas peculiares propiedades ópticas derivadas de la física descrita anteriormente:

(i) Su elevada sección transversal de dispersión y absorción se ha usado para mejorar la eficiencia de células solares [52, 53], o para acoplar la luz en guías de onda [54, 55]. Además, en los últimos años, esta propiedad también se ha propuesto como medio de realimentación aleatorio ("random distributed feedback") en dispositivos láser [56-59].

(ii) La frecuencia o longitud de onda del LSPR no sólo depende del material metálico, sino también del tamaño y forma de la nanopartícula, de las propiedades dieléctricas del medio circundante y del nivel del acoplamiento entre nanopartículas [60-64]. Por lo tanto, hay muchos grados de libertad para afinar sus propiedades ópticas y adecuarlas para una aplicación determinada.

(iii) El LSPR es muy sensible a los cambios en la constante dieléctrica del medio circundante (véase la ecuación 1.2), por lo que las MNPs han sido intensamente estudiadas para aplicaciones en detección de compuestos químicos y biológicos [65, 66].

(iv) Las MNPs presentan un campo cercano muy alto, lo que puede conducir a un fuerte aumento de la intensidad de la luz emitida por moléculas integradas en sus proximidades [67]. Las aplicaciones incluyen mejoría en la fluorescencia, mejora de la señal Raman [68], diagnóstico y terapia del cáncer [11], imágenes [69, 70] y terapias biomédicas [71, 72].

Además, la síntesis de las MNPs, especialmente Ag y Au, permite obtener biocompatibilidad [73] y una amplia gama de tamaños y formas [74], sobre una gran variedad de ligandos químicos y biomoleculares [75], lo que da llegar a una alta flexibilidad y estabilidad (foto)química.

1.4 Objetivos de la Tesis

El objetivo principal de esta Tesis Doctoral es la incorporación de moléculas orgánicas tipo perileno (PDI) y/o MNPs en guías de ondas poliméricas con el fin de usar sus propiedades activas/plasmónicas para construir nuevos dispositivos ópticos integrados. De esta manera, en primer lugar, se explotaron las excelentes propiedades emisoras de los PDI para demostrar amplificación. Paralelamente, se incorporaron MNPs dentro de guías de onda para aprovechar sus propiedades dispersoras para acoplar luz dentro de guías de onda. Posteriormente, se combinaron PDI y MNPs dentro de las guías de ondas poliméricas para mejorar la emisión de luz de las moléculas orgánicas por medio de un proceso der acoplamiento débil excitón-plasmón. Finalmente, esta Tesis Doctoral propone la implementación de un láser de realimentación aleatoria integrando MNPs con elevada sección transversal de dispersión junto con moléculas orgánicas (PDI) capaces de proveer emisión estimulada.

Con todo ello, en la presente Tesis Doctoral se propone una nueva tecnología para integrar funcionalidades activas (emisión de luz, amplificación o láser) en tecnología de silicio, aunque también puede ser la base para el desarrollo futuro de arquitecturas fotónicas integradas sobre substratos flexibles. Para ello, se han usado un nuevo tipo de moléculas orgánicas y se han propuesto nuevas configuraciones (plasmónica) capaces de mejorar las funcionalidades ya existentes sin complicar excesivamente la arquitectura fotónica.

1.4.1 Objetivos específicos

- Fabricación y caracterización de guías de onda, que contienen PDI dispersos en Poli(metacrilato de metilo) (PMMA). Para ello, se desarrolló una nueva guía de ondas consistente en una capa de PMMA altamente dopada con PDI, intercalado entre dos capas de PMMA sin dopar. Esta estructura demostró las mejores condiciones para obtener amplificación de la emisión espontánea, ya que permite obtener unas condiciones óptimas de generación/propagación de la luz. Esta configuración puede servir como base para un futuro prototipo de amplificador óptico.

- Integración de MNPs en guías de onda. Para ello, las nanopartículas metálicas se han incorporado dentro de los polímeros por dos métodos de fabricación diferentes: crecimiento in situ de nanopartículas de oro en la fotoresina comercial Novolak, y por goteo de nanopartículas de plata comerciales de 100 nm en diámetro. Estos métodos son más simples y económicos de implementar que otros, como el uso de litografía de haz de electrones para definir patrones metálicos a escala nanométrica.

- Acoplamiento de luz en guías de onda integrada con MNPs con elevada eficiencia de dispersión para redireccionar la luz que incide perpendicularmente sobre su superficie hacia modos guiados. El acoplador óptico propuesto es igualmente simple y económico en comparación a otros más estándar, como el uso de redes de difracción grabadas en la guía por litografía óptica de alta resolución o de haz de electrones.

- Estudio del acoplamiento débil entre la luz emitida por los PDI y la LSPR de las nanopartículas de plata para así demostrar la mejora de la

emisión de luz. Para ello, los parámetros geométricos se han seleccionado adecuadamente para optimizar dicha interacción. Asimismo, el sistema PDI-MNPs se ha integrado dentro de una estructura de guía de ondas con el fin de mejorar dicho acoplamiento con el alto confinamiento de la luz dentro de la guía. Aquí queremos demostrar el beneficio de usar una guía de ondas para estudiar la interacción excitón-plasmón, que se podría incrementar por el mayor confinamiento de la luz.

- Demostrar generación laser utilizando MNPs como medio capaz de proveer una realimentación aleatoria a la emisión (amplificada) de los PDI.

1.5 Publicaciones asociadas a la presente Tesis

Esta Tesis Doctoral ha dado lugar a tres publicaciones en revistas internacionales de alto factor de impacto (primer cuartil) en las que el doctorando es primer autor, y un cuarto artículo que está en preparación. Estas publicaciones están relacionadas con los objetivos de esta Tesis doctoral explicados en la sección anterior, y muestran los resultados más importantes, que se resumirán más adelante (capítulo 3).

En primer lugar, se ha demostrado con éxito la amplificación óptica utilizando un nuevo tipo de guía de ondas plana activa. La estructura consistía en un nanocompuesto de PMMA-PDI altamente dopado depositado entre dos capas de PMMA. Este diseño permite demostrar la generación de ganancia óptica mediante la propagación con pérdidas bajas del láser de excitación dentro de la guía de ondas y el alto confinamiento de la PL dentro de la capa activa. Estos resultados se resumen en la sección 3.1 y se han publicado en la revista *ACS*

photonics (factor de impacto 6.756 en 2016 y clasificado 7/92 en la categoría Optics JCR) con título "**Efficient Optical Amplification in a Sandwich-Type Active-Passive Polymer Waveguide Containing Perylenediimides**". El trabajo se incluye en el anexo de la presente Tesis y se cita como referencia [76]. La participación del alumno en este trabajo consistió en la caracterización óptica de los PDI en disoluciones (absorción, PL y TRPL), fabricación y caracterización óptica de los nanocomposites (absorción, PL y TRPL), y fabricación y caracterización de la estructura de la guía de ondas (amplificación de luz, PL guiado, TRPL y estabilidad de la ASE).

Paralelamente, el estudiante desarrolló el nuevo proceso tecnológico apropiado para incorporar MNPs en guías de ondas, con el fin de explotar sus inusuales propiedades ópticas (elevada sección eficaz de dispersión debido a la resonancia plasmónica) para aplicaciones fotónicas. Para ello, se estudió inicialmente un crecimiento "in situ" de MNPs de oro embebido en la fotoresina comercial Novolak. Este método permite seleccionar las propiedades ópticas del nanocomposite plasmónico mediante un adecuado control del tamaño y la concentración de las MNPs dentro de la matriz. A continuación, se analizó, tanto experimental como numéricamente, el índice de refracción del "nanocomposite" Novolak-MNPs. De esta manera se encontraron las condiciones de fabricación apropiadas (factor de llenado y tiempo de crecimiento) para optimizar la dispersión a la longitud de onda deseada. Finalmente, el "nanocomposite" se integró dentro de una guía de ondas de PMMA para explotar sus propiedades de dispersión con el fin de acoplar luz dentro de la estructura. Dicho acoplamiento de luz se demostró experimentalmente en un amplio rango de longitudes de onda (404-780 *nm*) que inciden perpendicularmente sobre la superficie de la estructura.

Estos resultados se resumen en la sección 3.2 de esta Tesis doctoral y se han publicado en la revista *Nanotechnology* (factor de impacto 3.821 en 2014 clasificado 24/145 en Física Aplicada) con título "**Polymer waveguide couplers based on metal nanoparticle-polymer nanocomposites**". El artículo se adjunta en el anexo de la presente Tesis y se cita como referencia [77]. La participación del alumno en esta publicación consistió en la fabricación de los diferentes "nanocomposites" y de guías de onda basadas en éstos, caracterización óptica y microscópica de los dispositivos (transmisión/reflectividad, imágenes SEM, eficiencia de acoplamiento, etc.) y cálculo del índice de refracción efectivo en la estructura.

En el paso siguiente, el nanocomposite PDI-PMMA se integró junto con nanopartículas de plata de 100 *nm* de diámetro con el fin de estudiar la interacción entre ambos materiales. Para ello, se optimizó adecuadamente una tecnología para depositar capas homogéneas de MNPs. Posteriormente, se estudió la interacción entre las nanopartículas plamónicas y las moléculas de PDI con el objetivo de las mejorar la emisión de PL mediante un acoplamiento débil excitón-plasmón. Finalmente, el sistema MNPs-PDI se integró en una estructura de guía de ondas con el fin de mejorar esta interacción bajo condiciones de relativamente alto confinamiento de luz. De esta manera, se ha demostrado con éxito un factor de Purcell mayor que 10 cuando se mide en la cara de salida de la guía. Estos resultados se han resumido en la sección 3.3.1 de esta Tesis y forman parte del documento titulado **"Purcell-enhancement of the radiative PL decay in perylenediimides by coupling with silver nanoparticles into waveguide modes"**. El artículo ha sido recientemente publicado en la revista *Applied Physics Letters* (factor de impacto 3.411 in 2016, clasificado 28/147 en Física Aplicada),

que también se adjunta en el Anexo de la presente Tesis y se cita como referencia [78]. La participación del alumno en este trabajo consistió en la fabricación de los dispositivos, la caracterización óptica y el análisis de los datos PL y TRPL, así como el cálculo de la mejora Purcell en función de la separación entre la molécula de PDI y las MNPs.

Por último, se integraron conjuntamente MNPs de plata y PDI con el fin de demostrar la operación de láser en condiciones de realimentación aleatoria ("random distributed feedback"). Estos resultados se resumen en la sección 3.3.2 de esta Tesis Doctoral y se espera que se publiquen en breve. La participación del alumno en este trabajo consistió en la realización de los dispositivos, las mediciones de caracterización óptica (espectros de PL) y el modelado de la curva láser.

1   Introduction (English)

The birth of the modern era of Optical Telecommunications can be attributed to the development of lasers in 1958 and optical fibres in the 90s. These discoveries, together with the application of advanced microelectronics fabrication techniques in the implementation of semiconductor optical devices, have resulted in a new branch of science known as photonics [1]. Examples of photonic applications include the ability to transmit and receive information with speeds up to 1 *Tbps* [2], the implementation of fully optical communications networks [3], or the fabrication of high sensitivity sensors [4]. Furthermore, in recent years, Plasmonic emerged as a new branch of Photonics. This new discipline deals with the generation, control, manipulation, and transmission of excitations in metal structures. These excitations primarily arise by the coupling of light with free electrons excitations at the metal surface [5, 6]. Nowadays plasmonic is being applied in a broad range of applications. For example, surface enhanced spectroscopy [7], surface-enhanced infrared absorption [8] molecular fluorescence [9, 10], cancer diagnosis and therapy [11].

1.1   Integrated optics

The high speed of photonics derives from the use of photons, instead of electrons, for the transmission and processing of the information. In this way, by replacing electrons with photons, the system performance, such as bandwidth and speed processing, increases since photons travel at the speed of light.

Integrated Optics is a field of Photonics, which consist of the fabrication of one or several devices on the same substrate, in the same way as Microelectronic does with electric circuits [1]. Thus, a photonic integrate circuit (PIC) consists of the implementation of one or several optical functions (light emission, filtering, modulation, coupling, detection, etc.) integrated in one "optical chip", which would be the photonic equivalent of the electronic chip in microelectronics.

However, dimensions of photonic devices are limited by the light diffraction limit to *λ/2n*, while typical critical dimensions of electronic components are being decreased down to the nanometers (*nm*) scale [12]. In this way, plasmonics has received a lot of attention in the last years [13, 14], thanks to its ability of joining the advantages of both disciplines, electronics and photonics, i.e. keeping the speed performance of photonics devices together with the small dimensions in typical electronic components [15].

1.1.1 Waveguides

Optical waveguides are key technology components to build most functionalities in Integrated Optics. A waveguide is an optical structure that allows the confinement and propagation of light. It is usually fabricated by two or more dielectric materials with different refractive indexes. In this way, the light can be confined in the region with the higher refractive index (core of the waveguide) by internal total refraction [1]. Generally, the upper layer is called cladding and the lower one is usually a thick substrate (even if a dielectric film can be deposited onto this substrate previously to the waveguide material to meet the index contrast requirement, as in the case of using a silicon substrate).

Waveguides can be classified into different types depending on the confinement of light or on the variation of the refractive index. According to the

confinement of the light, the waveguides are divided into one-dimensional (planar waveguides) or two-dimensional (strip waveguide). In the first type, show in Figure 1(a) and (b), the refractive index is varied in one direction, while in the second type, show in Figure 1(c), the refractive index is changed in two directions. In this way, the light is propagated in one direction (perpendicular to the figure) and the optical power density is increased.
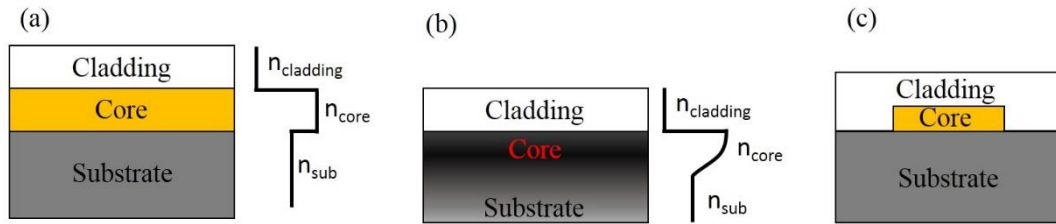
Figure 1. Scheme of (a) slab waveguide, (b) graded-index waveguide and (c) strip waveguide.

The refractive index profile is generated during the manufacturing process of the waveguides. Therefore, waveguides can also be classified according to the variation of refractive index into: step index waveguides (Figure 1(a) and (c)) and graded-index waveguide (Figure 1(b)). Step index waveguides are composed by uniform layers with constant refractive index. The central layer is the core of the waveguide and has a refractive index n_{core} greater than the ones of the surrounding medium (n_{sub} and $n_{cladding}$). In waveguides with graded-index profile, the refractive index in the waveguide core is not constant, usually being maximum at the interface with the cladding and decreasing progressively with depth, until it reaches the value of the refractive index of the substrate.

1.1.2 Active and passive waveguides

Different integrated optical devices can be fabricated by using waveguides, such as amplifiers [16], interferometers [17], beam splitters [18], as the most relevant ones. Such devices can be divided into passive and active. In a passive

19

device the relationship between the input and the output is fixed, as for example in an attenuator or a beam splitter. However, active devices are characterized by their own generation of light when they are optically or electrically pumped. In this case the waveguide will form part of very well-known devices, as lasers and optical amplifiers.

In particular, the incorporation of active solution processed materials (luminescent organic molecules [19-22], colloidal quantum dots [23, 24], colloidal quantum wells (nanoplateletes) [25], organic-inorganic semiconducting perovskites [26], etc.) into optical waveguides provides a suitable platform for on-chip integration of amplifiers and lasers [27].

1.2 Combination of photoluminescent molecules and polymers for integrated optics

Polymers are long chains of organic monomeric molecules, which join together to form linear, two-dimensional or three-dimensional lattices, depending on the type of polymer. Among all materials, they are particularly attractive for integrated optics because of their relatively good thermal stability, their transparency in the visible and infrared regions and their great technological versatility [2-4, 18].

One of the advantages of the polymer-based devices lies in their facility to be deposited in the form of thin layers on a wide variety of substrates. In addition, it is possible to cover large areas at a relatively low cost [28]. Another advantage is the possibility of making two-dimensional structures through lithographic techniques, such as nanoimprint [4], UV photolithography [29] or electron beam lithography [30].

Finally, polymers can act as a matrix for organic/inorganic (nano)materials, such as dyes [19-22], quantum dots [23, 24], or metal nanoparticles [31]. This sort of multicomponent materials is called nanocomposites [32] because at least one of the components present nanometer dimension [33]. These composites have the advantage of combining the properties of the nano-components with the technological feasibilities of the polymeric matrix [34].

In particular, nanocomposites formed by organic molecules embedded in a polymer matrix are of great interest for the realization of active devices. In fact, different applications have already been demonstrated with such multicomponent materials such as biosensors [32], OLEDs [35], OFETs [35], solar cells [35], amplifier [22] and lasers [19-21]. Therefore, such a molecule-polymer composites was chosen as the active elements in the devices produced in the present Ph.D. Thesis work.

1.2.1 Photoluminescent organic molecules

A typical molecule vibronic structure can be observed in Figure 2. At the ground state electrons are allocated up to the highest occupied molecular orbital (HOMO). These valence electron states are separated by an energy gap (E_p) from the lowest unoccupied molecular orbital (LUMO). Consequently, a photon with energy $h\nu \geq E_p$ can be absorbed by such a molecule to promote an electron from HOMO to LUMO states and hence determining an electron-hole pair. Successively, this photogenerated electron-hole pair can recombine in a radiative way by emitting a photon, which is called fluorescence (FL) or photoluminescence (PL). Of course the electron-hole pair can also find non-radiative paths to disintegrate by emitting phonons.
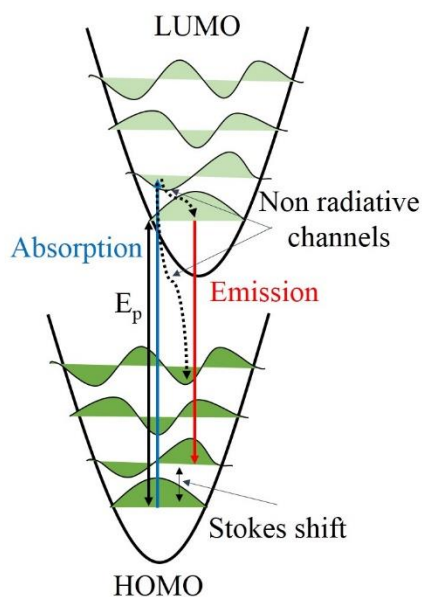
Figure 2. Schematic illustration of the photoluminescence process in molecule.

1.2.2 Why Perylenediimides?

In this Thesis Perylenediimide dye molecules (PDI) were chosen as the active elements to be incorporated into the optical waveguides. Figure 3 shows the structure of perylene-3,4,9,10-tetracarboxylic dianhydride (PTCDA), which can be considered as the father of this class of compounds firstly obtained in 1913 [36].
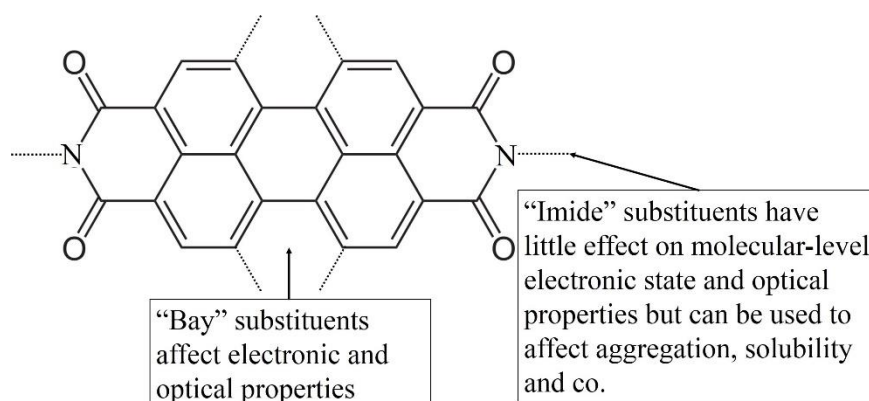
Figure 3. Chemical structure of PTCDA. Typical position where chemical substituents are usually placed are indicated and their effect described.

By using this structure as a starting point, a huge variety of PDI-derivatives have been properly fabricated. Indeed, with the right synthesis procedure, it

becomes possible to obtain PDI compounds with excellent chemical and thermal properties, high photochemical stability, near-unity FL/PL quantum yield and strong electron-acceptor character [37-46].

As a consequence, PDI are of great interest for a wide range of applications, such as solar cells [47], organic transistors [48], optical sensors [49] and solid state lasers [50].

1.3   Some background on Plasmonics

In the present Ph.D. work, we propose the integration of metal nanoparticles (MNPs) into optical waveguides in order to exploit their unusual optical properties for photonic applications. In this way, this section describes the main optical properties of these nanoparticles.

1.3.1   What is a plasmon?
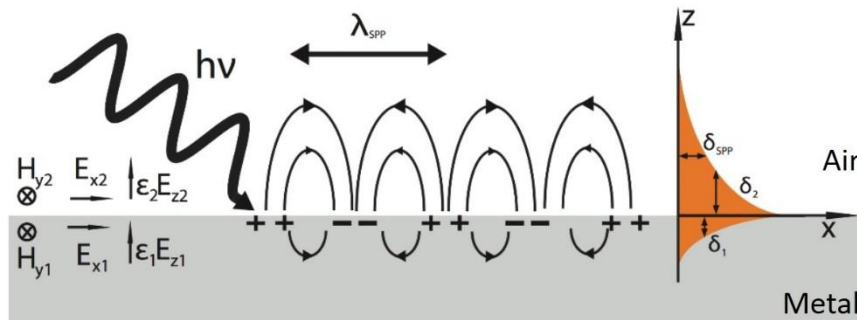
Figure 4. Schematic illustration of the SPP propagation at a single interface between a metal and a dielectric.

Surface plasmon polaritons (SPPs) are electromagnetic excitations propagating at the interface between a dielectric and a metal, evanescently confined in the perpendicular direction to this interface. These electromagnetic surface waves arise via the coupling of the electromagnetic fields to the oscillations of the electron plasma in the metal [51].

The simplest geometry is a flat interface (Figure 4) between a non-absorbing dielectric medium ($z > 0$ in Figure 4), characterized by a real and positive dielectric constant ε_2, and an adjacent media ($z < 0$ in Figure 4), usually a metal, described via a complex dielectric function $\varepsilon_1(\omega)$, with negative real and positive imaginary parts. For metals this condition ($Re[\varepsilon_1(\omega)] < 0$) is fulfilled at frequencies below the bulk plasmon frequency ω_p defined as [51]:

$$\omega_p = \sqrt{\frac{ne^2}{\varepsilon_0 m}}$$

(1.1)

where ε_0 is the vacuum dielectric permittivity, n the density of electrons, e the elemental electron charge and m its effective mass in the metal.
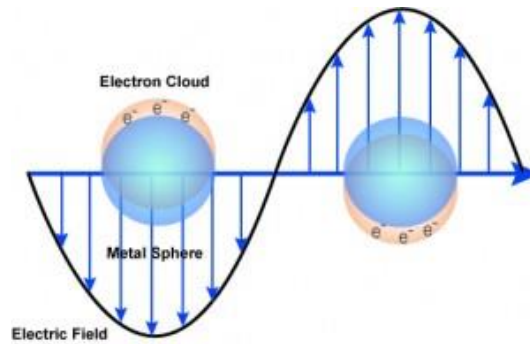
Figure 5. Sketch of the LSPR on a metallic sphere.

In the case of metallic nanostructures the coupling between free electrons and an external electromagnetic field gives rise to a non-propagating excitation called "Localized Surface Plasmons Resonance" (LSPR), as schematic illustrated in Figure 5. These electron oscillations arise naturally from the scattering problem of a small, sub-wavelength, metal nanoparticle in an oscillating electromagnetic field [51]. The curved surface of these particles exerts an effective restoring force

on the driven electrons, so that a resonance can arise, leading to electric field amplification [51].

An important parameter to study MNPs is their polarizability, α. For spherical metal nanoparticles whose size is much smaller than the excitation of the LSPR, the dipolar mode, dominates the surface plasmon oscillations and the polarizability can be calculated, on the base of Mie theory, from the following equation [5]:

$$\alpha = 3\varepsilon_0 V \left(\frac{\varepsilon_1 - \varepsilon_m}{\varepsilon_1 + 2\varepsilon_m} \right)$$

(1.2)

where V is the particle volume, $\varepsilon_1(\omega) = \varepsilon_r(\omega) + i\varepsilon_i(\omega)$ is the complex frequency-dependent dielectric function of the metal and ε_m is the dielectric constant of the surrounding medium. The LSPR frequency is defined when fulfilled the condition $\varepsilon_r(\omega_{SPR}) = -2\varepsilon_m$ (i.e. the magnitude of α tends to infinite). For gold (Au), silver (Ag), and copper (Cu), this resonance condition is fulfilled at visible frequencies [5], making them the appropriate choice for optical applications.

1.3.2 Properties/applications of plasmonic nanostructures

Metal nanostructures present several peculiar optical properties associated to the above described physics:

(i) The high scattering and absorption cross section of MNPs have been widely used to improve the efficiency of solar cells by light trapping [52, 53] or to couple light inside waveguide structures [54, 55]. Also, in the last years, this property is also used to provide the distributed feedback signal in random laser devices [56-59].

(ii) The LSPR frequency/wavelength depends not only on the metal, but also on the size and shape of the nanoparticle/nanostructure, the dielectric properties of the surrounding medium and inter-nanoparticle coupling interactions [60-64]; therefore, there are many degrees of freedom to tune the optical properties of the nanoparticles.

(iii) The LSPR is highly sensitive to changes in the dielectric constant of the surrounding medium (see equation 1.2), and hence MNPs have been intensively studied for chemo- and bio- sensing [65, 66].

(iv) The large local electric field in close proximity of the MNPs can lead to a strong enhancement of the spectroscopic signal from molecules in the vicinity of the nanoparticles [67]. Applications include plasmon-enhanced fluorescence, enhance of the Raman signal [68], cancer diagnosis and therapy [11], imaging [69, 70] and biomedical therapeutics [71, 72].

Furthermore, MNPs, especially Ag and Au, can be easily and bio-compatibly [73] synthesized in a huge range of sizes and shapes [74], with easy routes for surface conjugation to a variety of chemical and biomolecular ligands [75] and they usually present high (photo)chemical stability.

1.4 Objectives of the Thesis

The main target of this Ph.D. Thesis is the incorporation of PDI-derivatives and/or MNPs into polymer waveguides in order to use their active/plasmonic properties to construct novel integrated optical devices. In this way, the excellent properties of PDI-derivates were firstly exploited to demonstrate optical amplification. In parallel, the high scattering cross section of the MNPs was

designed to couple light inside optical waveguides. The combination of both PDI and MNPs integrated in polymer waveguides was used to enhance the emission of light of PDI by exciton-plasmon weak coupling. Finally, a random distributed feedback laser was fabricated by integrating MNPs with high scattering cross section together with amplification of the stimulated emission by PDI.

Therefore, in this Ph. D. Thesis a new technology is proposed to integrate active functionalities (light emission, amplification or laser) in silicon technology, although it can also be the basis for the future development of integrated photonic architectures on flexible substrates. To this end, a new type of organic molecules has been used and new configurations (plasmonics) have been proposed, capable of improving existing functionalities without excessively complicating the photonic architecture.

1.4.1   Specific objectives

- Fabrication and characterization of waveguides, containing PDI-derivatives dispersed in Poly(methyl methacrylate) (PMMA). A novel waveguide consisting of a highly doped PMMA-PDI nanocomposite sandwiched between two PMMA cladding layers demonstrated the best conditions to obtain amplification of the spontaneous emission in the single pass propagation of PL signal along the waveguide. This structure showed the best conditions to obtain amplification of the spontaneous emission, since it allows to obtain the optimum conditions for the generation / propagation of light. This configuration can serve as a basis for a future prototype of an optical amplifier.

- Integration of MNPs in waveguide structures. For this purpose, metal nanoparticles have been incorporated in polymers by two different

fabrication methods: in situ grown of gold nanoparticles in the commercial photoresist Novolak and drop casting of silver nanoparticles. These methods are simpler and cheaper to implement than others, such as the use of electron beam lithography to define metallic patterns at the nanoscale.

- Coupling of normal incident light into the waveguide core (PMMA) by exploiting the high scattering cross sections of Au MNPs. The proposed optical coupler is simple and economical as compared to other more standard ones, such as the use of diffraction gratings recorded in the guide by high resolution optical or electron beam lithographies.

- Study the weak coupling between the light emitted by PDI and the LSPR of silver nanoparticles in order to demonstrate their PL enhancement. For this purpose, the interaction is optimized by the geometrical parameters of the PDI-MNPs coupling structures and by their integration in an optical waveguide. Here we want to demonstrate the benefit of using a waveguide to study the exciton-plasmon interaction, which could be increased by a higher confinement of light.

- Exploit the high scattering cross section of nanoparticles to provide a random distributed feedback to the PDI PL. In these conditions, the amplification of spontaneous emission (ASE) of the PDI results in laser operation. For this purpose, Ag nanoparticles were integrated appropriately with the active material nanocomposite (PMMA-PDI).

1.5 Publications associated to the present Thesis

This Ph.D. Thesis led to three peer-reviewed publications in international journals, and a fourth article is now under preparation. These publications are

related with the objectives of this Ph.D. Thesis explained in the previous section, and provides the most important results (explain in chapter 3).

First, the optical amplification has been successfully demonstrated by using a novel planar active waveguide. The structure consisted of a highly doped PMMA-PDI sandwiched between two PMMA films. The generation of optical gain was demonstrated by the propagation of the laser excitation inside the waveguide structure with low losses and a high confinement of generated PL in the active layer. These results are explained in sections 3.1 and have been published in the paper entitled "**Efficient Optical Amplification in a Sandwich-Type Active-Passive Polymer Waveguide Containing Perylenediimides**" published in *ACS photonics* (impact factor 6.756 in 2016 and ranked 7/92 in the Optics JCR-category). The paper is included in the annex of the present Thesis and it is cited as reference [76]. The participation of the student in this work consisted of the optical characterization of the PDI in solutions (absorption, PL and Time Resolved PL), fabrication and optical characterization of the nanocomposites (absorption, PL and Time Resolved PL), and fabrication and characterization of the waveguide structure (light amplification, waveguided PL, Time Resolved PL and ASE stability).

In parallel, the student developed the appropriate technology process to incorporate MNPs in optical waveguides, in order to exploit their optical properties (high scattering cross sections, plasmonic resonances) for photonics. For this purpose, he initially studied an in-situ growth of Au MNPs in the commercial photoresist Novolak. Here, the control of the size and concentration of MNPs inside the matrix resulted in a way to tune the optical properties of the

plasmonic nanocomposite. Then, the refractive index of the Novolak-MNPs nanocomposite was carefully analyzed, both experimentally and numerically, in order to find the appropriate fabrication conditions (filling factor and growth time) to optimize the scattering cross section at a desired wavelength. Finally, the nanocomposite was patterned inside a PMMA waveguide to exploit its scattering properties to couple and guide a normal incident laser light beam along the polymer. In this way, light coupling was experimentally demonstrated in a broad wavelength range (404-780 *nm*). These results are summarized in section 3.2 of this Ph.D. Thesis and have been published in an article entitled "**Polymer waveguide couplers based on metal nanoparticle-polymer nanocomposites**" published in *Nanotechnology* (impact factor 3.821 in 2014 ranked 24/145 in Applied Physics). The paper is attached in the annex of the present Thesis and it is cited as reference [77]. The participation of the student in this publication consisted of the fabrication of the different nanocomposites and waveguiding structures, optical and microscopic characterization (transmission/reflectivity, SEM images, coupling efficiency, etc.), and calculation of the effective refractive index in the structure.

In the next step, the PDI-PMMA nanocomposite was integrated together with Ag nanoparticles 100 *nm* in diameter in order to study the interaction between both materials. For this purpose, a drop casting technology to deposit homogeneous layers of MNPs was properly optimized. The interaction between plasmonic nanoparticles and PDI molecules was studied in order to find the optimum conditions to enhance the PL under a weak exciton-plasmon coupling. Moreover, the MNPs-PDI system was integrated in a multilayered waveguide structure in order to improve this interaction under relatively high light confinement

conditions. In this way, a Purcell factor greater than 10 has been successfully demonstrated when measured at the output edge of the waveguide. These results have been summarized in section 3.3.1 of this Thesis and form part of the paper entitled "**Purcell-enhancement of the radiative PL decay in perylenediimides by coupling with silver nanoparticles into waveguide modes**". The paper has been recently published in *Applied Physics Letters* (impact factor 3.411 in 2016 ranked 28/147 in Applied Physics), which is also attached in the Annex of the present Thesis and it is cited as reference [78]. The participation of the student in this work consisted in the fabrication of the devices, optical characterization and analysis of PL and Time Resolved PL data, and calculation of the PL enhancement as a function of the separation between the PDI molecule and the MNPs.

Finally, Ag MNPs and PDI were properly integrated in order to demonstrate lasing operation under random distributed feedback conditions. These results are summarized in section 3.3.2 of this Thesis and are expected to be submitted for publication in brief. The participation of the student in this work consisted in the realization of the devices, the optical characterization measurements (PL spectra) and modelling the laser curve.

2 Experimental techniques

This chapter summarizes the experimental techniques used in this Thesis. The first section contains the different fabrication procedures used to deposit layers of polymers and nanoparticles (spin coating, drop casting), or to create patterns (UV lithography). The second section is focussed in the morphological (SEM, profilometer) and optical (reflectivity, absorption, PL, Time Resolved PL, light coupling) characterization of the nanoparticles, layers and waveguides.

2.1 Fabrication techniques

2.1.1 Spin coating

Spin coating (Figure 6) is a common technique used to deposit thin films on flat substrates of a material dispersed or diluted in solution. It consists of dropping an amount of this solution at the centre of the substrate (Figure 6(a)) that is previously fixed on a sample holder (usually by vacuum). Then, the holder chuck is rotated (Figure 6(b)) at sufficiently high velocity (1000-3000 *rpm*, typically) to produce a solution layer on its entire surface by centrifugal force. The thickness of the final film after solvent evaporation and material curing/baking can be modified by the spin velocity and the material viscosity, which can be controlled with the concentration of the material in the solvent.

At the end of the process the spin-coated films are usually baked at a specific temperature (Figure 6(c)) to evaporate the solvent and to promote the formation of the layers. For example, for polymers or resists, a second bake is

made at temperatures higher than the vitreous transition to polymerize the material.
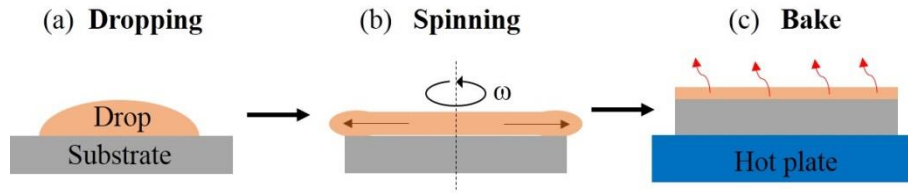

Figure 6. Steps of the spin coating technique: (a) dropping, (b) spinning and (c) solvent evaporation.

The film thickness can be measured by different methods. For example, in this work this parameter was controlled by the reflectivity characterized with a reflectometer, or by measuring the profile with a mechanical profilometer after scratching some regions of the sample.

2.1.2 UV-lithography

UV lithography or photolithography, is a process used in Microtechnology to define patterns down to 1 μm^2 on a resist previously deposited on a flat substrate. For this purpose, a photoresist is firstly deposited on the top of the sample, as it is illustrated in Figure 7(a). Then, the sample is aligned in contact with a quartz mask (Figure 7(b)) containing Cr_2O_3 patterns with the design to be transferred on the resist. In this way, the regions of the resist protected by the Cr_2O_3 patterns are not activated with the posterior illumination with a UV lamp (Figure 7(c)). Finally, sample is immersed in a solution (developer) able to remove the zones of the resist which were exposed (for positive resist) or unexposed (for negative resist) in the previous step (Figure 7(d)). Consequently, a negative resist will reproduce the mirror image of the Cr_2O_3 patterns, while a positive resist will form the same pattern structures.

Here the commercially available positive resist Novolak (product ma-P 1275 from micro resist technology GmbH, with a resolution of 1 μm) was chosen.

The UV lithography was performed with a commercial setup (model MJB4 from SUSS MicroTec) by using the following procedure:

(a) Novolak (Nv) resist was deposited on SiO_2/Si substrate with spin coating technique (3000 *rpm*, for 30 *seconds*), and then post bake at 65 °C for 2 *minutes*.

(b) a mask was put in contact with the sample (substrate + resist film),

(c) the sample was illuminated with a UV (Hg) lamp for four *seconds*,

(d) the UV-sensitized film was developed by dipping the sample in a solution of Tetramethylammonium hydroxide (product ma-D 525S from micro resist technology) diluted in water, in a ratio 1 to 1, for 20 *seconds*.
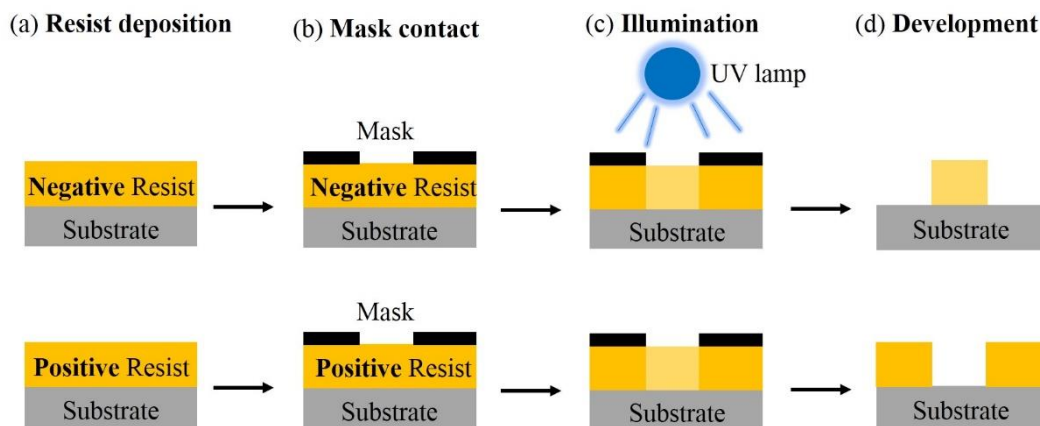
Figure 7. UV-lithography process for negative and positive type resists: (a) the deposition of the photoresist on the substrate, (b) the contact of the optical mask with the resist, (c) the illumination and (d) the development.

2.1.3 Drop casting

Drop casting consists of the formation of a film from a liquid directly dropped on the desired substrate (see Figure 8(a)). Once the solvent is evaporated (Figure 8(b)) the film, whose thickness mainly depends on the concentration of the material dispersed/diluted in the solution, is formed on the sample.

This is an easy, cheap and fast technique to form layers, but it usually lacks from homogeneity and reproducibility manly due to the different evaporation rate of the solvent on the surface of the sample and the inhomogeneous distribution of the material in the drop.
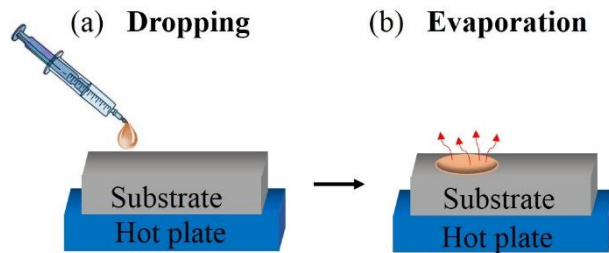
Figure 8. Illustration of the two steps of the drop casting technique: (a) dropping and (b) solvent evaporation.

In this work this method was used to deposit metal (Ag) or dielectric (TiO_2) nanoparticles. For this purpose, these problems were solved by following this procedure:

(i) the solution was immersed in an ultrasonic bath for 2 *minutes* before dropping on the substrate,

(ii) we kept the substrates at a fixed temperature (50 $°C$), during all the procedure,

(iii) this process is repeated twice consecutively.

2.1.4 Waveguide

The waveguides studied in this Ph.D. Thesis were fabricated by depositing/patterning polymer or nanocomposites on commercial SiO_2/Si substrates supplied by Cemat Silicon (Poland) (see Figure 9). The higher refractive index of the polymer ($n_c \approx 1.5$ at 600 *nm*) with respect to that of SiO_2 ($n_s = 1.458$ at 600 *nm*), results in a high enough refractive index contrast ($100(n_s -$

$n_c)/n_s \approx 2.8 \%$) to produce an optical waveguide. In particular we propose the use of 0.5-2 μm thick Poly(methyl methacrylate) (PMMA) film (or a PMMA nanocomposite) as the core of the waveguide. The thickness of the SiO_2 layer, thermally grown on the top of the Si substrate, was chosen to be around 2 μm in order to isolate the polymer waveguide from the silicon substrate (whose refractive index is 3.95 at 600 nm) in the visible-near infrared range.
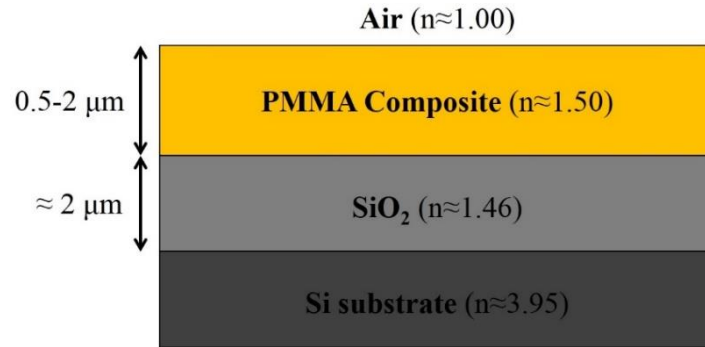
Figure 9. Scheme of the optical waveguide structures adopted in the present work.

2.2 Characterization

2.2.1 Structural characterization

Scanning Electron Microscopy (SEM)

Resolution of images obtained with standard light microscopy techniques is limited by the fundamental laws of diffraction to $\lambda/2n$, and hence it is restricted to hundreds of nm for visible light. In a Scanning Electron Microscopy (SEM), however, images are scanned by the interaction of a focussed beam of electrons with the sample, and the posterior analysis with different detectors. Therefore, since the electron wavelength, given by the De Broglie equation ($\lambda = h/(m_e v_e)$), is in the order of few picometers, resolution is reduced to the nanometer scale [79], and it is mostly limited by external factors (detectors resolution, electron beam shot noise, electron diffusion effects, etc.) rather than the probe mechanism.

The microscope used in this work was the model S-4800 from HITACHI, and presents a field emission gun (FEG) with a 1.4 *nm* resolution at 1 *kV*. This equipment has a detector of backscattered electrons, Bruker RX detector, transmittance detector, The QUANTAX 400 program for microanalysis and five motorized axes. The characterization was performed under high vacuum conditions, with a working distance of 8 *cm* and a FEG of 1-10 *kV*.

This device was used to analyse the surface of the samples (usually covered by metal nanoparticles) or the cross sections in a multilayer structure. For this purpose, conductivity of the samples was usually enhanced by a very thin sputtering layer of gold (1-5 *nm*) and/or covered the borders with silver tint.

Profilometer

A profilometer is a measuring instrument used to analyse the surface's profile of the samples. The device used in this work is the contact profilometer Dektak 150 Surface Profiler from Veeco. It consists of a stylus, with a well-defined tip, which is moved vertically until it is in contact with the sample, and then shifted laterally across the sample for a specified distance and contact force. The vertical resolution is about 2 *nm* that is mainly limited by the dimensions of the tip.

This device was used to measure the roughness and the thickness of the layers. For this purpose, samples were previously scratched if UV lithography was not performed previously.

2.2.2 Optical characterization

Reflectivity/transmission

The reflectivity (R) and transmission (T) measurements were performed by using a commercial reflectometer (Nanocalc-2000 from Mikropak/Ocean), schematically illustrated in Figure 10(a). This setup consist of a UV-visible double source Deuterium + Halogen (λ_{IN}) coupled into an optical fiber that illuminates the sample surface under normal incidence and collects the transmitted (λ_T) or the reflected (λ_R) signals.

Absorbance

Light absorbance is the fraction of incident light taken by a sample, without reflection or scattering.
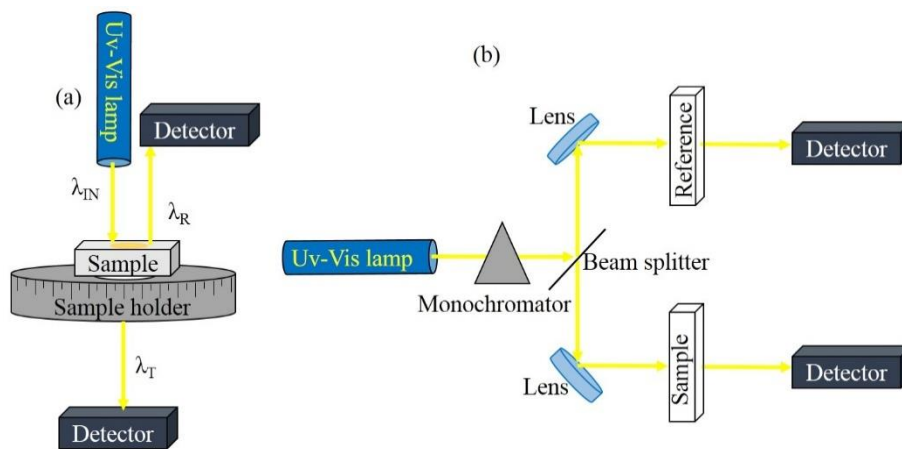
Figure 10. Scheme of the experimental setups used to measure (a) the transmittance, (a) the reflectivity and (b) the absorbance.

In this Ph.D. Thesis, absorbance spectra for samples in solution or in solid state (previously deposited on glass), were measured with a commercial Shimadzu UV-2501PC spectrophotometer (UV-visible range, schematically represented in Figure 10(b)). This device consists of a UV-Visible Xenon lamp coupled to a monochromator, with a resolution of 0.5 *nm* (300-900 *nm* range). Then the

monochromatic light beam is split in two branches containing a reference and the sample to be analyzed. Finally light transmitted by both the reference (T_{Ref}) and the sample (T_{Sample}) is collected by two photodetectors, and the absorption is calculated by the well-known formula:

$$Abs = -log_{10}\big(T_{Sample}/T_{Ref}\big)$$

(2.1)

Reference samples were the solvents or a glass substrate for solution and solid state measurements, respectively.

Back and forward scattering Photoluminescence (PL)

Photoluminescence (PL) is an optical process from which a material spontaneously emits photons after the absorption of light at a shorter wavelength.

Figure 11. Scheme of the setup used to measure the PL of the samples in the back or forward scattering configuration.

In this Thesis PL signal, generated from dye molecules, was analysed by using the experimental setup illustrated in Figure 11. Samples were placed on a XYZ positioner and illuminated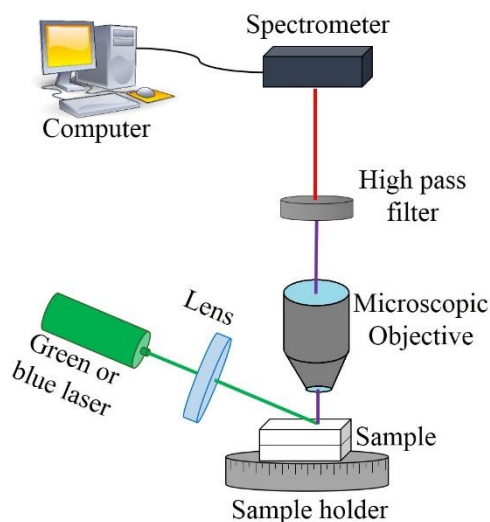 with Continuous Wave (CW) lasers at 532 *nm* (Nd:Yag doubled) or 404 *nm* (GaN) with an incident angle of around 45 *degrees*.

40

Excitation fluency was set to be around around 20 mW/cm^2 by focusing the beam on a spot of ≈ 1 mm^2 at the surface of the sample. Then the PL signal was collected along the normal direction to the sample surface with the aid of a 10x microscope objective (numerical aperture 0.22), from which collected light is coupled into an HR4000 Ocean Optics spectrograph (resolution ≈ 0.7 nm) through a multimode optical fibre. High pass filters with $\lambda_{cut-off} = 550$ nm or 450 nm were included in the PL signal collection arm to eliminate light scattering from the sample at the excitation green and blue laser wavelengths, respectively.

Time Resolved Photoluminescence (TRPL)

Time Resolved PL (TRPL) experiments consist of the characterization of the PL transients produced in a material after pulsed laser excitation. This spectroscopy is used in the present work to find the effective recombination time of the electron-hole pairs in the material giving rise to the emission of a photon (radiative path), but also to the emission of phonons (non-radiative paths).

These measurements require the simultaneous acquisition of the laser pulse and the emitted signal, in order to synchronize the pulsed laser with the emission of PL. For this purpose, the laser beam was split in two branches (see Figure 12): the reference, which gives the "start" signal, and the excitation, which produces the PL signal from the samples. The excitation path contained neutral density filters to control the excitation power. Then the PL signal was collected with a 10x microscope objective (numerical aperture 0.22), which focused the light into a Hamamatsu C5658−3769 avalanche photodetector connected to a BOXCARDPCS-150 electronics from Becker and Hickl GmbH. Before the photodetector, a high pass filter with $\lambda_{cut-off} = 550$ nm, is incorporated in order to eliminate light scattering from the sample at the green laser wavelength. It is worth mentioning that this kind of measurement needs a certain level of data

accumulation in order to increase the signal to noise ratio. In addition, the excitation source should be carefully chosen in order to provide short enough pulses with a repetition rate longer than the PL lifetime. For this purposed two different kinds of Nd:Yag lasers doubled to 532 *nm* were used.

(a) Nd:YAG laser doubled to 532 *nm* with a repetition rate of 10, 100 or 1000 *Hz*, a pulse width of 1 *ns* and average power of 30 *mW* (at 1 *kHz*).

(b) Nd:YAG laser doubled to 532 *nm* with a repetition rate of 20 *kHz*, a pulse width of 1.2 *ns* and an average power of 3 *mW*.
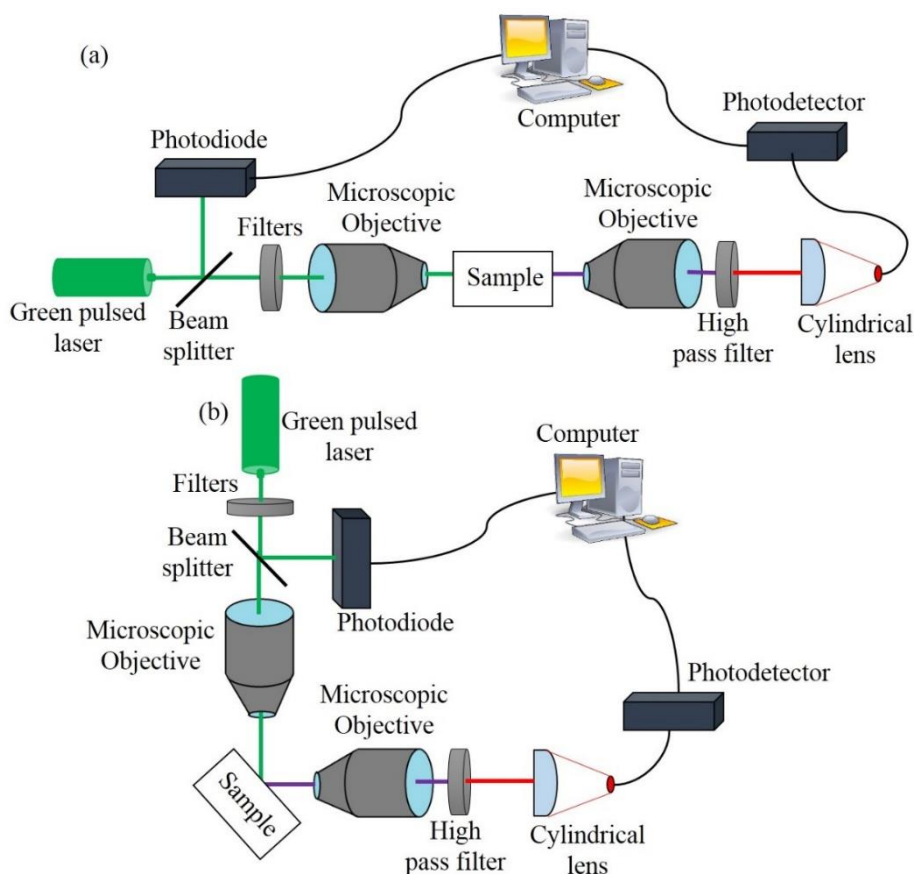
Figure 12. Scheme of the different configuration used for the TRPL measurements: (a) waveguide and transmission and (b) scattering, with a 45 *degrees* angle between excitation/collection and the samples surface.

The decay time of the excited state of a molecule to the ground state can be expressed by a typical rate equation:

$$\frac{dI(t)}{dt} = -kI(t) + f(t)$$

(2.2)

Where I is the number of excited elements at time t, k is the rate constant of all de-excitation processes and $f(t)$ is an arbitrary function of the time, describing the photo-generation. If excitation is switched off at $t = 0$, equation 2.2 takes the form:

$$\frac{dI(t)}{dt} = -kI_0$$

(2.3)

Integrating 2.3 give

$$I(t) = I_0 e^{-t/\tau}$$

(2.4)

where, I_0 is the intensity at time zero (upon excitation) and τ is the lifetime ($\tau = 1/k$), which is defined as the time for the intensity to drop by $1/e$. In general, more than one decay time can be observed depending on the environment conditions. So equation 2.4 becomes

$$I(t) = I_0 \sum_{i=1}^{n} A_i\, e^{-t/\tau_i}$$

(2.5)

In our case up to two decay times ($n = 2$) were, usually, needed to fit our experimental data (which an example is given in Figure 13).

The data from TRPL spectra (h) are the convolution ($*$) between the function (f) that represents the temporal decay of the PL and the system response function (g), which is plotted in the grey area in Figure 13:

$$h = f * g$$

<div align="right">(2.6)</div>

By taking in account Equation 2.5 f is defined as:

$$f = A\left(e^{-t/\tau_1} - e^{-t/\tau_{rise}}\right) + Be^{-t/\tau_2}$$

<div align="right">(2.7)</div>

where A and B are amplitude constants, τ_{rise} is the rising time (fixed equal to 0.1 ns, i.e., negligible as compared to the laser pulse width) and τ_1 and τ_2 are different decay mechanisms (usually just the first one becomes necessary). In Figure 13 a table is inserted with the values used in the fitting of a TRPL spectrum recorded in one of our samples.

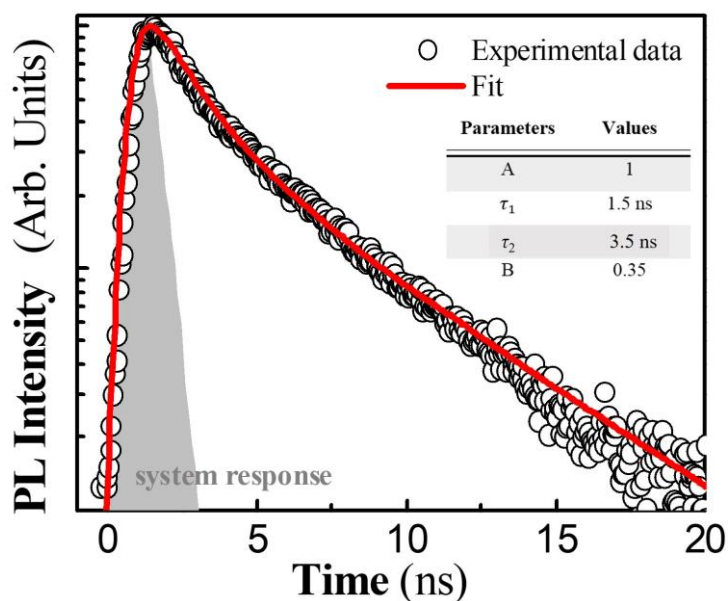| Parameters	Values
A	1
τ_1	1.5 ns
τ_2	3.5 ns
B	0.35

Figure 13. Example of a typical TRPL spectra (black open symbols) obtained and its exponential fitting curves (red line); grey shaded area corresponds to the temporal system response. The inset present a table with the parameter used in the fitting.

2.2.3 Waveguide characterization

End-fire coupling

End-fire coupling experiments consist of coupling a laser light beam into the input edge of waveguides with the aid of a microscope objective (40x infinite corrected, numerical aperture 0.66), and collecting the waveguided light from the output edge of the structure (see Figure 14(a)) with another microscopic objective (20x, numerical aperture 0.35).

This system firstly allows the characterization of the near field distribution of the modes at the output edge of the sample. For this purpose, light collected by the second objective was focused into a CCD camera (model DCU224C from Thorlabs, see Figure 14(b) and (c)). Neutral density or linear polarizer filters could be inserted in excitation/collection paths in order to set the light intensity or to choose the polarization.
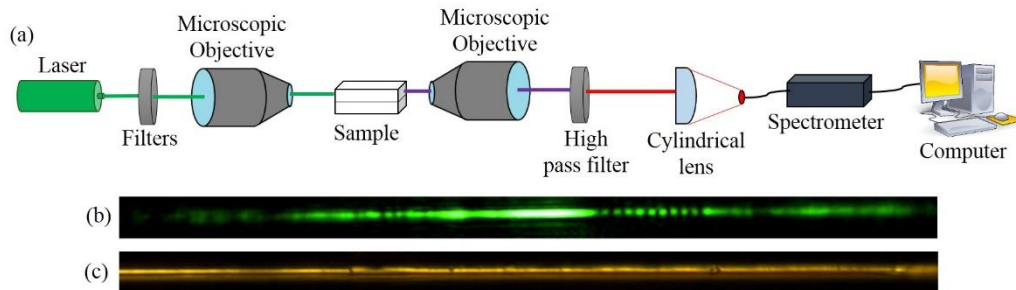
Figure 14. (a) Scheme of the experimental setups used for the waveguides characterization with end-fire coupling. Photographs of light at the output edge of the waveguide for (b) the green pump laser and (c) the PL signals.

In addition, this experimental set-up allows the characterization of the emission of light in active waveguides. For this purpose a laser pump beam (usually a Nd:Yag doubled to 532 *nm* described in the last section) was coupled inside the structure, and light collected by the output objective was focused into a HR4000 Ocean Optics spectrograph. A high pass filter, (normally a $\lambda_{\text{cut-off}} = 550$ *nm*) and a cylindrical lens was included to cut the laser line and focalize the line

modal distribution of the planar waveguide into a point (and hence to enhance the signal to noise ratio). Finally, this geometry can also be exploited to analyze the recombination time inside the waveguide by combining it with the setup shown in Figure 12(a). For this purpose, the laser light beam was split into two branches before the input microscope objective, and light collected by the second microscope objective was focused into the Hamamatsu C5658−3769 avalanche photodetector connected to a BOXCARDPCS-150 (see Figure 12(a))

Surface Illumination

The surface of the waveguide was illuminated under normal incidence to analyze the coupling efficiency of gold metal nanoparticles (MNPs) integrated in the structure (see section 3.2.4). For this purpose, the incident light was carefully positioned in the region with Au MNPs in order to maximize the scattering of light with the aid of an aspherical lens (focal length 11 *mm*, numerical aperture 0.25), as it is illustrated in Figure 15(a). Then the guided light traveling along the waveguide was collected at the output edge of the sample by using a 20x microscope objective (numerical aperture 0.35), which focused the guided light into an HR4000 Ocean Optics spectrograph, or the CCD camera (the same as in Figure 14). A cylindrical lens could be included before the spectrograph to focalize the line distribution of the waveguide into a point. Different CW lasers were used to test the light coupling by the Au MNPs into the PMMA waveguides at different wavelengths: 404 *nm* and 450 *nm* (semiconductor lasers), 532 *nm* (Second harmonic of a Nd:Yag laser), 590 *nm* and 633 *nm* (HeNe lasers), and 780 *nm* (semiconductor laser).

Variable stripe length method

The Variable Stripe Length (VSL) method is a common technique to characterize the optical gain and/or losses in a planar waveguide [80-83]. It consists of focusing the excitation beam on a straight line on the surface of the waveguide, usually with the aid of a cylindrical lens. Before the lens, a slit is typically installed to select the central part of the Gaussian laser beam, and hence to provide a uniform illumination. In this way, the length d of this line can be varied to obtain information on the gain in the waveguide, or, the excitation line can be moved inside the waveguide to estimate the waveguide losses [80-83].
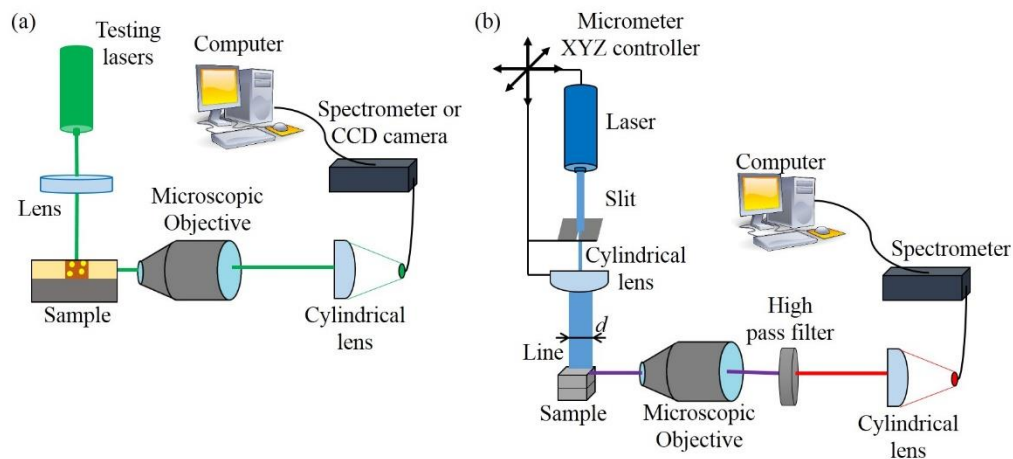
Figure 15. Scheme of the experimental setup used (a) for analyzing the coupling efficiency due to the scattering of the gold MNPs and (b) for illuminating the waveguide with a uniform straight line beam.

In our setup the light, from a CW Nd laser ($\lambda = 532$ *nm*) with a power ≈ 20 *mW/cm^2*, or the pulsed Nd:Yag laser doubled to 532 *nm*, described before, were focused into a stripe 1 *mm* long and 0.2 *mm* wide (Figure 15(b)). The light at the output edge of the waveguide was collected with a 20x microscope objective (numerical aperture 0.35), which coupled waveguided light into an HR4000 Ocean Optics spectrograph through a multimode optical fiber. A long pass filter

and a second cylindrical lens was also included to eliminate laser scattered light before the detector and to increase the signal to noise ratio, respectively.

3   Summary of Results

This chapter summarizes the most important results obtained during this Ph.D. Thesis work.

Section 3.1 is devoted to the optical characterization of the active elements proposed in this work (Perylenediimides derivatives). Here are also establishes the conditions to generate optical gain in waveguides using this organic compound as their active medium. The optical properties of the MNPs used in this Ph.D. Thesis work are summarized in section 3.2 together with the fabrication procedures to integrate them in photonic structures, namely optical waveguides. The particular optical properties of MNPs are exploited for different functionalities. Particularly, MNPs with high scattering cross section are proposed to be integrated in polymer waveguides to develop optical couplers for normal incident light. Finally, MNPs can be also integrated together with optical waveguides containing organic compounds, the PDI, in order to study the interaction between both materials. In particular, MNPs are demonstrated to enhance the photoluminescence by the reduction in the emitter radiative lifetime or Purcell effect by exciton-photon coupling (section 3.3.1), or to provide the necessary light scattering to define a random distributed feedback laser (section 3.3.2).

3.1   Amplification of Spontaneous Emission in Perylenediimides based waveguides

Optical gain (or stimulated emission) is a light emission process where an incident photon promotes the generation of a second photon with the same frequency, phase and direction. For this purpose, the generation of light in the

49

medium needs to overcome the absorption, or in other words, the population of electrons in the upper level needs to be greater than that in the ground level (inverted population). In these conditions, optical net gain (G) is usually modelled as the difference of electrons in the excited state (N_1) minus the electrons in the ground state (N_0) multiplied by a gain cross section (σ):

$$G = \sigma \cdot (N_1 - N_0)$$

(3.1)

where the first term is related with the gain of the material, and the second with the absorption losses.

3.1.1 Optical properties of the PDI compounds in solution

The Perylenediimides (PDI) used in this Thesis were synthesized in the group DYSMOL (Profs. Àngela Sastre-Santos and Fernando Fernández-Lázaro, Miguel Hernández University, Elche, Spain) following the methods explained elsewhere [50, 84]. Four different compounds (named PDI-1, PDI-2, PDI-3 and PDI-4) were prepared with the molecular structure shown in the insets of Figure 16, and then diluted in toluene at 10^{-5} M. Absorption and PL spectra of these solutions present the typical vibronic structure of PDIs materials [50, 85, 86]. For example, the absorption spectrum of PDI-1 (red curve in Figure 16(a)) exhibits four peaks at 424, 464, 498 and 535 nm, corresponding to the 0-3, 0-2, 0-1 and 0-0 vibronic transitions; while its PL (black curve in Figure 16(a)) show a mirror-like reflection spectrum with peaks at 545, 590 and 641 nm. Similar behaviors were observed for the other PDI-derivatives.

In addition, the four PDI solutions exhibit similar recombination time, τ, (5.9-6.2 ns, yellow data and exponential decay fit in Figure 17) with no influence

on the excitation fluency (0.3-30 μJ) and similar quantum yield, *QY*, (90-95 %) measured with a commercial apparatus (Hamamatsu C9920-02). Table I summarizes all photophysical properties measured in the studied PDI-derivatives in solution.

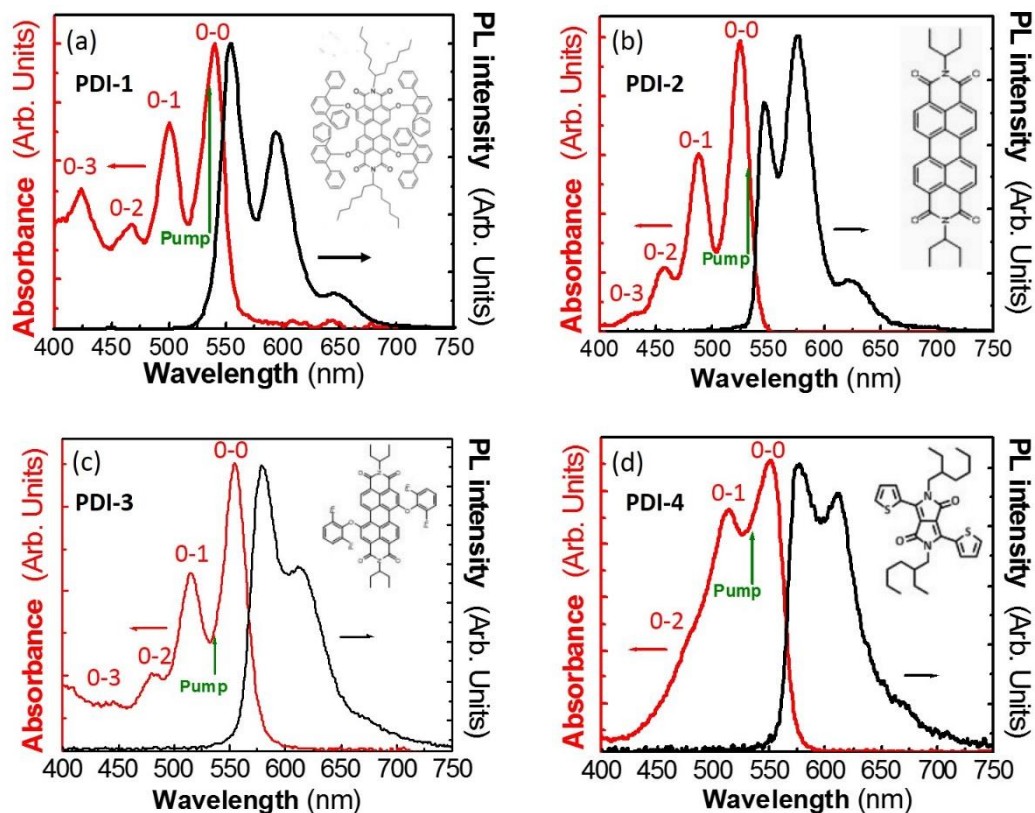**Figure 16.** Absorption (red line and left axis) at 10^{-5} *M* and photoluminescence (black line and right axis) spectra of the PDI in toluene solutions: (a) PDI-1, (b) PDI-2, (c) PDI-3, (d) PDI-4. With insight their relative molecular structure.
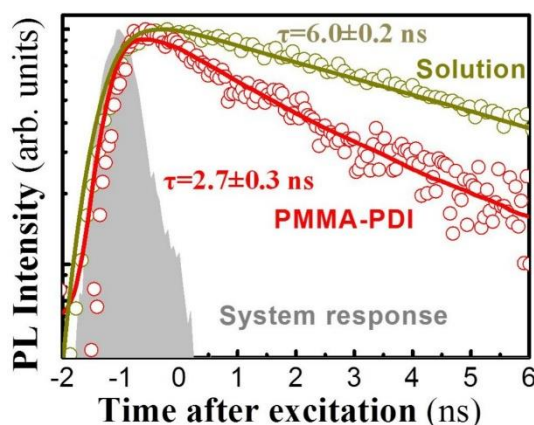

Figure 17. Recombination time of PDI-1 in toluene solution (yellow) and in the PMMA film (red) data (hallow circlet) and fit (continues line). Other PDI show similar behaviours.

Table I. Photophysical properties of the PDI compounds in toluene solution used in this Thesis.

PDI	λ_{Abs} (*nm*)	λ_{PL} (*nm*)	τ (*ns*)	QY (*%*)
PDI-1	464	546	5.9	95
	498	590		
	535	642		
PDI-2	457	542	6.2	92
	488	578		
	525	622		
PDI-3	482	579	5.9	90
	513	612		
	554	670		
PDI-4	514	576	6.1	90
	551	611		

3.1.2 PDI-PMMA composite characterization

The PDI organic compounds were integrated in the waveguide structure by dispersing the PDI in a PMMA matrix. For this purpose, solutions of PDI and PMMA, both diluted in toluene, were mixed in the appropriate proportion (5 *% w.t.*) and then spin coated on the substrate by following the procedure explained in the experimental section [76] that assures the formation of solid state PMMA-PDI nanocomposite films.

PDI-PMMA films were firstly characterized by depositing a ≈ 600 *nm* thick nanocomposite film on glass and silicon substrates (as show in Figure 18) in order to analyze absorbance and reflectivity (section 2.2.2), respectively. Figure 19 presents the absorption (black line and left axis) and photoluminescence (red line and right axis) spectra of the different PDI-PMMA films deposited on a glass

substrate. Here, the structure of the PDI molecule plays an important role in the optical properties of the nanocomposites. For example, despite that absorption spectra of the PMMA-PDI-1 nanocomposite is blue-shifted by 10 *nm*, its shape is similar to that measured in solution that indicates the absence of aggregation in the spin-coated film (Figure 19(a)). In addition, its broader PL spectrum shows the activation of other vibrational transitions. Similar conclusion is obtained for PDI-3 (Figure 19(c)) and PDI-4 (Figure 19(d)) nanocomposites. However, both absorption and PL of PMMA-PDI-2 nanocomposites exhibit a different behaviour (Figure 19(b)). Although spectra are not shifted as compared to the solution, we observe a broader shape that could indicate the formation of H-aggregates in the films [35, 87]. Table II summarizes all photophysical properties of the solid-state PMMA-PDI nanocomposites.
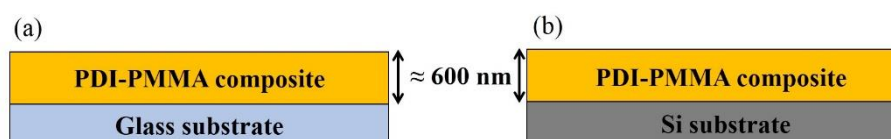
Figure 18. PDI-PMMA nanocomposite deposited on (a) glass and (b) silicon substrate for the characterization of its optical properties.

The complex refractive index of the PMMA-PDI nanocomposites has been estimated from the reflectivity spectra of a 600 *nm* thick film deposited on a silicon substrate (Figure 20(a)). The imaginary part is calculated from the absorption curve, whereas the real part (blue line in Figure 20(b)) is obtained from the interference intensity modulation in the reflectivity spectra. Theoretical reflectivity calculated by this approximation (red line in Figure 20(a)) clearly agrees with the experimental measured curve (hollow circles in Figure 20(a)) for the PMMA-PDI-1 compound. The other nanocomposites (PMMA-PDI-2 to -4) exhibited similar behaviours.

Table II. Photophysical properties of the PDI-PMMA composite used in this Thesis.

PDI	λ_{Abs} *(nm)*	λ_{PL} *(nm)*	τ_d *(ns)*	**QY** *(%)*
PDI-1	458	537	3.0	30.6
	491	580		
	530	360		
PDI-2	461	555	3.3	-
	487	583		
	522	615		
PDI-3	481	580	3.1	-
	515	613		
	555	668		
PDI-4	512	568	3.5	-
	547	610		

Finally, it is worth mentioning that the quantum yield in the PMMA-PDI-1 film was 30.6 %, as measured with the commercial system and the decay time (τ_{eff}) was measured around 3 *ns* (see red curve in Figure 17), which is half the value of the decay time measured in solution (6 *ns*). This is due to the contribution of non-radiative path in the exciton recombination, given that 6 *ns* should be considered as the exciton radiative lifetime of the PDI compound. We will come into this discussion in section 3.3.1.
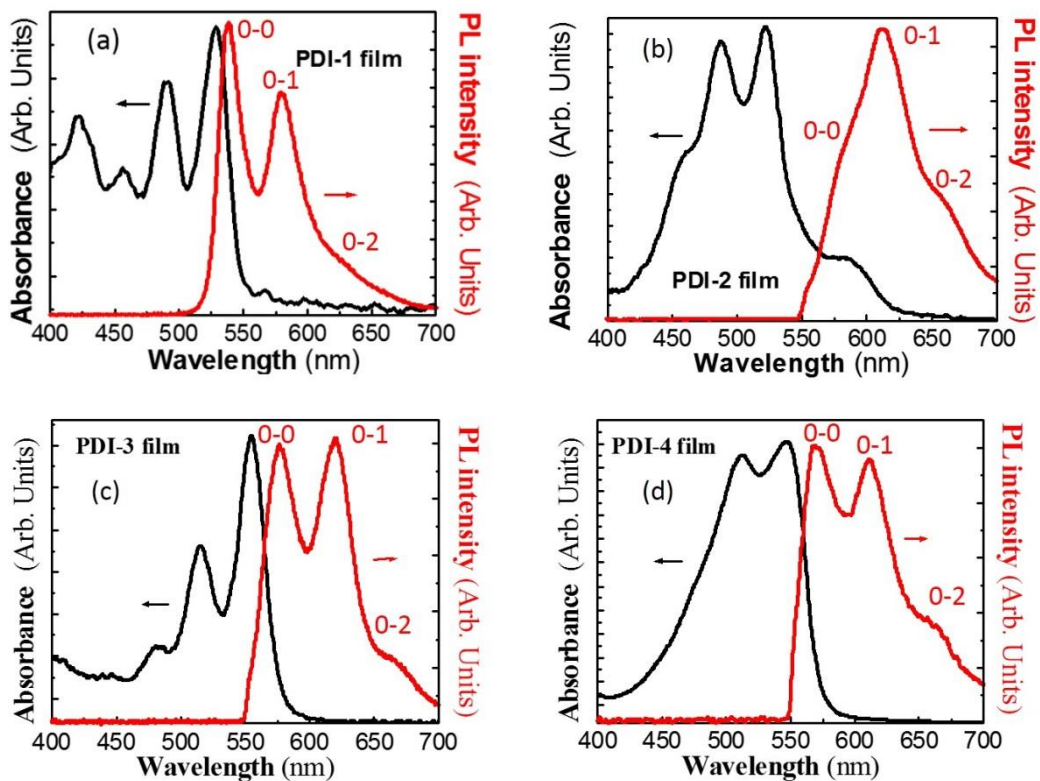
Figure 19. Absorption (black line and left axis) and photoluminescence (red line and right axis) spectra of (a) PDI-1, (b) PDI-2, (c) PDI-3 and (d) PDI-4 in PMMA film at 5 *% wt*.
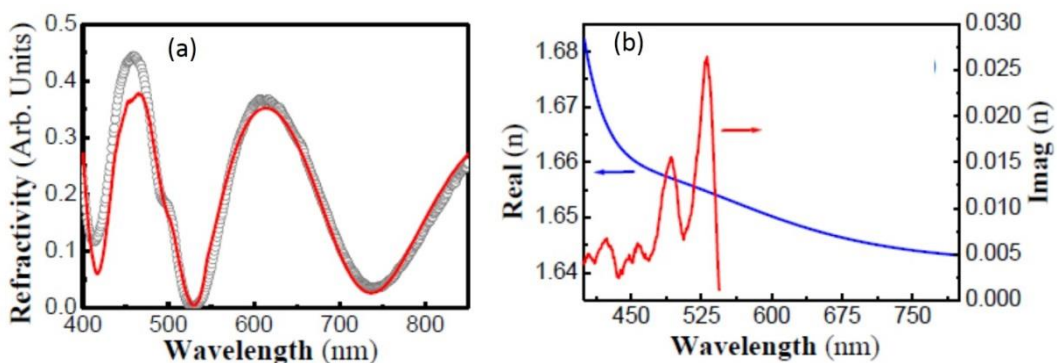
Figure 20. (a) Experimental (black points) and theoretical (red line) reflectivity of a PMMA-PDI-1 film deposited on silicon. (b) Real part (blue line and left axis) and imaginary part (red line and right axis) of the extracted refractive index for the PMMA-PDI-1 composite.

In addition, since the 0-0 transition of PDI derivatives is limited by self-absorption losses (see overlap of PL and absorption spectra in Figure 16 and Figure 19) optical gain in PDI-derivatives is usually obtained for the 0-1 vibronic state. In this way, this transition corresponds to the first excited state of the four-level scheme of the PDI compounds. For this purpose, a high enough concentration of the organic compound in the polymer (0.2-5 *% w.t.*) is usually

needed in order to promote the required electron density in the upper state for achieving stimulated emission.

3.2.2. Geometrical optimization to demonstrate ASE

Once the properties of the PMMA-PDI nanocomposites were characterized, films were deposited on a SiO$_2$/Si substrate in order to check the optical properties in a waveguide configuration (Figure 21(a)). For this purpose, the thickness of the layers was fixed to about 1200 *nm* in order to assure single mode propagation at the emission wavelength ($\approx$ 600 *nm*). Then PL of the film was excited by end fire coupling a Nd:YAG laser doubled to 532 *nm* (1 *ns*, 100 *Hz*) at the input edge of the waveguide and collecting the waveguided PL from its output edge (see Figure 14(c)). However, the high concentrations needed for optical amplification (5 *% w.t.*) restricts the propagation of the laser excitation beam at 532 *nm* down to a few microns due to the strong absorption of the PDI compound (around 2000 *cm^{-1}* for PDI-1 embedded in PMMA at 5 *% wt.*). Consequently, this structure did not show ASE for the range of laser fluencies studied here (green symbols in Figure 22(a)). Indeed, to the best of our knowledge, a surface excitation has always been needed to demonstrate ASE with similar configurations [50, 85, 86, 88, 89].

For this reason, a modified multilayer architecture was proposed (the one depicted in Figure 21(b)) in order to allow the co-propagation of the excitation laser beam and the PL signal generated inside the waveguide. It consisted of a thin (25-200 *nm*) layer of PDI-PMMA composite (with a concentration 5 *% wt.* of PDI) sandwiched between two thicker passive layers of PMMA, both with a thickness around 650 *nm* (Figure 21(b)). In this way, the absence of losses in the claddings alleviates the attenuation of the laser excitation beam, while the PL is highly confined at the centre of the structure forming the waveguide core. Indeed,

this configuration previously demonstrated an optimum of PL signal generation at the exit face of the waveguide by using colloidal QDs as active medium [90].
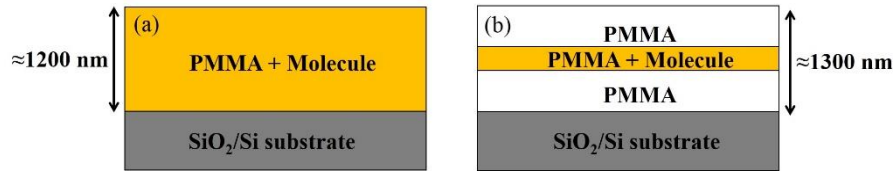

Figure 21. Structure of the samples studied: (a) monolayer waveguide, (b) sandwich type waveguide.
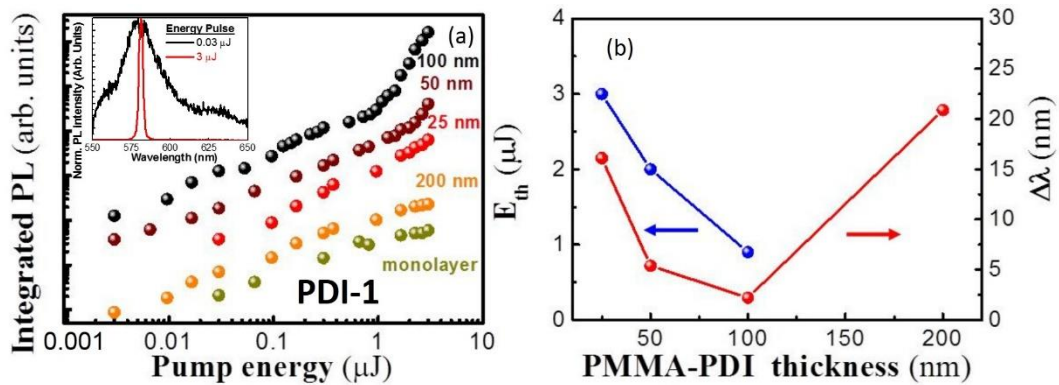
Figure 22. (a) Integrated PL as a function of the laser pump fluency for different thicknesses of the PMMA-PDI-1 active layer. Black, brown, red and orange colours refer to 100, 50, 25 and 200 *nm* thickness. Dark yellow show the results obtained with a PMMA-PDI monolayer waveguide, where no amplification was observed. In inset, are shown the normalized PL spectra at pump fluency of 0.03 *μJ* (black curve) and 3 *μJ* (red curve), for the 100 *nm* active layer. (b) Energy threshold (blue and left axis) and linewidth (red and right axis) as a function of the thickness of the PMMA-PDI-1 intermediate layer.

Therefore, the proposed multilayer structure not only allowed the propagation of the laser excitation beam along the waveguide, but also the generation of stimulated emission for optimum geometrical parameters was demonstrated. Figure 22(a) presents in a log-log plot the integrated PL as a function of the laser excitation fluency for thicknesses of the nanocomposite ranging between 25 and 200 *nm* (being fixed the thickness of the PMMA claddings to 650 *nm*) for the PMMA-PDI-1 nanocomposite. Clearly, only thicknesses between 50 and 100 *nm* (wine and black symbols in Figure 22(a), respectively) exhibit a superlinear growth above a certain laser excitation threshold, which is the signature of stimulated emission. Simultaneously, the spectrum of the waveguided PL changes from a broad band below this threshold

(black line in the inset of Figure 22(a)) that collapses into a narrow line above the threshold (red line in the inset of the figure). Thinner films did not presented ASE (see red symbols in Figure 22(a) for a 25 nm thick PMMA-PDI-1 nanocomposite) due to the fact that the total quantity (or the effective concentration in the whole multilayer structure) of molecules is not high enough. On the opposite, films as thick as 200 *nm* did not exhibit ASE, but this time due to the strong attenuation of the pump beam (orange symbols in Figure 22(a)), as occur in the homogeneous nanocomposite waveguide of Figure 21(a). In these conditions, a PMMA-PDI layer 100 *nm* thick demonstrate an optimum ASE generation with the lowest E_{th} (0.9 μJ) and the narrowest linewidth (2.3 *nm*) [76], as observed in Figure 22(b).

3.1.3 ASE characterization

PL linewidth and intensity

Figure 23 plots the PL spectra measured at the output edge of the waveguide for a 100 *nm* thick PMMA-PDI-1 (the other composites showed similar behaviour) layer sandwiched between two 650 *nm* thick PMMA cladding layers. Above a threshold $E_{th} = 0.9$ μJ, the 1-0 vibronic transition collapses into a narrow peak with a Full Width at Half Maximum (*FWHM)* of 2.3 *nm* under the highest laser excitation fluency. Figure 24 shows the log-log plot of the integrated PL intensity (black dots and left axis) and the PL *FWHM* (hollow circles and right axis) as a function of the laser excitation fluency for waveguides containing PDI-1 (Figure 24(a)), PDI-2 (Figure 24(b)), PDI-3 (Figure 24(c)) and PDI-4 (Figure 24(d)). The threshold between the spontaneous and stimulated emission is clearly observed from the different slope in the curves at 0.9, 1.2 and 2.2 μJ for PDI-1, PDI-2, and PDI-4 respectively. Only PDI-3 did not exhibited ASE due, principally, to the low absorption efficiency of this dye at the excitation

wavelength of 532 *nm* (see Figure 16(c), black line). The laser excitation fluencies (values included inside Figure 23) inside the waveguide were estimated by assuming a coupling efficiency of around 1 *%* of the laser pump beam at the input face of the structure [76].

The lowest ASE threshold found for the PDI-1 compound is attributed to the absence of aggregation effects, and hence exhibiting a better emission efficiency [35, 87]. Indeed, waveguides containing the PDI-1 compound presented the narrowest linewidth of around 8 *meV* (2.3 *nm*), while waveguides containing PDI-2 and PDI-4 exhibited a linewidth of around 11 *meV* (3.0 *nm*) and 12 *meV* (3.3 *nm*), respectively. Table III summarizes the ASE properties of these devices.
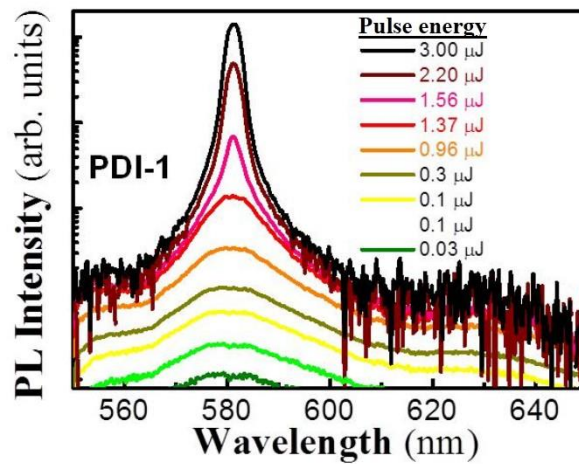
Figure 23. PL spectra for different laser pump fluencies at the output of a waveguide containing PMMA-PDI-1 composite 100 *nm* thick sandwiched between two 650 *nm* thick PMMA cladding layers.
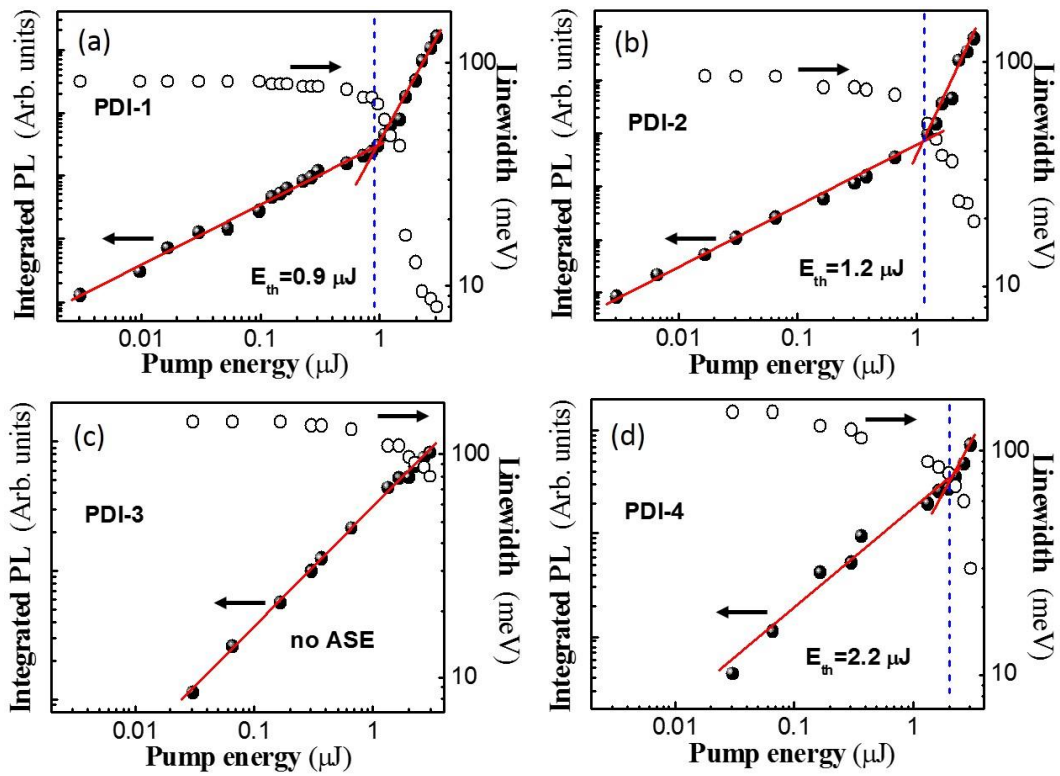
Figure 24. Integrated PL intensity (black dots and left axis) and the PL peak linewidth (hallow dots and right axis) as a function of the laser pump fluency, for waveguides containing (a) PDI-1, (b) PDI-2, (c) PDI-3 and (d) PDI-4.
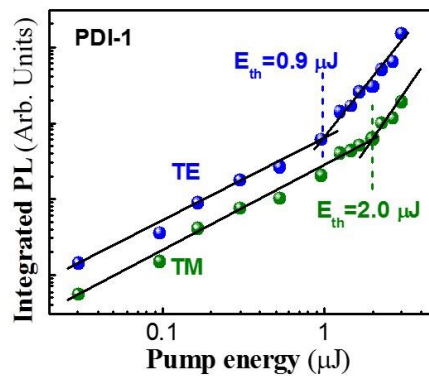
Figure 25. Integrated PL spectra for TE (blue dots) and TM (green dots) polarization for the sample containing PDI-1.

Figure 25 presents the integrated PL spectra for TE and TM polarization in a sample containing PDI-1 derivative (the other composites show similar behaviours). Light in TE polarization (blue symbols in Figure 25) exhibited lower threshold, $E_{th} \approx 0.9~\mu J$, than that in TM mode (green symbols in Figure 25), $E_{th} \approx 2~\mu J$, probably due to the fact that this particular geometry enhances the emission in the plane [76].

60

TRPL measurements

TRPL measurements are consistent with the generation of gain discussed above. When the structure was pumped well below the E_{th} value the TRPL spectrum exhibit an exponential decay (orange symbols and line in Figure 26(a)) with a decay time of around $\tau \approx 4.7$ *ns*, close to that measured for the organic compound in toluene solution (see Table I and yellow symbols and line in Figure 26(a)). Nevertheless, above a certain threshold the decay time decreases with the laser pump fluency down to the response of the system (grey area in Figure 26(a)).

Results plotted in Figure 26(a) correspond to the waveguide containing a 100 *nm* PMMA-PDI-1 nanocomposite (other waveguides showed similar curves). Symbols and solid lines refer to the experimental data and the fitting obtained with equation 2.6 (see section 2.2.2).
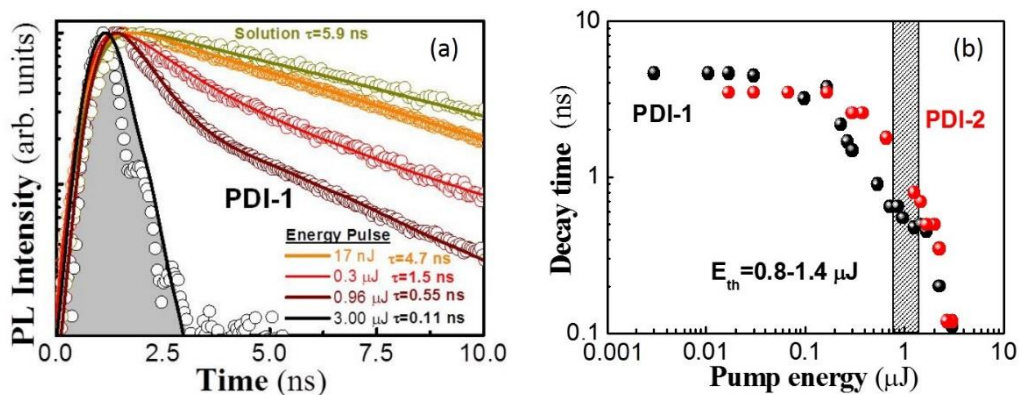
Figure 26. (a) TRPL spectra (open symbols) for PDI-1 under different laser pump fluencies and exponential fitting curves (continuous lines). Grey shaded area corresponds to the temporal system response. (b) Decay time as a function of the laser excitation fluency for PDI-1 (black symbols) and PDI-2 (red symbols) compounds.

Figure 26(b) plots the decay time as a function of the excitation fluency for waveguides containing PDI-1 (black symbols) and PDI-2 (red symbols) organic compounds. The reduction in the measured decay time of waveguided PL agrees in both structures with the threshold pulse energy of stimulated emission

deduced above from the growth of the integrated intensity of waveguided PL and its linewidth narrowing.

ASE stability

The stability of fabricated devices was characterized by acquiring ASE signal at the maximum pump fluency (3 *μJ*) every 60 *seconds* for 1 *hour*. Waveguides containing a PMMA-PDI-1 maintained half of the maximum signal over $15 \cdot 10^4$ and $6 \cdot 10^4$ laser shots for PMMA-PDI thicknesses of 50 and 100 *nm* respectively (see Figure 27(a)). In the same way stability of sample containing 100 *nm* of PMMA-PDI-2 nanocomposite demonstrated a similar behaviour: ASE is maintained up to $6 \cdot 10^4$ laser shots (see Figure 27(b)).
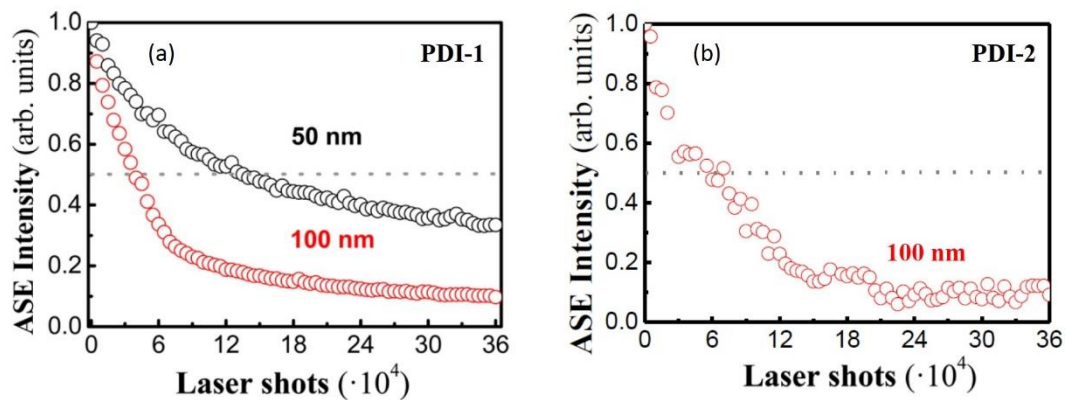
Figure 27. Integrated ASE intensity as a function of the laser shot for (a) PMMA-PDI-1 compound with thicknesses of 50 (black symbols) and 100 (red symbols) *nm* and for (b) PMMA-PDI-2 compound with thicknesses of 100 *nm* (red symbols).

Table III. ASE properties measured in the multilayer waveguides based on PDI compounds studied in this Thesis.

PDI	λ_{ASE} (*nm*)	E_{th} (μJ)	$\Delta\lambda$ (*nm*)	ASE stability (laser shot)
PDI-1	580	0.9	2.3	$6 \cdot 10^4$
PDI-2	576	1.2	3.0	$6 \cdot 10^4$
PDI-3	-	-	-	-
PDI-4	605	2.2	3.3	-

3.2 Optical couplers based on MNPs

Metal nanoparticles (MNPs) have been incorporated in polymer waveguides in order to exploit their particular optical properties for different applications (light redirection, PL enhancement, random distributed feedback for lasing). For this purpose, two kinds of MNPs were used: gold MNPs dispersed in a Novolak (Nv) matrix and commercial silver MNPs deposited by drop casting. The first nanostructures (gold MNPs) are grown in situ and presents a size controlled by the fabrication conditions. While the silver nanoparticles are supplied by NanoComposix and had a fixed diameter of 100 *nm*. The following sections detail the fabrication processes and optical properties obtained with these nanostructures.

3.2.1 Scattering and absorption cross sections of MNPs

As a preliminary step we calculate the extinction (σ_{ext}), scattering (σ_{sct}) and absorption (σ_{abs}) cross sections of the MNPs on the basis of the Mie theory [91]. In this way we could prove that the selected MNPs had their plasmonic resonance in the wavelength range we want to study.

$$\sigma_{ext} = \frac{\lambda^2}{2\pi n_m} \sum_{l=1}^{\infty} (2l + 1)[Im(t_l^E) + Im(t_l^M)]$$

(3.2)

$$\sigma_{sct} = \frac{\lambda^2}{2\pi n_m} \sum_{l=1}^{\infty} (2l + 1)[|t_l^E|^2 + |t_l^M|^2]$$

(3.3)

$$\sigma_{abs} = \sigma_{ext} - \sigma_{sct}$$

(3.4)

where n_m is the refractive index of the medium surrounding the MNPs, t_l^E and t_l^M the electric and magnetic scattering coefficient whose expression can be found in [91]. The index l accounts for the contribution of the partial modes: $l = 1$ corresponds to the dipole mode, $l = 2$ to the quadrupole, $l = 3$ to the octupole and so on. When small nanoparticles (diameter $<< \lambda$) are considered only the electric dipole presents a significant contribution. However, when larger MNPs are considered, high order terms need to be taken into account. Figure 28 plots absorption (red line), scattering (orange line) and extinction (wine line) cross sections calculated for gold MNPs with radius a = 25 *nm* (Figure 28(a)) and a = 45 *nm* (Figure 28(b)). The scattering cross section is negligible for small Au MNPs. However, this contribution cannot be neglected when the MNPs radius reaches 25 *nm* (Figure 28(a)), and dominates in the extinction coefficient for a radius of 45 *nm* (Figure 28(b)). This is due to the fact that scattering grows superlinearly with the size while absorption grows linearly (see equations 3.2-3.4). In addition, it is worth mentioning that the plasmon resonance red shifts with increasing the MNPs size (see Figure 28).
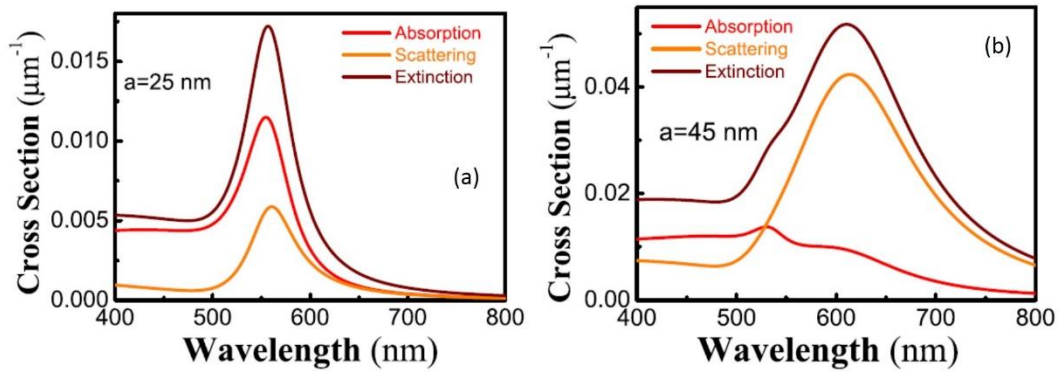
Figure 28. Extinction (wine), absorption (red) and scattering (orange) cross sections calculated from Mie theory for spherical Au MNPs with (a) 25 and (b) 45 *nm* radii.

The same calculation was performed for the 100 *nm* Ag MNPs. Here, to better reproduce the experimental conditions we have taken into account different surrounding media: air ($n_m = 1$, Figure 29(a)) and PMMA ($n_m \approx 1.5$, Figure 29(b)).
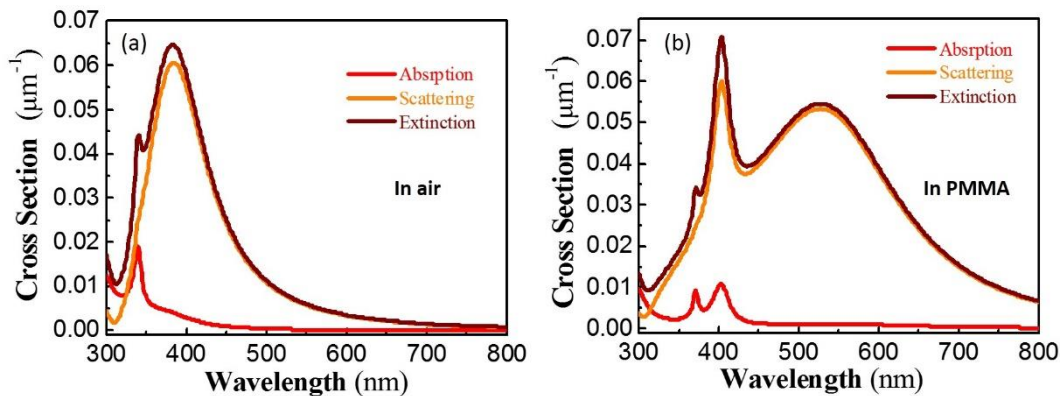
Figure 29. Extinction (wine), absorption (red) and scattering (orange) cross sections calculated from Mie theory for 100 *nm* spherical Ag MNPs surrounded by (a) air ($n_m = 1$) and (b) PMMA ($n_m \approx 1.5$).

3.2.2 Au-Novolak (Nv) nanocomposite

Nanocomposite fabrication

Au MNPs-Nv nanocomposite films were prepared following the procedure explained in [92]. Initial gold seed solutions were made by mixing Nv photoresist with different volume ratios of initial solutions of Nv to Au salt in the proportions 1:1, 1:0.1 and 1:0.01. The initial Nv solution was the commercial ma-P1275 resist from "micro resist technology", and the initial Au solution was 0.197 *g* of

HAuCl$_4$-3H$_2$O 0.1 M dissolved in 0.5 ml of Methoxy propyl acetate (MPA). Then the Au-Nv suspension was spin coated on the appropriate substrate and post-baked at 180 $°C$ for 10 min to initiate the formation of Au MNPs in Nv. At the end of the process 100-200 nm thick films containing Au MNPs of around 10 nm in diameter were synthesized.

To increase the size of the seed gold nanoparticles the nanocomposite was immersed in a "growing" solution containing H$_3$NOHCl with a gold precursor in ethanol. The growth reaction was carried out at a controlled temperature of 45 $°C$ from *minutes* to several *hours* until the desired nanoparticle size was reached.

Nanocomposite deposition

Au MNPs-Nv nanocomposites films were fabricated by following the next steps:

(i) The Au-Nv nanocomposite was deposited by spin coating on a desired substrate (glass, silicon, SiO$_2$/Si) and then baked at 65 $°C$ for two *minutes*.

(ii) The nanocomposite was patterned, by UV-lithography in order to define the zones containing MNPs in the final waveguide (see section 2.1.2).

(iii) Sample was post-baked at 180 $°C$ for 10 *minutes* to initiate the formation of MNPs.

(iv) Sample was immersed in the growing solution until the MNPs reached the desired size.

Nanocomposite characterization

Au MNPs-Nv nanocomposites were initially deposited on glass and silicon substrates (Figure 30) in order to analyse their optical properties. For this purpose, transmission (glass substrate) and reflectivity (silicon substrate) were studied after

each growth step in order to correlate with the morphology characterization shown in Figure 31. Initial seed concentrations of 0.4, 0.04 and 0.004 *g/ml* leaded to 10 *nm* MNPs dispersed in the polymer with filling factors of 10^{-3}, $5 \cdot 10^{-4}$, 10^{-4} respectively, as deduced from SEM images. When these nanocomposite films were immersed in the growing solution, the size of the Au MNPs increase progressively with the immersion (growth) time (Figure 31) from 10 (in the initial nanocomposite) to 100 *nm* (practically completed gold layer), with an average 10 *%* of size dispersion [77]. SEM images presented in Figure 31 correspond to Au MNPs-Nv acquired at different growth times (0, 6, 12 and 22 *hours*) for an initial *ff* of $5 \cdot 10^{-4}$ (nanocomposites fabricated with other concentrations demonstrated similar behaviors).
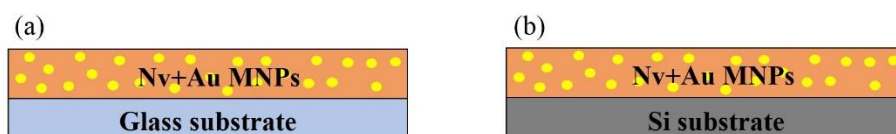

Figure 30. Novolak-gold nanocomposite deposited on (a) glass and (b) silicon substrate for the characterization of its optical properties.
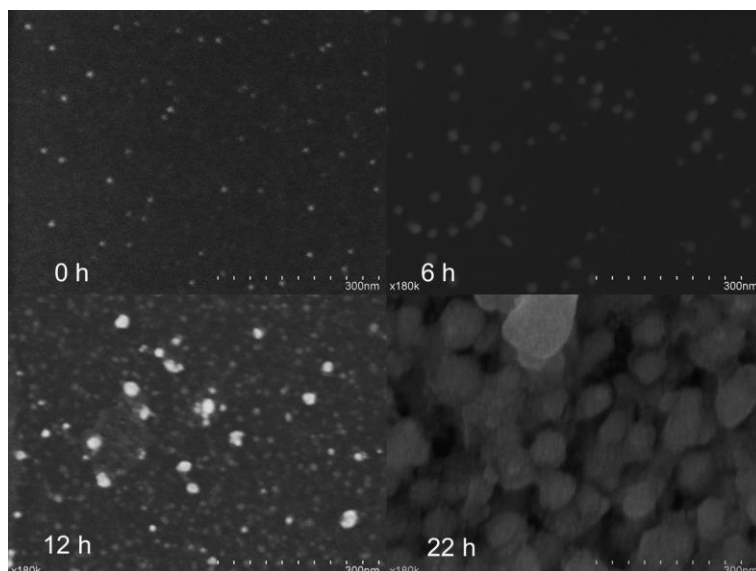
Figure 31. SEM images of Au MNPs obtained after different growing times for the composite with an initial *ff* around $5 \cdot 10^{-4}$.
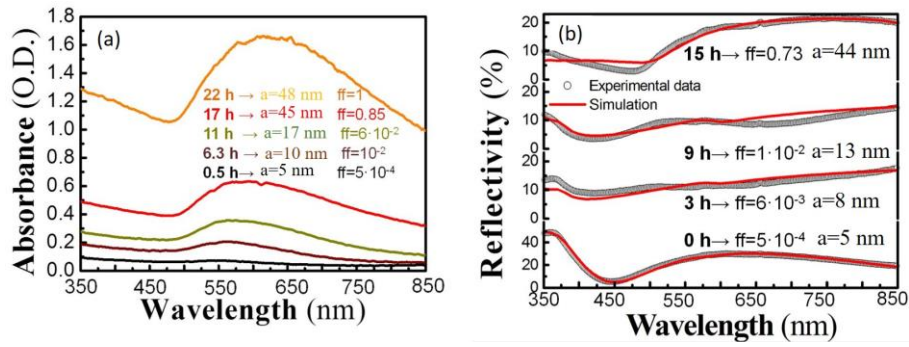
Figure 32. (a) Absorbance and (b) Reflectivity spectra of the Au-NV nanocomposite ($5 \cdot 10^{-4}$ of initial filling factor of Au MNPs) deposited on glass and silicon for absorbance and Reflectivity, respectively. Symbols and red lines in (b) correspond to experimental data and calculated curves.

Transmission and reflectivity spectra, studied after each growing time, agree with the morphological characterization. Figure 32(a) plots the experimental absorbance spectra for a sample with an initial $ff = 5 \cdot 10^{-5}$ and growth times between *1.5* and *22 hours*. The absorbance is negligible at the beginning of the process (black curve), but it increases progressively with the growth time. The maximum of the absorbance corresponds to the localized surface plasmon resonance (LSPR) of the Au MNPs and experiences a red-shift with the size of the MNPs, in agreement with previous publications [93-95] and the calculation presented in the section 3.2.1 [77]. Reflectivity spectra demonstrates a similar behavior: influence of Au is negligible at the beginning of the process (see Figure 32(b)), but the film is practically formed by gold for long growth times (see Figure 32(b)). Au MNPs composite samples with $ff = 10^{-3}$ and $ff = 10^{-4}$ showed similar curves.

Refractive index of the nanocomposite

A Maxwell-Garnett effective medium approximation [96] was chosen to reproduce the reflectivity spectra (red curves in Figure 32(b)) by estimating refractive index of the layer by means of the following equation:

$$\left(n_{eff}\right)^2 = \varepsilon_{eff} = \varepsilon_{Nv} \cdot \frac{L_i \cdot (\varepsilon_{MNPs} - \varepsilon_{Nv}) + \varepsilon_{Nv} + ff \cdot (\varepsilon_{MNPs} - v) \cdot (1 - L_i)}{L_i \cdot (\varepsilon_{MNPs} - \varepsilon_{Nv}) + \varepsilon_{Nv} - ff \cdot (\varepsilon_{MNPs} - \varepsilon_{Nv}) \cdot L_i}$$

(3.5)

where ε_{Nv}, ε_{MNPs} and ε_{eff} are the dielectric constants of the surrounding medium (Nv), MNPs and the nanocomposite, respectively. L_i refers to the depolarization factors along each axis (1/3 in spherical shape) [94, 95]. Refractive index of the Nv has been experimentally obtained by fitting the reflectivity of Nv films of thicknesses between *0.5* and *2 μm* on silicon substrates:

$$n_{Nv}(\lambda) = 1.6 + 65e^{-\lambda/47} + 0.29e^{-\lambda/400}$$

(3.6)

where λ is the wavelength in *nm*. The dielectric constant of MNPs is approximated by taking into account the free and the bound electrons of the metal [91, 97-101]:

$$\varepsilon_{MNPs} = \varepsilon_{free-e^-} + \varepsilon_{bound-e^-}$$

(3.7)

The first term is usually calculated by Drude's model and the second term by the expression proposed in [98, 99]:

$$\varepsilon_{free-e}(\omega) = 1 - \frac{\omega_p^2}{\omega^2 + i(\Gamma_{bulk} + C \cdot v_f/a) \cdot \omega}$$

(3.8)

$$\varepsilon_{bound-e}(\omega) = Q_{bulk} \int_{\omega_g}^{\infty} \frac{\sqrt{x - \omega_g}}{x} [1$$

$$- F(x, E_F, T)] \frac{(x^2 - \omega^2 + \gamma_b^2 - i2\omega\gamma_b)}{(x^2 - \omega^2 + \gamma_b^2)^2 + 4\omega^2\gamma_b^2} dx$$

(3.9)

where ω_p is the plasma frequency set to $13 \cdot 10^{15}$ Hz [98-100], Γ_{bulk} the bulk damping constant considered to be $1.1 \cdot 10^{14}$ Hz [100], v_f the electrons velocity at the Fermi surface (14.1 nm/s) [98], C a constant set to 1 [91], $F(x, E_F, T)$ the Fermi energy distribution function at the temperature T and the Fermi energy $E_F = 2.5$ eV [98], E_g the energy gap of Au ($E_g = 2.1$ eV) [98], γ_b the damping constant in the intraband transitions ($2.4 \cdot 10^{14}$ Hz) and Q_{bulk} a proportionality factor ($Q_{bulk} = 2.3 \cdot 10^{24}$) [98]. Due to the fact that Au is an absorbing material dielectric constant of the MNPs, as well as the dielectric constant of the effective medium (equation 3.5), is a complex number. Equations 3.8 and 3.9 agrees with the experimental values of the dielectric constant of bulk gold obtained from [102] (black hallow circles in Figure 33). In addition, the proposed model (solid lines in Figure 33) reproduces the experimental data (symbols in Figure 33).
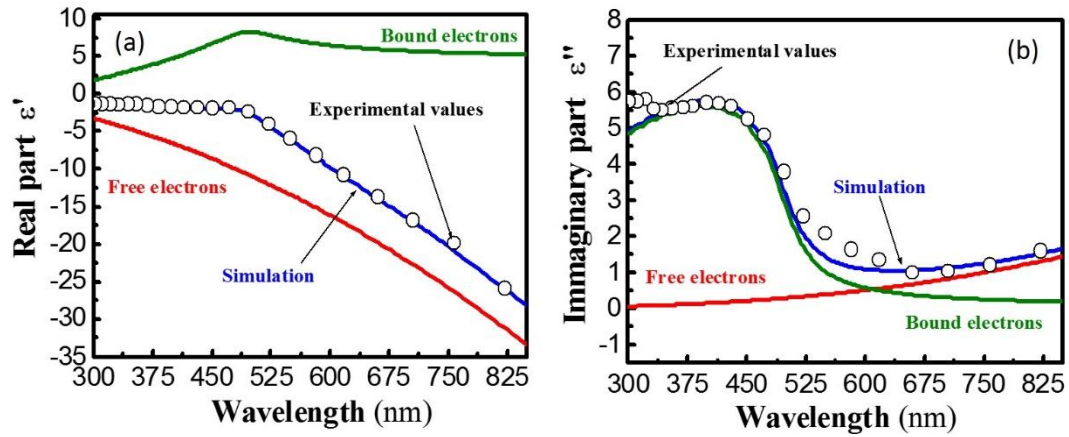
Figure 33. Calculated (lines) and experimental values taken from [102] (allow circles) of the (a) real and (b) imaginary part of the bulk gold dielectric function.

Figure 34 shows the *ffs* and radius deduced from the reflectivity fitting as a function of the growing time for the three concentrations studied (initial filling factor of *10⁻³, 5·10⁻⁴, 10⁻⁴*). The size of Au MNPs slowly increases with the growing time until a certain threshold is reached, above which their size grows faster until a continuous gold film is formed for *ff > 0.5*. The decrease of the

threshold with the initial concentration of the MNPs in the composite is probably related with the easiness of the nanocomposite film to incorporate neighbouring Au atoms when there is a high amount of metal on its surface. The size of the MNPs saturates with regrowth to a diameter of 40 *nm* for the nanocomposite with the smallest Au concentration (wine symbol in Figure 34). For higher initial concentration of MNPs (red and orange symbols in Figure 34) the MNPs size can be controlled between 10 *nm* and 100 *nm* upon regrowth time.
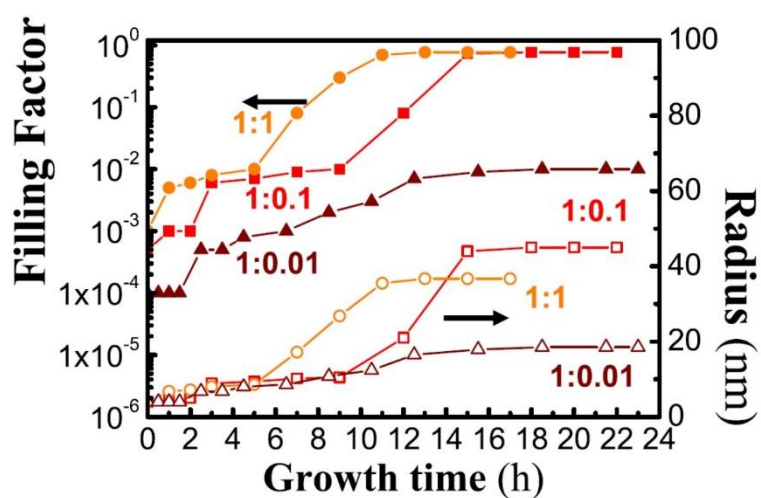
Figure 34. Filling factor (left axis and filled symbols) and radius (right axis and hallow symbols) deduced from the modelling as a function of the growth time. Orange, red and wine colures refer to an initial Nv/Au volume radius of 1:1, 1:0.1 and 1:0.01 respectively (initial *ffs* of 10^{-3}, $5 \cdot 10^{-4}$, 10^{-4}).

3.2.3 Integration of MNPs in waveguides

This section illustrates the fabrication procedures used to incorporate the MNPs in polymer waveguides.

Au MNPs-Nv nanocomposite

First, the nanocomposite was deposited on a SiO_2/Si substrate following the procedure explained section 3.2.2. Then, a PMMA layer was spin coated on the top of the nanocomposite, and post baked at 80 *°C* and 150 *°C* for two *minutes*

each temperature [34]. The thickness of this layer was around 2 *μm* in order to allow the propagation of guided modes.

Silver MNPs

Commercial MNPs used in this Thesis were supplied by Nanocomposix, and consisted of silver spheres of *100 nm* diameter diluted in water at *0.020 mg/ml* (corresponding to a particle density of *3.6·10^9 particles/ml*) and coated with polyvinylpyrrolidone (PVP, negatively charged) to prevent aggregation. They were deposited by dropping the solution on the appropriate substrate, and baked at 50 *°C* for 30 *minutes* to control the evaporation rate. For this purpose, an intermediate layer of the commercially available polymer electrolyte Omnicoat (from Microchem Corp.) is spin coated and baked at 180 *°C* for 1 *minute* in order to improve the adhesion of the MNPs on the substrate. In these conditions, quite homogeneous layer of MNPs with a *ffs* between *1 %* and *10 %* (controlled by the concentration of the solution) were obtained (see SEM images in Figure 35)
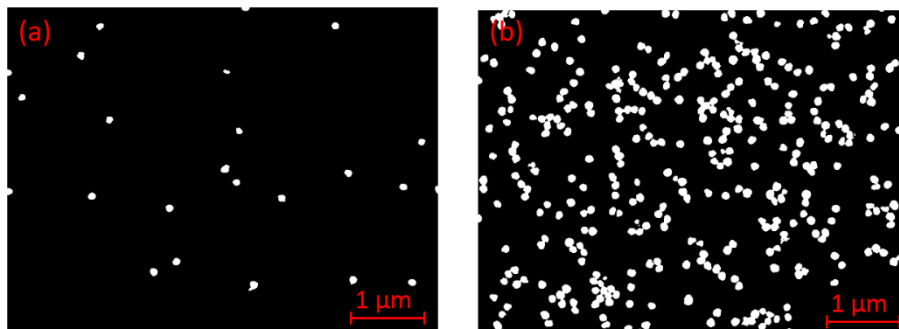
Figure 35. SEM images of Ag MNPs deposition on Si substrate with drop casting, from (a) a ten times diluted or (b) the initial concentration.

Again, deposition of MNPs is followed by spin coating a PMMA or PMMA-PDI film with the intention to conform a planar waveguide.

3.2.4 Coupling normal incident light by MNPs

Au MNPs-Nv nanocomposites were applied as integrated optical waveguide couplers by exploiting their high scattering cross sections. For this purpose, the nanocomposite is patterned inside the waveguide structure in order to redirect normal incident light into the waveguide modes, as schematically illustrated in Figure 36.
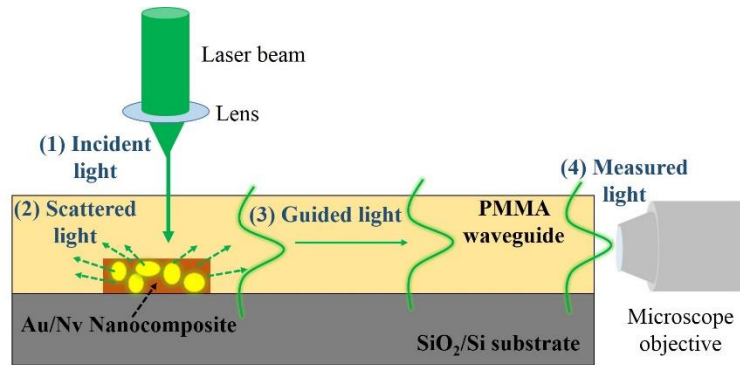
Figure 36. The sample structure and experimental setup. Au MNPs/Novolak nanocomposite is patterned on a SiO_2/Si wafer and a PMMA film is deposited on the top. An incident laser beam (1) is focused on the surface of the nanocomposite for scattering the light by the MNPs (2). Finally, the scattered light is coupled to the guided modes (3) of the PMMA/SiO_2 structure and collected at the output edge of the sample (4).

Figure 37(b) plots the coupling efficiency (calculated by the ratio of the optical power density at the output and input) measured in samples with $ff = 0.01$ (green) and $ff = 0.1$ (blue), for the six different wavelengths (404, 450, 532, 590, 633 and 780 *nm*). Although all wavelengths were successfully coupled in the structure (see top photographs), coupling efficiency demonstrated a strong dependence on the operation wavelength. It was around *1 %* for wavelengths closer to the plasmonic resonance but it dropped down to *0.01 %* for shorter and longer wavelengths. The significant better coupling in TE than in TM polarization (a 3-fold increase in the *550-650 nm* range and about 2-fold out of this range, as observed in Figure 37(c)) is probably due to a the worse matching of the propagating modes in the PMMA and Au-Nv layers, as explained in [77].

73
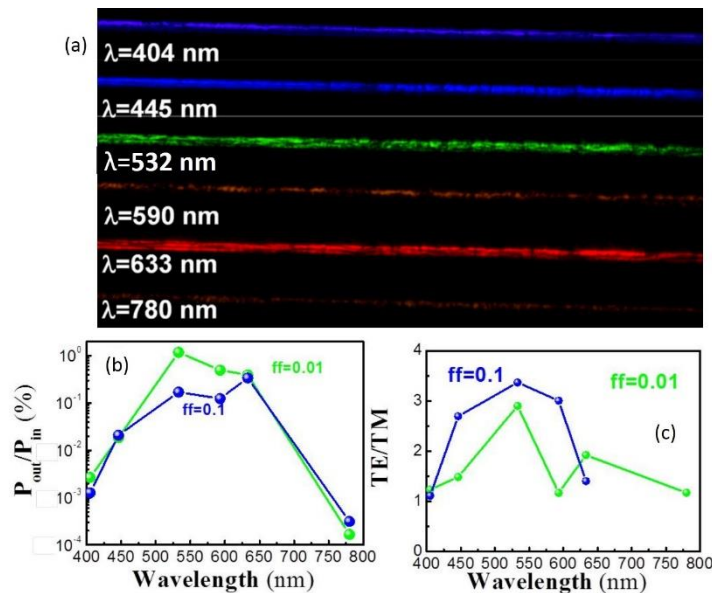
Figure 37. (a) Photographs of light at the output edge of the waveguide for the different wavelengths studied. (b) Coupling efficiency at the output of the waveguide as a function of the wavelength. (c) Ratio between TE and TM light at the output of the waveguide.

3.3   Interaction between MNPs and PDI compounds

MNPs are integrated together with PDI compounds in order to study the influence of the nanoparticles in the generation of PL. In particular, this work was focussed in finding the optimum conditions to observe an enhancement of the spontaneous emission (section 3.3.1), and implement a laser based on random distributed scatters (section 3.3.2).

3.3.1   Enhancement of photoluminescence.

Optical properties of an oscillator in close proximity to MNPs can be influenced by the plasmonic resonance or the high near field at the surface of the nanostructures. As a consequence, the hybrid plasmonic-emitter system demonstrates different optical properties than the isolated individual elements, giving rise to outstanding applications. This section studies a weak coupling interaction between PDI compound and MNPs able to enhance the PL emitted by the organic compound. For this purpose, silver nanoparticles have been chosen as

nanostructures with high scattering cross section and spectral overlap of the plasmonic resonance with the PL of the PDI (see Figure 38). Furthermore, the separation between the MNPs and the molecule [103] has to meet a critical distance to have the best interaction between these two elements.
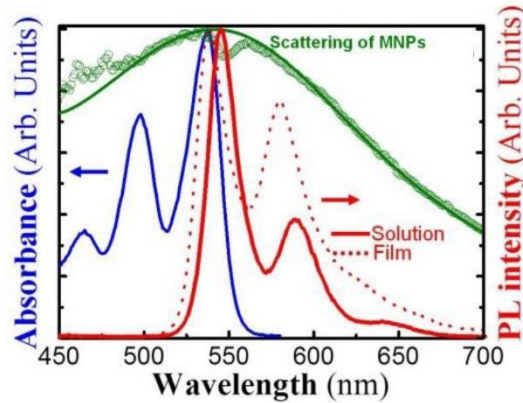
Figure 38. Absorbance (blue line and left axis) and PL intensity (red line and right axis) of the PDI-1. Dotted line shows the PL intensity of the PDI-1 embedded in PMMA. Green symbols present the measured scattering of the Ag nanoparticles which are in agreement with the theoretical predictions (green line) calculated with equation 3.3.

Then, silver MNPs have been integrated together with PDI following the procedure described in section 3.2.3. For this purpose, a thin ($\approx$ *50 nm*) PMMA-PDI nanocomposite is deposited on the appropriate substrate and covered with a layer of MNPs with an intermediate Omnicoat film to improve adhesion. Here the concentration of PDI in the polymer was fixed down to *0.06 % wt.* in order to avoid aggregation and to keep a similar concentration of emitter oscillators and MNPs (see Figure 39(a)).

Finally, it is worth mentioning that the size of the drop (around *0.5 cm^2*) was smaller than the sample ($\approx$ *1.5 cm^2*), and hence two distinguishable regions, with and without MNPs, were defined for studying the influence of MNPs on the emission of PDI-1 molecules referred to the region without nanoparticles.
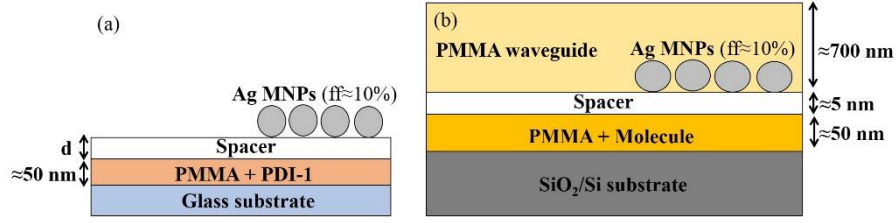
Figure 39. Sample structure to study exciton-plasmon interaction on: (a) glass substrates for measuring transmission and forward-scattering PL for different spacer thickness between the molecule and the MNPs and (b) on SiO₂/Si substrates for the study of waveguided PL.

The same procedure was used to fabricate waveguide samples on SiO$_2$/Si substrate with the obtained optimum spacer thickness. Here, on top of the MNPs, a PMMA layer was spin coated and post baked at at 80 *°C* and 150 *°C* for two *minutes* each bake. Final thickness was around 700 *nm* to act as the core of the waveguide (Figure 39(b)).

Theory of exciton-photon enhancement

We studied the PL enhancement factor, *F*, as a function of the MNPs-dye separation following the model proposed in [91, 104-106]:

$$F = G(\omega)Q(\omega')$$

(3.10)

Where *G* is the incident field enhancement factor, *Q* the quantum yield of the molecule and ω, ω' the incident light frequency and the frequency of the emitted radiation respectively. From the Electromagnetic theory the quantum yield can be calculated from:

$$Q(\omega', r) = \left(\frac{\gamma_{rad}(\omega', r)}{\gamma_0}\right) \Big/ \left(\frac{\gamma_{tot}(\omega', r)}{\gamma_0}\right)$$

(3.11)

where r is the length of the radius vector plotted from a particle centre to the molecule position, $\gamma_{rad}(\omega',r)/\gamma_0$ and $\gamma_{tot}(\omega',r)/\gamma_0$ are the radiative and the total components of the decay rate of the molecule respectively calculated as:

$$\frac{\gamma_{rad}(\omega',r)}{\gamma_0} = \frac{3}{2(kr)^4} \sum_{n=1}^{\infty} n(n+1)(2n+1) \cdot |\psi_n(kr) + b_n\zeta_n(kr)|^2$$

(3.12)

$$\frac{\gamma_{tot}(\omega',r)}{\gamma_0} = 1 + \frac{3}{2(kr)^4} \sum_{n=1}^{\infty} n(n+1)(2n+1) \cdot Re\{b_n\zeta_n(kr)^2\}$$

(3.13)

here $k = \omega'/c$ is the wavenumber, $\psi_n(kr) = (\pi kr/2)^{1/2}J_{n+1/2}(kr)$ with $J_{n+1/2}(kr)$ being the spherical Bessel Function, $\zeta_n(kr) = (\pi kr/2)^{1/2}H^{(1)}_{n+1/2}(kr)$ with $H^{(1)}_{n+1/2}(kr)$ being the spherical Henkenl Function of the first kind and b_n and a_n the Mie coefficient defined as:

$$b_n = -\frac{\sqrt{\varepsilon}\psi_n(k_0a\sqrt{\varepsilon})\psi_n'(k_0a) - \psi_n(k_0a)\psi_n'(k_0a\sqrt{\varepsilon})}{\sqrt{\varepsilon}\psi_n(k_0a\sqrt{\varepsilon})\zeta_n'(k_0a) - \zeta_n(k_0a)\psi_n'(k_0a\sqrt{\varepsilon})}$$

(3.14)

$$a_n = -\frac{\psi_n(k_0a\sqrt{\varepsilon})\psi_n'(k_0a) - \sqrt{\varepsilon}\psi_n(k_0a)\psi_n'(k_0a\sqrt{\varepsilon})}{\psi_n(k_0a\sqrt{\varepsilon})\zeta_n'(k_0a) - \sqrt{\varepsilon}\zeta_n(k_0a)\psi_n'(k_0a\sqrt{\varepsilon})}$$

(3.15)

Where a is the metal particle radius and ε is its dielectric permittivity (depending on ω) and $k_0 = \omega/c$ is the wavenumber. The Factor G is calculated by averaging all the possible orientation of the molecules, in our case for molecules on glass we assume, as in [106], that:

$$\langle G(\omega, \boldsymbol{r})\rangle = \frac{1}{2(kr)^4} \sum_{n=1}^{\infty} n(n+1)(2n+1) \cdot |\psi_n(kr) + b_n \zeta_n(kr)|^2$$

$$+ \frac{1}{2(kr)^2} \sum_{n=1}^{\infty} (2n+1) \cdot (|\psi_n(kr) + a_n \zeta_n(kr)|^2$$

$$+ |\psi_n'(kr) + b_n \zeta_n'(kr)|^2)$$

(3.16)

As discussed below this model is able to reproduce the experimental results on the PL enhancement by Purcell effect. The maximum enhancement factor is found for a separation ($d = r - a$) around *6 nm.*

PL enhancement in forward-scattering configuration

As it has been studied in the last section, the gap between the active material and MNPs has a direct influence in the enhancement of PL. If this gap is too short the emission is quenched by ohmic losses, while if it is too long there is no interaction between the MNPs and the emitter [103]. For the optimum gap the weak coupling between the exciton and the plasmon results in a reduction of the radiate recombination time, and hence in an enhancement of the PL.

In this way, the Omnicoat film, not only serves to obtain a homogenous layer of MNPs, but also plays an important role in the enhancement of PL. Then, the influence of the thickness of this spacer was properly studied in order to find the optimum conditions for light generation. For this purpose, the nanocomposite/omnicoat/MNPs multilayers were deposited on glass substrates, and characterized by measuring the PL and TRPL in transmission and forward-scattering configuration (see section 2.2.2).

The enhancement of the PL intensity with MNPs reveals a direct dependence on the spacer gap, *d.* Although there is no influence for thin (*d < 2.5 nm*) or thick layers (*d > 10 nm,* Figure 40(a)), PL increases by 4-6 fold

enhancement when a gap $d = 5\text{-}10$ *nm*, (Figure 40(b)) is chosen. This enhancement can be explained by the influence of scattering mechanisms or a modification of the radiative spontaneous emission rate [107].
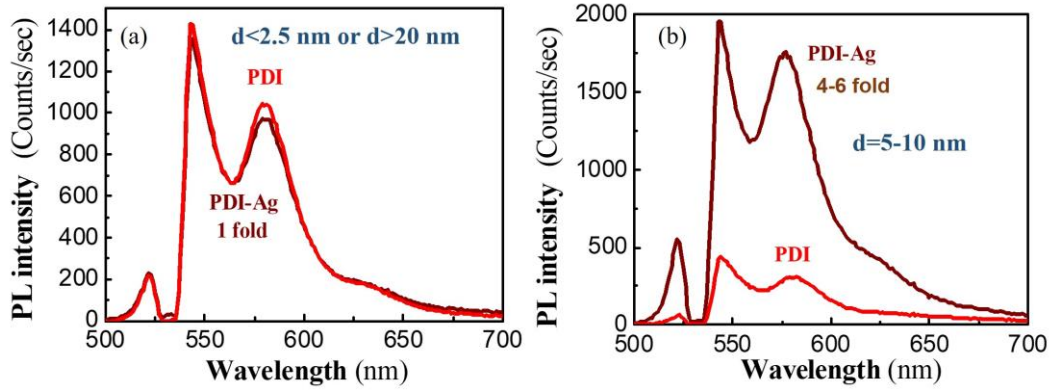
Figure 40. Average PL intensity measured in forward scattering with (wine) and without MNPs (red) for spacer thickness *d* of (a) 0, 2.5 and 20 *nm* and (b) 5 and 10 *nm*.

TRPL measurements (measured with the Nd:YAG laser doubled at 532 *nm* with a repetition rate of 20 *KHz* and pulse width of 1.2 *ns*) corroborate the enhancement observed at the optimum gap. Figure 41(a) shows the TRPL measurement in absence of MNPs (red) and with MNPs and a spacer of $d = 5$ *nm*. Symbols and solid lines correspond to experimental data and fitting respectively. The grey area presents the response of the system. As already introduced in section 3.1.1 we can fit the PL transients of the molecule dispersed in solution (yellow in Figure 17) and deposited as films (red in Figure 17) with single exponential decay functions (solid lines in Figure 17). Here the best fitting decay times were 6.0 ± 0.2 *ns* and 2.7 ± 0.3 *ns* for solution and film, respectively. This reduction in the decay time can be attributed to some non-radiative channel present in the PMMA-PDI film that was absent or negligible in solution. The effective recombination decay time (τ_{eff}) deduced from TRPL is the combination of radiative (τ_r) and non-radiative (τ_{nr}) contributions $1/\tau_{eff} = 1/\tau_r + 1/\tau_{nr}$. If τ_r is assumed to be close to that of the solution (6 *ns*), τ_{nr} would be around *5 ns*. From

these values, an emission quantum yield, $QY = \tau_{nr}/(\tau_{nr}+ \tau_r) \approx 45\ \%$, can be estimated for the film, which is very close to the *QY* measured with the commercial system (see section 3.1.1). Whit this consideration we calculate the radiative decay time of the molecule in the presence of the MNPs with a total spacer of *6.5 nm (d = 5 nm)*. In this conditions we obtained a decay time of *0.8 ± 0.1 ns* (red line in Figure 41(a)). The reduction in the PL lifetime, so obtained, is attributed to a Purcell mechanism, where the gain in the spontaneous emission rate (or Purcell Factor, *PF*) is known to be the ratio between both radiative time constants.

$$PF = \frac{\tau_{PDI}}{\tau_{PDI-Ag}}$$

(3.17)

In our calculation we assumed that the Purcell effect only affect to the emitted radiative rate [78]. Under this assumption, we have a Purcell factor around 5.5, for the optimum omnicoat thickness of *d = 5 nm* [78]. This value is very close to the measured intensity enhancement (Figure 40(b)) and to the theoretical curve (red line in Figure 41(b)) calculated from the model proposed in [91, 104-106] (equation 3.10). It is worth mentioning that we did not observe any total PL quenching with *d = 0 nm*, as one should have expected [103], because the non-radiative complete quenching of PL is prevented by the *1-2 nm* ligands covering the surface of the MNPs, providing an effective thicker spacer that have been taken into account in the x-axis of Figure 41(b), and the main contribution to the TRPL curve of organic molecules far from MNPs, which is the reason to find $PF = 1$.
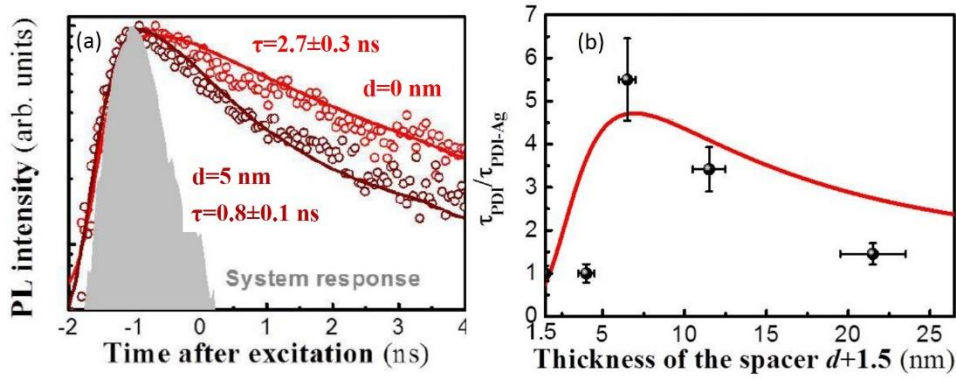
Figure 41. (a) TRPL measurement in absence of MNPs (red) and with MNPs and a spacer of $d = 5$ *nm*. Symbols and solid lines correspond to experimental data and fitting respectively. Grey area presents the response of the system. (b) Shortening of the PL decay time as a function of the thickness of the spacer. Symbols and solid red line refers to experimental data and modelling, respectively.

PL enhancement in optical waveguides

PL intensity was measured in the waveguide configuration shown in Figure 39(b) by using the setup described in section 2.2.2 (VSL method). This experimental setup allows uniform excitation of the pump beam (C.W. 532 *nm*) along the whole length of the waveguide.

Figure 42(a) presents the PL spectra obtained at the output edge of the sample under (wine line) or without (red line) the influence of MNPs. Here the PL intensity was enhanced by a factor 4.5, approximately, close to that found by forward scattering geometry (not limited by losses). However, in this case the PL intensity is influenced not only by the interaction with the MNPs plasmon, but also by the propagation losses in the waveguide, mainly introduced by the MNPs. Then, the exciton-photon coupling overcomes the additional attenuation in the structure.

TRPL experiments were carried out by end fire coupling the excitation beam at the input edge of the waveguide and collecting the PL from the output edge. In the region without MNPs the PL kinetics experiments show a decay time of *2.0 ± 0.1 ns* (red symbols and solid line in Figure 42(b)), close to the previous measurements in PMMA-PDI-1 films possibly reduced by the light confinement

in the waveguide [76]. Nevertheless, the influence of MNPs in the waveguide geometry (wine symbols and solid in Figure 42(b)) reveals a more important reduction of the decay time down to *0.30 ± 0.05 ns*. Again, these decays correspond to radiative exciton lifetimes $\tau_r = 0.32$ *ns* and $\tau_r = 3.4$ *ns* with and without MNPs, respectively, by taking into account the same nonradiative recombination $\tau_{nr} = 5$ *ns* [78]. Thus, the MNPs-dye coupling in the waveguide geometry leads to a Purcell factor as high as 10.5, i.e., a factor two larger than that obtained in forward-scattering geometry. This enhancement of Purcell effect can be attributed to the high confinement of the light in the core of the waveguide, as compared to light emission into air, as it has been proposed in metal-insulator-metal structures [108], and demonstrates the benefit of the proposed waveguide geometry is not only to study the enhancement of PL, but also to exploit it in integrated photonic devices.
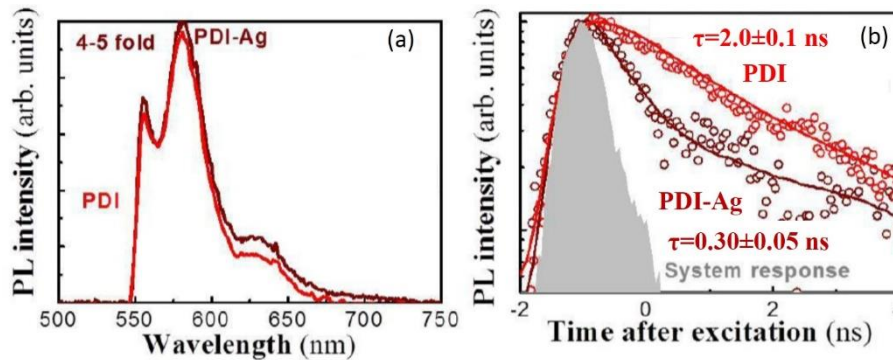
Figure 42. (a) PL intensity measured at the edge of the waveguide with (wine) and without MNPs (red). (b) Recombination time measured at the edge of the waveguide with the PDI uncovered (red) and covered (wine) by Ag MNPs. Symbols correspond to the experimental data and solid lines to the exponential fitting. Grey area shows system response.

3.3.2 Random distributed feedback laser

The last target of this Ph.D. has been the demonstration of laser operation by using PMMA-PDI nanocomposites as a gain media, and nanoparticles with high scattering cross section at the PL wavelengths as a randomly distributed feedback material. Samples consisted of 1 *μm* thick PMMA-PDI-1 nanocomposite spin

coated on the top of the nanoparticles film (as illustrated in Figure 43), previously deposited with the method explained in section 3.2.3. Concentration of PDI in the PMMA was fixed up to *5 % wt.* in order to achieve gain generation conditions. In addition, two different kinds of nanoparticles with high scattering cross section at the PL wavelengths were tested:

(a) Commercial Silver MNPs of *100 nm* diameter (described in section 3.2.3).

(b) Commercial spherical TiO_2 nanoparticles (NPs) of *140 nm* diameter (Titanix JR-600E from Specialchem, Japan) dissolved in water (with TiO_2 mass concentration of 0.020 *mg/ml*).
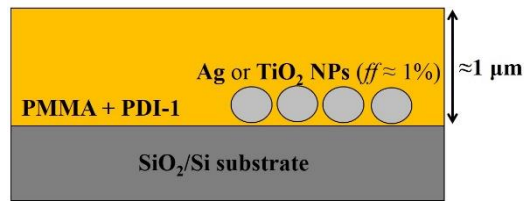
Figure 43. Scheme of the samples used to study random lasing operation.

Samples were characterized by optically pumping the active medium with a pulsed Nd:Yag laser doubled to *532 nm* with a repetition rate of *10 Hz* and a pulse width of *1 ns* (Energy pulse *30 μJ*). Here a pulse frequency of *10 Hz* was used to reduce heating and consequently reduce the damaging of the samples. Also for this purpose, the radius of the spot on the surface of the sample was increased to around *1 mm*. Then, the PL signal was collected into a commercial Ocean Optics MAYA2000 pro spectrometer (with a resolution of ≈ *0.1 nm*).
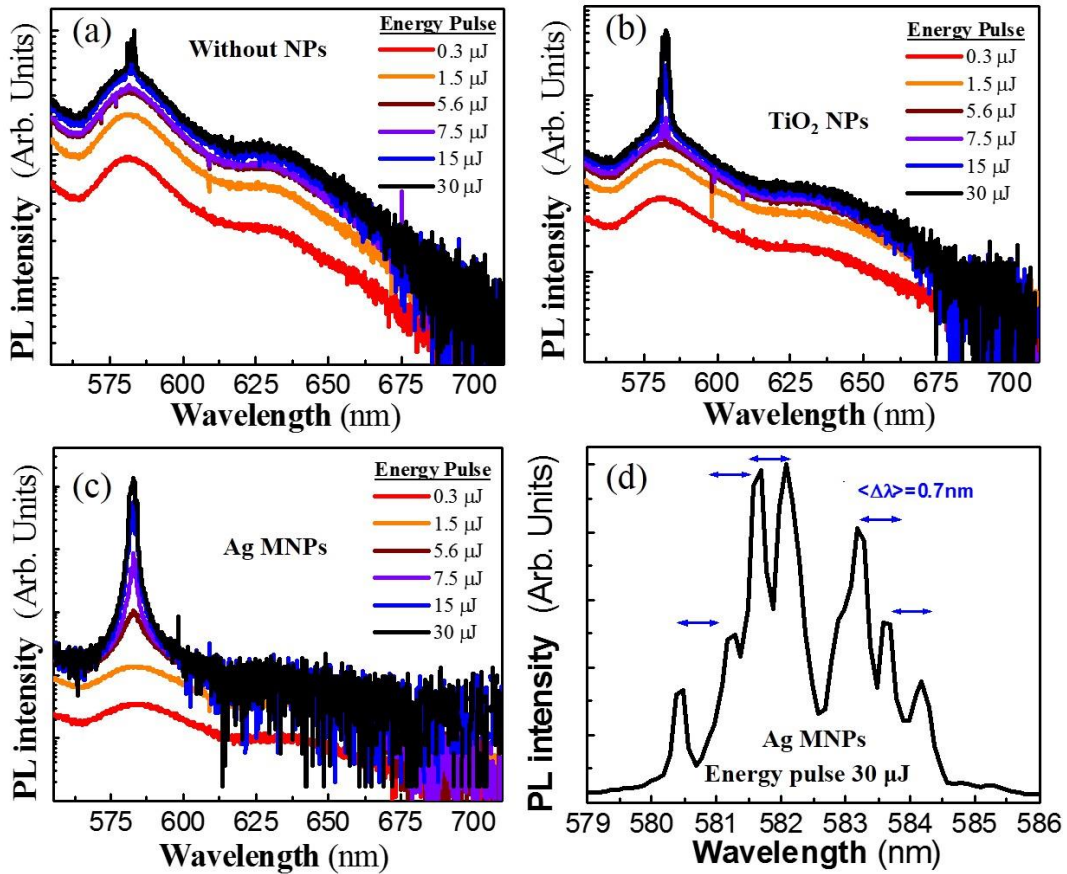
Figure 44. PL spectra for different pump energy for the sample (a) without nanoparticles, (b) with TiO$_2$ NPs and (c) with the Ag MNPs. (d) Zoom of the PL spectrum of the sample with Ag MNPs at maximum pump energy (30 μJ).

In Figure 44(a)-(c) are reported the PL spectra obtained for sample without NPs (a) with TiO$_2$ NPs (b) and with Ag MNPs (c) for different pump fluencies. Here we can see that at high pump fluency the PL peak collapse into a narrow line, typical signature of optical gain (ASE).

Figure 45 and Figure 46 show log-log plots of the integrated PL intensity and the PL linewidth as a function of the excitation fluency. Red, blue and black symbols refer to Ag MNPs, TiO$_2$ nanoparticles and the region without nanoparticles, respectively. Although ASE is demonstrated for the three conditions, the nanoparticles reveals an important influence. First TiO$_2$ shows a decrease of the ASE threshold by a factor four as compared to the case without nanoparticles. In the case of using silver MNPs the PL spectrum evolution with the laser excitation fluency (red symbol in Figure 45 and Figure 46) indicates

84

three different regions [109]. Below a threshold of *2 μJ* light is predominantly spontaneously emitted [110] with a linear dependence of the PL intensity with the excitation fluency and a nearly constant linewidth. When the excitation fluency is increased above the ASE threshold of *2 μJ* the integrated PL intensity shows a superlinear increase with the excitation power, and the PL spectrum collapses into a narrow line, which is characteristics of the ASE regime. Finally, at excitation higher than *10 μJ*, the PL intensity, again, reveals a linear dependence with the excitation pump energy, and the linewidth of the PL line continues to decrease slowly and it is composed of several narrow peaks (see Figure 44(d)). This S-curve characteristics of the PL-intensity log-log plot, together with presence of such narrow peaks in the PL spectrum, are clear indications of laser operation, and hence it is attributed to a random distributed feedback. Table IV summarizes the optical properties of these devices.
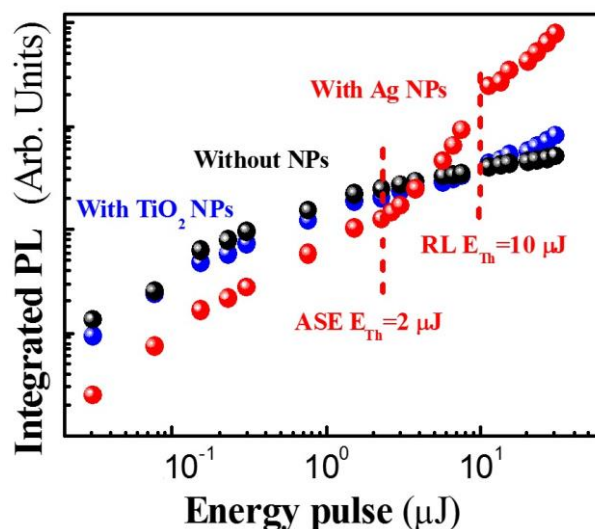
Figure 45. Integrated PL intensity of the samples with Ag MNPs (red symbols), with TiO_2 NPs (blue symbols) and without NPs (black symbols), as a function of the excitation fluency. Labels indicates threshold of ASE and lasing for the sample with Ag MNPs.

85
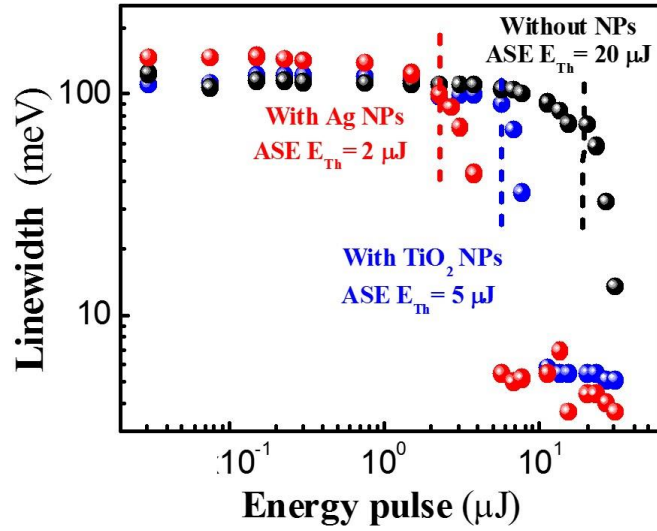
Figure 46. PL peak linewidth of the samples with Ag MNPs (red symbols), with TiO$_2$ NPs (blue symbols) and without NPs (black symbols), as a function of the excitation fluency. Labels indicates threshold of ASE.

Figure 44(d) shows a zoom of the PL spectra at maximum pump fluency (30 μJ) centred on the PL peak for the sample with the Ag MNPs. Clearly, here, there are narrow peaks superimposed to the PL, which are attributed to random lasing generation. Since the average separation between the resonance peaks ($<\Delta\lambda>$) is estimated around *0.7 ± 0.1 nm*, the length of the equivalent Fabry-Perot resonator is found to be about $l = 250 \pm 30 \mu m$, by using the following formula [111]:

$$\Delta\lambda \approx \frac{\lambda_{em}^2}{2n_{eff}cos\theta l}$$

(3.18)

where λ_{em} is the central wavelength of the random laser emission ($\lambda_{em} \cong$ 582 *nm*), n_{eff} the effective refractive index of the medium ($n_{eff} \cong 1.5$), θ the incident angle ($\theta \cong$ *45 degree*).

On the other hand, we can estimate the minimum mean free path length, l_{min}, between consecutive scatters as [112]:

$$l_{min} = 2n_{eff}^2 d/(n_{eff}^2 - 1)^{1/2}$$

(3.19)

86

where d is the thickness of the gain layer ($d \cong 1\ \mu m$). In this way we obtained $l_{min} \cong 4\ \mu m$. Obviously, this minimum mean free path length requires a separation between the silver nanoparticles smaller than $S = l_{min}sin\theta_c \cong 2.6\ \mu m$, where $\theta_c = sin^{-1}(1/n_{eff})$ is the critical angle for the total reflection at the composite/air interface. If a homogeneous distribution of the MNPs with an average ff of 1 % is assumed, we can estimate an average separation about $< S_{MNPs} > \cong 1.3\ \mu m$, and hence fulfils the aforementioned condition. Finally, if we compare this minimum free path length with the equivalent Fabry-Pérot resonator's length l, one would deduce that 50-70 light scattering Ag nanoparticles are needed to form a closed loop path. When the amplification along such a loop path exceeds the loss, laser oscillation can occur in the loop, which serves as a laser resonator [115]. Furthermore the minimum mean free path length (l_{min}) is approximately equal to $7\lambda_{em}$. As it is reported in the experimental works [115, 116] and according to the definition of the free path length of random laser, we can state that this is an excellent relationship to support the lasing action in such a random device.

Table IV. Resume of the optical properties of the devices studied.

NPs	λ_{ASE} (*nm*)	ASE E_{th} (*μJ*)	RL E_{th} (*μJ*)	$\Delta\lambda$ (*nm*)
None	582	20	-	2.7
TiO$_2$	582	5	-	1.0
Ag	582	2	$\approx$10	0.7

Theoretical modelling

Experimental PL intensity, for the sample with the Ag MNPs, at its centred wavelength (582 *nm*, black points in Figure 47) is fitted (solid red line in Figure 47) as a function of the pump fluency with a standard laser model [113, 114]:

$$\frac{dN}{dt} = R_p - \frac{N}{\tau_r} - \frac{N}{\tau_{nr}} - \frac{\Gamma g c (N - N_{tr}) P}{n_{eff}}$$

(3.20)

$$\frac{dP}{dt} = \frac{\Gamma \beta N}{\tau_r} - \frac{N}{\tau_c} + \frac{\Gamma g c (N - N_{tr}) P}{n_{eff}}$$

(3.21)

where N and P are number of optically excited molecules and photon densities within the active area, R_P is the pumping rate, g is the differential gain coefficient and N_{tr} is the transparency carrier density, Γ the confinement factor, β the spontaneous emission coupling factor, and τ_c the cavity photon lifetime. The radiative and non-radiative recombination lifetimes are $\tau_r = 6$ *ns* and $\tau_{nr} = 5$ *ns*, respectively, as calculated in [78]. Since the PDI's are embedded in the highest refractive index layer, we believe that the light emitted is mainly coupled to a waveguide mode, and hence $\beta = \Gamma = 1$ is assumed. Then τ_c, g and N_{tr} were used as a fitting parameters with $\tau_c = 70$ *ps*, $N_{tr} = 1.1 \cdot 10^8$ *cm*$^{-3}$ and $g = 3 \cdot 10^{-9}$ cm^2. This differential gain coefficient corresponds to an effective gain (g_{eff}) of $g_{eff} = g/V_a \cong 1 \cdot 10^{-3}$ cm^{-1}, where $V_a = d\pi r^2$ is the active volume where d is the thikness of the active layer (≈ 1 *μm*) and r the radius of the illumination spot (≈ 1 *mm*). These values are in agreement with those found in previous works [114, 117, 118], with the only discrepancy of the low transparency carrier density (N_{tr}) found here, about 6 orders of magnitude smaller than the one reported in [114].

This could be explained by the large Stokes-shift between the 0-1 PL transition and the absorption. Using those values pumping threshold (P_{pth}) can be estimated as [113, 114]:

$$R_{pth} = \frac{(1 - \beta)N_{th}}{\tau_r} + \frac{N_{th}}{\tau_{nr}}$$

(3.22)

$$N_{th} = N_{tr} + \frac{n_{eff}}{\tau_c \Gamma c g}$$

(3.23)

where R_{pth} and N_{th} are the pumping rate and the carrier density, respectively, evaluated at threshold in the steady state, and n_{eff} the effective refractive index of the active medium (≈ *1.50* at *580 nm*). Therefore, it becomes possible to estimate the threshold as $P_{pth} = R_{pth} * E_{ph} = 8.35\ KW$, where $E_{ph} = hc/\lambda$ is the energy of the excitation beam (λ = 532 *nm*). This value corresponds to *8.35 μJ*, by taking in account the width of the pump pulse (1 *ns*), and hence it agrees with the value extracted from the experimental data (≈ 10 *μJ*).
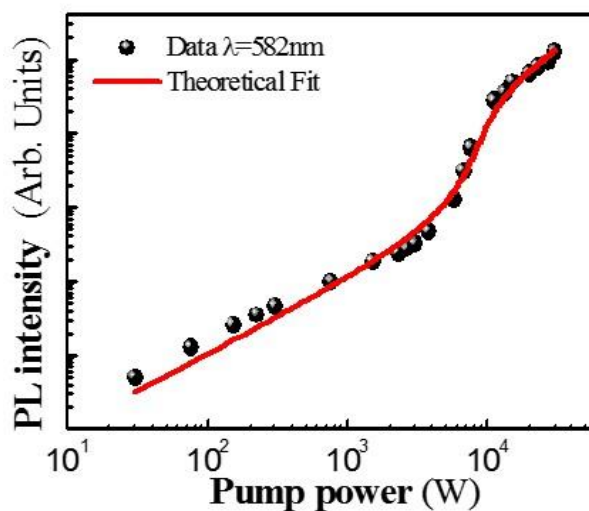
Figure 47. PL peak at 582 *nm*, at different pump power for the sample with the Ag MNPs: experimental data (black points) and simulation (red line).

4 Conclusions

In this Thesis we propose the integration of organic compounds (Perylenediimides derivatives) and metal nanoparticles into polymer waveguides to exploit their active and plasmonic properties for different photonic applications.

In this way, the following main works were performed:

- **Amplification of the spontaneous emission** from a PDI-PMMA nanocomposite was studied. For this purpose, a novel structure, which consisted of a thin (100 *nm*) PMMA-PDI film sandwiched between two passive PMMA claddings, was proposed. The high confinement of light in the nanocomposite layer results in an efficient excitation and generation of photoluminescence, and the absence of losses in the cladding guarantee the propagation of the pump beam along the whole length of the structure. The properly optimization of the geometrical parameters resulted in the amplification of the spontaneous emission (ASE) with a threshold as low as *0.9 μJ* and a linewidth of ASE as narrow as *2 nm*. The proposed device is a future alternative to implement on-chip optical amplifiers for visible light communications.

- A method to grow gold metal nanoparticles in situ within a commercial photoresist (Novolak) was thoroughly studied, and demonstrated an optimum control of their size with the initial concentration and growing time. This nanocomposite was patterned inside a PMMA waveguide in order to exploit the high scattering properties of the **MNPs to couple normal incident light into the PMMA film**. As a result, light coupling was experimentally demonstrated in a broad wavelength range (404-780

91

nm) with efficiencies as high as *1 %*. This coupling efficiency is of the same order of magnitude as the one obtained under end-fire coupling conditions. The proposed configuration could be an alternative to diffraction gratings for light coupling in integrated photonic platforms.

Finally, the active material (PMMA-PDI-1 composite) was properly combined with metal nanoparticles in order to exploit their interaction in the following way:

- The **emission of light of the PDI is significantly enhanced by a weak coupling with commercial silver nanoparticles**. For this purpose, the MNPs-PDI system is integrated inside a waveguide structure, in order to enhance the Purcell factor up to 10 due to the high confinement of light inside the structure. This approach can be applied to improve the efficiency of light emitting devices.

- Then a PMMA film highly doped with PDI was integrated with commercial silver nanoparticles in order to **demonstrate a random distributed feedback laser**. For this purpose, the high scattering of the MNPs produced the necessary random feedback for laser operation with a threshold of around *10 μJ*.

In these conditions, this Ph. D. Thesis will influence future research lines in the host (UMDO) group. For example, it would be very interesting to demonstrate random lasing into a waveguide configuration because the high confinement of light in this structure would improve the quality parameters. In the same way,

different cavity configurations could be also integrated in the PDI-PMMA amplifier to demonstrate lasing. Examples include gratings etched at the extremes of the waveguide or mirrors evaporated at its input/output facets. The work with metal nanoparticles can be also completed to perform more ambitious approaches. For instance, metal nanoparticles could be patterned in different configurations to guide light along the structures or even to provide a direct feedback of the light. In this way, the exciton-plasmon interaction could be exploited to improve the quality of an optical amplifier.

5 References

[1]   G. Lifante, *Integrated Photonics: Fundamentals*. 2003.

[2]   R. C. Alferness, H. Kogelnik, and T. H. Wood, "The evolution of optical systems: Optics everywhere," *Bell Labs Tech. J.*, vol. 5, no. 1, p. 188, 2000.

[3]   D. Dey and T. Goswami, "Optical biosensors: A revolution towards quantum nanoscale electronics device fabrication," *J. of Biomed. and Biotech.*, vol. 2011. p. 7, 2011.

[4]   M. Uddin and H. Chan, "Materials and process optimization in the reliable fabrication of polymer photonic devices," *J. Optoelectron. Adv.*, vol. 10, no. 1, p. 1, 2008.

[5]   U. Kreibig and M. Vollmer, *Optical Properties of Metal Clusters*. 1995.

[6]   C. Bohren and D. Huffman, *Absorption and Scattering of Light by Small Particles*, 2008.

[7]   H. Xu, J. Aizpurua, M. Käll, and P. Apell, "Electromagnetic contributions to single-molecule sensitivity in surface-enhanced Raman scattering," *Phys. Rev. E*, vol. 62, no. 3B, p. 4318, 2000.

[8]   F. Neubrech, T. Kolb, R. Lovrincic, G. Fahsold, A. Pucci, J. Aizpurua, T. W. Cornelius, M. E. Toimil-Molares, R. Neumann and S. Karim, "Resonances of individual metal nanowires in the infrared," Appl. Phys. Lett., vol. 89, no. 25, p. 253104, 2006.

[9]   S. Nie, "Probing Single Molecules and Single Nanoparticles by Surface-Enhanced Raman Scattering," *Sci.*, vol. 275, no. 5303, p. 1102, 1997.

[10]   A. Otto, I. Mrozek, H. Grabhorn, and W. Akemann, "Surface-enhanced raman scattering," *J. Phys. Condens. Matter*, vol. 604, no. 5, p. 1143, 1992.

[11] L. R. Hirsch, R. J. Stafford, J. A. Bankson, S. R. Sershen, B. Rivera, R. E. Price, J. D. Hazle, N. J. Halas and J. L. West, "Nanoshell-mediated near-infrared thermal therapy of tumors under magnetic resonance guidance," *Proc. Natl. Acad. Sci. U. S. A.*, vol. 100, no. 23, p. 13549, 2003.

[12] N. H. Weste and K. Eshraghian, *Principles of CMOS VLSI design*. 1985.

[13] H. A. Atwater, "The promise of plasmonics," *Sci. Am.*, vol. 296, no. 4, p. 56, 2007.

[14] S. Lal, S. Link, and N. J. Halas, "Nano-optics from sensing to waveguiding," *Nat. Photonics*, vol. 1, no. 11, p. 641, 2007.

[15] E. Ozbay, "Plasmonics: merging photonics and electronics at nanoscale dimensions.," *Sci.*, vol. 311, no. 5758, p. 189, 2006.

[16] J. D. B. Bradley and M. Pollnau, "Erbium-doped integrated waveguide amplifiers and lasers," *Laser Phot. Rev.*, vol. 5, no. 3, p. 368, 2011.

[17] N. Pelletier, B. Bèche, E. Gaviot, L. Camberlein, N. Grossard, F. Polet, and J. Zyss, "Single-Mode Rib Optical Waveguides on SOG / SU-8 Polymer and Integrated Mach – Zehnder for Designing Thermal Sensors," *IEEE Sensors*, vol. 6, no. 3, p. 565, 2006.

[18] L. Eldada and L. W. Shacklette, "Advances in polymer integrated optics," *IEEE J. Sel. Top. Quantum Electron.*, vol. 6, no. 1, p. 54, 2000.

[19] I. D. W. Samuel and G. a Turnbull, "Organic semiconductor lasers.," *Chem. Rev.*, vol. 107, no. 4, p. 1272, 2007.

[20] C. Grivas and M. Pollnau, "Organic solid-state integrated amplifiers and lasers," *Laser and Phot. Rev.*, vol. 6, no. 4. p. 419, 2012.

[21] S. Chénais and S. Forget, "Recent advances in solid state organic lasers," *Polym. Int.*, vol. 61, no. 3, p. 390, 2012.

[22] M. A. Reilly, C. Marinelli, C. N. Morgan, R. V. Penty, I. H. White, M.

Ramon, M. Ariu, R. Xia and D. D. C. Bradley, "Rib waveguide dye-doped polymer amplifier with up to 26 dB optical gain at 625 nm," *Appl. Phys. Lett.*, vol. 85, no. 22, p. 5137, 2004.

[23]   C. Dang, J. Lee, C. Breen, J. S. Steckel, S. Coe-Sullivan, and A. Nurmikko, "Red, green and blue lasing enabled by single-exciton gain in colloidal quantum dot films," *Nat. Nanotechnol.*, vol. 7, no. 5, p. 335, 2012.

[24]   L. Hu, H. Wu, L. Du, H. Ge, X. Chen, and N. Dai, "The effect of annealing and photoactivation on the optical transitions of band-band and surface trap states of colloidal quantum dots in PMMA.," *Nanotechnol.*, vol. 22, no. 12, p. 125202, 2011.

[25]   J. Q. Grim, S. Christodoulou, F. Di Stasio, R. Krahne, R. Cingolani, L. Manna, and I. Moreels, Iwan, "Continuous-wave biexciton lasing at room temperature using solution-processed quantum wells," *Nat. Nanotechnol.*, vol. 9, no. 11, p. 891, 2014.

[26]   G. Xing, N. Mathews, S. S. Lim, N. Yantara, X. Liu, D. Sabba, M. Gràtzel, S. Mhaisalkar and T. C. Sum, "Low-temperature solution-processed wavelength-tunable perovskites for lasing.," *Nat. Mater.*, vol. 13, no. 5, p. 476, 2014.

[27]   I. Suárez, "Active photonic devices based on colloidal semiconductor nanocrystals and organometallic halide perovskites," *Eur. Phys. J. Appl. Phys.*, vol. 75, no. 3, p. 30001, 2016.

[28]   I. Suárez, "Moduladores electroópticos integrados en LiNbO$_3$," Tesi doctoral, Univesidad Autonoma de Madrid, 2006.

[29]   K. K. Tung, W. H. Wong, and E. Y. B. Pun, "Polymeric optical waveguides using direct ultraviolet photolithography process," *Appl. Phys. A Mater. Sci. Process.*, vol. 80, no. 3, p. 621, 2005.

[30] C. Vieu, F. Carcenac, A. Pepin, Y. Chen, M. Mejias, A. Lebib, L. Manin-Ferlazzo, L. Couraud and H. Launois, "Electron beam lithography - Resolution limits and applications," *Appl. Surf. Sci.*, vol. 164, no. 1, p. 111, 2000.

[31] R. Abargues, K. Abderrafi, E. Pedrueza, R. Gradess, J. Marquès-Hueso, J. L. Valdès and J. Martìnez-Pastor, Juan, "Optical properties of different polymer thin films containing in situ synthesized Ag and Au nanoparticles," *New J. Chem.*, vol. 33, no. 8, p. 1720, 2009.

[32] F. Hussain, M. Hojjati, M. Okamoto, and R. E. Gorga, "Review article: Polymer-matrix Nanocomposites, Processing, Manufacturing, and Application: An Overview," *J. Compos. Mater.*, vol. 40, no. 17, p. 1511, Jan. 2006.

[33] G. Schmid, *Nanoparticles: From theory to applications*. 2011.

[34] I. Suárez, H. Gordillo, R. Abargues, S. Albert, and J. Martínez-Pastor, "Photoluminescence waveguiding in CdSe and CdTe QDs–PMMA nanocomposite films," *Nanotechnol.*, vol. 22, no. 43, p. 435202, 2011.

[35] T. M. Figueira-Duarte and K. Mullen, "Pyrene-based materials for organic electronics," *Chem. Rev.*, vol. 111, no. 11, p. 7260, 2011.

[36] R. Weitzenböck, "Eine Synthese des Pyrens," *Monatshefte fur Chemie/Chemical Mon.*, vol. 34, no. 1, p. 193, 1913.

[37] P. M. Kazmaier and R. Hoffmann, "A theoretical study of crystallochromy quantum interference effects in the spectra of Perylene pigments," *J. Am. Chem. Soc.*, vol. 116, no. 21, p. 9684, 1994.

[38] F. Würthner, "Perylene bisimide dyes as versatile building blocks for functional supramolecular architectures," *Chem. Commun.*, no. 14, p. 1564, 2004.

[39] J. M. Serin, D. W. Brousmiche, and J. M. J. Fréchet, "Cascade energy transfer in a conformationally mobile multichromophoric dendrimer," *Chem Commun*, no. 22, p. 2605, 2002.

[40] R. Gronheid, J. Hofkens, F. Kòhn, T. Weil, E. Reuther, K. Müllen and F. C. De Schryver, "Intramolecular Förster energy transfer in a dendritic system at the single molecule level," *J. Am. Chem. Soc.*, vol. 124, no. 11, p. 2418, 2002.

[41] Z. An, J. Yu, S. C. Jones, S. Barlow, S. Yoo, B. Domercq, P. Prins, L. D. A. Siebbeles, B. Kippelen and S. R. Marder, "High electron mobility in room-temperature discotic liquid-crystalline perylene diimides," *Adv. Mater.*, vol. 17, no. 21, p. 2580, 2005.

[42] B. A. Jones, A. Facchetti, M. R. Wasielewski, and T. J. Marks, "Tuning orbital energetics in arylene diimide semiconductors. Materials design for ambient stability of n-type charge transport," *J. Am. Chem. Soc.*, vol. 129, no. 49, p. 15259, 2007.

[43] M. Sadrai and G. R. Bird, "A new laser dye with potential for high stability and a broad band of lasing action: perylene-3, 4, 9, 10-tetracarboxylic acid-bis-N, N'(2', 6' xylidyl) diimide," *Opt. Commun.*, vol. 51, no. 1, p. 62, 1984.

[44] G. Seybold and G. Wagenblast, "New perylene and violanthrone dyestuffs for fluorescent collectors," *Dye. Pigment.*, vol. 11, no. 4, p. 303, 1989.

[45] T. Weil, U. M. Wiesler, A. Herrmann, R. Bauer, J. Hofkens, F. C. De Schryver and K. Müllen, "Polyphenylene dendrimers with different fluorescent chromophores asymmetrically distributed at the periphery," *J. Am. Chem. Soc.*, vol. 123, no. 33, p. 8101, 2001.

[46] M. J. Ahrens, M. J. Fuller, and M. R. Wasielewski, "Cyanated perylene-

3,4-dicarboximides and perylene-3,4:9,10-bis(dicarboximide): Facile chromophoric oxidants for organic photonics and electronics," *Chem. Mater.*, vol. 15, no. 14, p. 2684, 2003.

[47] F. Fernández-Lázaro, N. Zink-Lorre, and Á. Sastre-Santos, "Perylenediimides as non-fullerene acceptors in bulk-heterojunction solar cells (BHJSCs)," *J. Mater. Chem. A*, vol. 4, no. 24, p. 9336, 2016.

[48] H. Usta, A. Facchetti, and T. J. Marks, "N-channel semiconductor materials design for organic complementary circuits," *Acc. Chem. Res.*, vol. 44, no. 7, p. 501, 2011.

[49] M. Morales-Vidal, P. G. Boj, J. A. Quintana, J. M. Villalvilla, A. Retolaza, S. Merino and M. A. Dìaz-Garcìa, "Distributed feedback lasers based on perylenediimide dyes for label-free refractive index sensing," *Sensors Actuators B Chem.*, vol. 220, p. 1368, 2015.

[50] M. G. Ramirez, S. Pla, P. G. Boj, J. M. Villalvilla, J. A. Quintana, M. A. Dìaz-Garcìa, F. Fernàndez-Làzaro and À. Sastre-Santos, "1,7-Bay-substituted perylenediimide derivative with outstanding laser performance," *Adv. Opt. Mater.*, vol. 1, no. 12, p. 933, 2013.

[51] H. L. Lord, W. Zhan, and J. Pawliszyn, *Plasmonics: Fundamentals and Applications*. 2007.

[52] F. J. Beck, S. Mokkapati, and K. R. Catchpole, "Light trapping with plasmonic particles: beyond the dipole model," *Opt. Express*, vol. 19, no. 25, p. 25230, 2011.

[53] S. A. Maier, P. G. Kik, H. A. Atwater, S. Meltzer, E. Harel, B. E. Koel and A. A. G. Requicha, "Local detection of electromagnetic energy transport below the diffraction limit in metal nanoparticle plasmon waveguides," *Nat. Mater.*, vol. 2, no. 4, p. 229, 2003.

[54] T. P. H. Sidiropoulos, M. P. Nielsen, T. R. Roschuk, A. V Zayats, S. A. Maier, and R. F. Oulton, "Compact Optical Antenna Coupler for Silicon Photonics Characterized by Third-Harmonic Generation," *ACS Phot.*, vol. 1, no. 10, p. 912, 2014.

[55] A. Apuzzo, M. Fèvrier, R. Salas-Montiel, A. Bruyant, A. Chelnokov, G. Lèrondel, B. Dagens and S. Blaize, "Observation of near-field dipolar interactions involved in a metal nanoparticle chain waveguide," *Nano Lett.*, vol. 13, no. 3, p. 1000, 2013.

[56] X. Shi, Y. Wang, Z. Wang, Y. Sun, D. Liu, Y. Zhang, Q. Li and J. Shi, "High performance plasmonic random laser based on nanogaps in bimetallic porous nanowires," *Appl. Phys. Lett.*, vol. 103, no. 2, p. 23504, 2013.

[57] C. T. Dominguez, R. L. Maltez, R. M. S. dos Reis, L. S. a. de Melo, C. B. de Araújo, and A. S. L. Gomes, "Dependence of random laser emission on silver nanoparticle density in PMMA films containing rhodamine 6G," *J. Opt. Soc. Am. B*, vol. 28, no. 5, p. 1118, 2011.

[58] Z. Wang, X. Shi, S. Wei, Y. Sun, Y. Wang, J. Zhou, J. Shi and D. Liu, "Two-threshold silver nanowire-based random laser with different dye concentrations," *Laser Phys. Lett.*, vol. 11, no. 9, p. 95002, 2014.

[59] Z. Hu, Y. Liang, K. Xie, P. Gao, D. Zhang, H. Jiang, F. Shi, L. Yin, J. Gao, H. Ming and Q. Zhang., "Gold nanoparticle-based plasmonic random fiber laser," *J. Opt.*, vol. 17, no. 3, p. 35001, 2015.

[60] S. Link and M. A. El-Sayed, "Shape and size dependence of radiative, non-radiative and photothermal properties of gold nanocrystals," *Int. Rev. Phys. Chem.*, vol. 19, no. 3, p. 409, 2000.

[61] P. K. Jain, K. S. Lee, I. H. El-Sayed, and M. A. El-Sayed, "Calculated

absorption and scattering properties of gold nanoparticles of different size, shape, and composition: Applications in biological imaging and biomedicine," *J. Phys. Chem. B*, vol. 110, no. 14, p. 7238, 2006.

[62] S. Underwood and P. Mulvaney, "Effect of the Solution Refractive Index on the Color of Gold Colloids," *Langmuir*, vol. 10, no. 3, p. 3427, 1994.

[63] S. K. Ghosh, S. Nath, S. Kundu, K. Esumi, and T. Pal, "Solvent and Ligand Effects on the Localized Surface Plasmon Resonance (LSPR) of Gold colloids," *J. Phys. Chem B*, vol. 108, no. 37, p. 13963, 2004.

[64] K. H. Su, Q. H. Wei, X. Zhang, J. Mock, D. R. Smith, and S. Schultz, "Interparticle Coupling Effects on Plasmon Resonances of Nanogold Particles," *Nano Lett.*, vol. 3, no. 8, p. 1087, 2003.

[65] N. L. Rosi and C. A. Mirkin, "Nanostructures in biodiagnostics," *Chem. Rev.*, vol. 105, no. 4, p. 1547, 2005.

[66] C. A. Mirkin, R. L. Letsinger, R. C. Mucic, and J. J. Storhoff, "A DNA-based method for rationally assembling nanoparticles into macroscopic materials," *Nature*, vol. 382, no. 6592, p. 607, 1996.

[67] C. K. Chen, A. R. B. De Castro, and Y. R. Shen, "Surface-enhanced second-harmonic generation and Raman scattering," *Phys. Rev. B*, vol. 27, no. 4, p. 1965, 1983.

[68] K. Kneipp, Y. Wang, H. Kneipp, L. T. Perelman, and I. Itzkan, "Single molecule detection using surface-enhanced Raman scattering (SERS)," *Phys. Rev.,* vol. 78, no. 9, p. 1667, 1997.

[69] I. H. El-Sayed, X. Huang, and Mostafa A. El-Sayed, "Surface plasmon resonance scattering and absorption of anti-EGFR antibody conjugated gold nanoparticles in cancer diagnostics: applications in oral cancer," *Nano Lett.*, vol. 5, no. 5, p. 829, 2005.

[70] K. Sokolov, M. Follen, J. Aaron, I. Pavlova, A. Malpica, R. Lotan and R. Richards-Kortum, "Real-time vital optical imaging of precancer using anti-epidermal growth factor receptor antibodies conjugated to gold nanoparticles," *Cancer Res.*, vol. 63, no. 9, p. 1999, 2003.

[71] V. P. Zharov, E. N. Galitovskaya, C. Johnson, and T. Kelly, "Synergistic enhancement of selective nanophotothermolysis with gold nanoclusters: Potential for cancer therapy," *Lasers Surg. Med.*, vol. 37, no. 3, p. 219, 2005.

[72] V. P. Zharov, J.-W. Kim, D. T. Curiel, and M. Everts, "Self-assembling nanoclusters in living systems: application for integrated photothermal nanodiagnostics and nanotherapy," *Nanomed.*, vol. 1, no. 4, p. 326, 2005.

[73] E. E. Connor, J. Mwamuka, A. Gole, C. J. Murphy, and M. D. Wyatt, "Gold nanoparticles are taken up by human cells but do not cause acute cytoxicity," *Small*, vol. 1, no. 3, p. 325, 2005.

[74] C. Burda, X. Chen, R. Narayanan, and M. A. El-Sayed, "Chemistry and properties of nanocrystals of different shapes," *Chem. Rev.*, vol. 105, no. 4, p. 1025, 2005.

[75] E. Katz and I. Willner, "Integrated nanoparticle--biomolecule hybrid systems: synthesis, properties, and applications," *Angew. Chemie Int. Ed.*, vol. 43, no. 45, p. 6042, 2004.

[76] M. Signoretto, N. Zink-Lorre, I. Suàrez, E. Font-Sanchis, A. Sastre-Santos, V. S. Chirvony, F. Fernàndez-Làzaro and J. P. Martìnez-Pastor, "Efficient Optical Amplification in a Sandwich-Type Active-Passive Polymer Waveguide Containing Perylenediimides," *ACS Phot.*, vol. 4, no. 1, p. 114, 2017.

[77] M. Signoretto, I. Suárez, V. S. Chirvony, R. Abargues, P. J. Rodríguez-

Cantó, and J. Martínez-Pastor, "Polymer waveguide couplers based on metal nanoparticle–polymer nanocomposites," *Nanotechnol.*, vol. 26, no. 47, p. 475201, 2015.

[78] M. Signoretto, N. Zink-Lorre, I. Suárez, E. Font-Sanchis, V. Chirvony, Á. Sastre-Santos, F. Fernández-Lázaro and J. P. Martínez-Pastor, "Purcell-enhancement of the radiative PL decay in perylenediimides by coupling with silver nanoparticles into waveguide modes," *Appl. Phys. Lett.*, vol. 111, no. September, p. 081102, 2017.

[79] C. J. D. Catto and K. C. A. Smith, "Resolution limits in the surface scanning electron microscope," *J. Microsc.*, vol. 98, no. 3, p. 417, 1973.

[80] A. Costela, O. García, L. Cerdán, I. García-Moreno, and R. Sastre, "Amplified spontaneous emission and optical gain measurements from pyrromethene 567-doped polymer waveguides and quasi-waveguides," *Opt. Express*, vol. 16, no. 10, p. 7023, 2008.

[81] D. O. Kundys, P. Murzyn, J. P. R. Wells, A. I. Tartakovskii, M. S. Skolnick, L. S. Dang, E. V. Lutsenko, N. P. Tarasuk, O. G. Lyublinskaya, A. A. Toropov, and S. V. Ivanov., "The dynamics of amplified spontaneous emission in CdSe/ZnSe quantum dots," *J. Appl. Phys.*, vol. 100, no. 12, p. 123510, 2006.

[82] M. C. Gather, K. Meerholz, N. Danz, and K. Leosson, "Net optical gain in a plasmonic waveguide embedded in a fluorescent polymer," *Nat. Photonics*, vol. 4, no. 7, p. 457, 2010.

[83] L. Dal Negro, P. Bettotti, M. Cazzanelli, D. Pacifici, and L. Pavesi, "Applicability conditions and experimental analysis of the variable stripe length method for gain measurements," *Opt. Commun.*, vol. 229, no. 6, p. 337, 2004.

[84]   N. Zink-Lorre, E. Font-Sanchis, Á. Sastre-Santos, and F. Fernández-Lázaro, "Easy and mild fluoride-mediated direct mono- and dialkoxylation of perylenediimides," *Dye. Pigment.*, vol. 127, no. April, p. 9, 2016.

[85]   L. Cerdàn, A. Costela, G. Duràn-Sampedro, I. Garcìa-Moreno, M. Calle, M. Juan-y-Seva, J. de Abajo and G. A. Turnbull, "New perylene-doped polymeric thin films for efficient and long-lasting lasers," *J. Mater. Chem.*, vol. 22, no. 18, p. 8938, 2012.

[86]   M. G. Ramirez, M. Morales-Vidal, V. Navarro-Fuster, P. G. Boj, J. A. Quintana, J. M. Villalvilla, A. Retolaza, S. Merino and M. A. Dìaz-Garcìa, "Improved performance of perylenediimide-based lasers," *J. Mater. Chem. C*, vol. 1, no. 6, p. 1182, 2013.

[87]   E. M. Calzado, J. M. Villalvilla, P. G. Boj, J. A. Quintana, R. Gomez, J. L. Segura and M. A. Dìaz-Garcìa, "Effect of structural modifications in the spectral and laser properties of perylenediimide derivatives," *J. Phys. Chem. C*, vol. 111, no. 36, p. 13595, 2007.

[88]   E. M. Calzado, J. M. Villalvilla, P. G. and Boj, J. A. Quintana, R. Gòmez, J. L. Segura and M. A. Dìaz-Garcìa, "Amplified spontaneous emission in polymer films doped with a perylenediimide derivative," *Appl. Opt.*, vol. 46, no. 18, p. 3836, 2007.

[89]   E. M. Calzado, M. G. Ramírez, P. G. Boj, and M. A. Dìaz-García, "Thickness dependence of amplified spontaneous emission in low-absorbing organic waveguides," *Appl. Opt.*, vol. 51, no. 16, p. 3287, 2012.

[90]   I. Suárez, A. Larrue, P. J. Rodrìguez-Cantò, G. Almuneau, R. Abargues, V. S. Chirvony and J. P. Martìnez-Pastor, "Efficient excitation of photoluminescence in a two-dimensional waveguide consisting of a quantum dot-polymer sandwich-type structure," *Opt. Lett.*, vol. 39, no. 16,

p. 4962, 2014.

[91] V. Myroshnychenko, J. Rodrìguez-Fernàndez, I. Pastoriza-Santos, A. M. Funston, C. Novo, P. Mulvaney, L. M. Liz-Marzàn and F. J. G. de Abajo, "Modelling the optical response of gold nanoparticles," *Chem. Soc. Rev.*, vol. 37, no. 9, p. 1792, 2008.

[92] R. Abargues, M. L. Martinez-Marco, P. J. Rodriguez-Canto, J. Marques-Hueso, and J. P. Martinez-Pastor, "Metal-polymer nanocomposite resist: a step towards in-situ nanopatterns metallization," *Proc. SPIE*, vol. 8682, no. March, p. 86820X, 2013.

[93] X. Huang and M. A. El-Sayed, "Gold nanoparticles: Optical properties and implementations in cancer diagnosis and photothermal therapy," *J. Adv. Res.*, vol. 1, no. 1, p. 13, 2010.

[94] P. Mulvaney, "Not All That's Gold Does Glitter," *MRS Bull.*, vol. 26, no. 12, p. 1009, 2001.

[95] H. Chen, X. Kou, Z. Yang, W. Ni, and J. Wang, "Shape- and size-dependent refractive index sensitivity of gold nanoparticles," *Langmuir*, vol. 24, no. 10, p. 5233, 2008.

[96] B. Salski and M. Celuch, "On the equivalence between the maxwell-garnett mixing rule and the debye relaxation formula," *IEEE Trans. Microw. Theory Tech.*, vol. 60, no. 8, p. 2352, 2012.

[97] E. Pedrueza, J. L. Valdès, V. Chirvony, R. Abargues, J. Hernàndez-Saz, M. Herrera, S. I. Molina and J. P. Martìnez-Pastor, "Novel method of preparation of gold-nanoparticle-doped TiO_2 and SiO_2 plasmonic thin films: Optical characterization and comparison with Maxwell-Garnett modeling," *Adv. Funct. Mater.*, vol. 21, no. 18, p. 3502, 2011.

[98] B. Scaffardi and J. O. Tocho, "Size dependence of refractive index of gold

nanoparticles," *Nanotechnol.*, vol. 17, no. 5, p. 1309, 2006.

[99] H. Inouye, K. Tanaka, I. Tanahashi, and K. Hirao, "Ultrafast dynamics of nonequilibrium electrons in a gold nanoparticle system," *Phys. Rev. B*, vol. 57, no. 18, p. 11334, 1998.

[100] P. B. Johnson and R. W. Christry, "Optical Constants of the Noble Metals," *Phys. Rev. B*, vol. 6, no. 12, p. 4370, 1972.

[101] C. Noguez, "Surface plasmons on metal nanoparticles: The influence of shape and physical environment," *J. Phys. Chem. C*, vol. 111, no. 10, p. 3606, 2007.

[102] R. W. Christy, P.B. Johnson, "Optical Constants of the Noble Metals," *Phys. Rev. B*, vol. 6, no. 1970, p. 4370, 1972.

[103] P. Anger, P. Bharadwaj, and L. Novotny, "Enhancement and quenching of single-molecule fluorescence," *Phys. Rev. Lett.*, vol. 96, no. 11, p. 3, 2006.

[104] K. Q. Le, "Nanoplasmonic Enhancement of Molecular Fluorescence: Theory and Numerical Modeling," *Plasmonics*, vol. 10, no. 2, p. 475, 2015.

[105] T. V. Shahbazyan, "Theory of plasmon-enhanced metal photoluminescence," *Nano Lett.*, vol. 13, no. 1, p. 194, 2013.

[106] D. V. Guzatov, S. V. Vaschenko, V. V. Stankevich, A. Y. Lunevich, Y. F. Glukhov, and S. V. Gaponenko, "Plasmonic enhancement of molecular fluorescence near silver nanoparticles: Theory, modeling, and experiment," *J. Phys. Chem. C*, vol. 116, no. 19, p. 10723, 2012.

[107] F. Tam, P. G. Goodrich, R. B. Johnson, and J. N. Halas, "Plasmonic Enhancement of Molecular Fluorescence," *Nano Lett.*, vol. 7, no. 2, p. 496, 2007.

[108] G. M. Akselrod, C. Argyropoulos, T. B. Hoang, C. Ciracì, C. Fang, J. Huang, D. R. Smith and M. H. Mikkelsen, "Probing the mechanisms of

large Purcell enhancement in plasmonic nanoantennas," *Nat. Photonics*, vol. 8, no. 11, p. 835, 2014.

[109] M. Khajavikhan, A. Simic, M. Katz, J. H. Lee, B. Slutsky, A. Mizrahi, V. Lomakin and Y. Fainman, "Thresholdless nanoscale coaxial lasers," *Nature*, vol. 482, no. 7384, p. 204, 2012.

[110] J. Canet-Ferrer, I. Prieto, G. Munoz-Matutano, L. J. Martınez, L. E. Munoz-Camuniez, J. M. Llorens, D. Fuster, B. Alen, Y. Gonzalez, L. Gonzalez, P. A. Postigo and J. P. Martınez-Pastor, "Excitation power dependence of the Purcell effect in photonic crystal microcavity lasers with quantum wires," *Appl. Phys. Lett.*, vol. 102, no. 20, p. 201105, 2013.

[111] K. K. Sharma, *Optics : principles and applications*. 2006.

[112] T. Zhai, X. Zhang, Z. Pang, X. Su, H. Liu, S Feng and L. Wang, "Random laser based on waveguided plasmonic gain channels," *Nano Lett.*, vol. 11, no. 10, p. 4295, 2011.

[113] L. A. Coldren, S. W. Corzine, and M. L. Mašanović, *Diode lasers and photonic integrated circuits*. 2012.

[114] I. Prieto, J. M. Llorens, L. E. Munoz-Camùnez, A. G. Taboada, J. Canet-Ferrer, J. M. Ripalda, C. Robles, G. Muñoz-Matutano, J. P. Martìnez-Pastor and P. A. Postigo, "Near thresholdless laser operation at room temperature," *Optic.*, vol. 2, no. 1, p. 66, 2015.

[115] H. Cao, J. Xu, S.-H. Chang, and S. T. Ho, "Transition from amplified spontaneous emission to laser action in strongly scattering media," *Phys. Rev. E*, vol. 61, no. 2, p. 1985, 2000.

[116] D. S. Wiersma, "The physics and applications of random lasers," *Nat. Phys.*, vol. 4, no. 5, p. 359, 2008.

[117] S. A. Javro and S. M. Kang, "Transforming Tucker's linearized laser rate

equations to a form that has a single solution regime," *J. Lightwave Technol.*, vol. 13, no. 9, p. 1899, 1995.

[118] L. V. T. Nguyen, A. J. Lowery, P. C. R. Gurney, and D. Novak, "A time-domain model for high-speed quantum-well lasers including carrier transport effects," *IEEE J. Select. Topics Quantum Electron.*, vol. 1, no. 2, p. 494, 1995

6   Publications annex

Efficient Optical Amplification in a Sandwich-Type Active-Passive Polymer Waveguide Containing Perylenediimides

Mattia Signoretto,[†] Nathalie Zink-Lorre,[‡] Isaac Suárez,*[,†] Enrique Font-Sanchis,[‡] Ángela Sastre-Santos,[‡] Vladimir S. Chirvony,[†] Fernando Fernández-Lázaro,*[,‡] and Juan P. Martínez-Pastor[†]

[†]UMDO, Instituto de Ciencia de los Materiales, Universidad de Valencia, Valencia 46071, Spain
[‡]Área de Química Orgánica, Instituto de Bioingeniería, Universidad Miguel Hernández de Elche, Avda. de la Universidad s/n, Elche 03202, Spain

S *Supporting Information*

ABSTRACT: Polymer waveguides doped with luminescent materials serve as a suitable flexible platform for active elements (lasers and amplifiers) in on-chip optical circuits. However, at present, the best parameters (lowest thresholds) achieved with these devices are obtained with the use of the stripe excitation technique in the framework of which external illumination of an active material along the whole length of the waveguide is realized that is not convenient for the waveguide on-chip integration and requires high peak energies due to the large excitation area. In the present work, an elegant method is proposed to overcome this obstacle and provide efficient active material pumping along the whole waveguide length with use of on-chip integration compatible edge-type excitation light injection. This novel type of planar active-passive polymer waveguides includes a thin (50−100 nm) active layer of poly(methyl methacrylate) (PMMA), which is heavily doped with highly luminescent perylenediimide (PDI) molecules, sandwiched between two cladding (passive) PMMA layers. This structure efficiently exploits the excellent light-emitting properties of PDIs with a confinement of both the excitation beam and the photoluminescence in the active PMMA−PDI film. In this way, the absence of losses in the PMMA claddings guarantees the propagation of the pump beam along the whole length of the structure (≈1 mm) in order to provide the required excitation to obtain stimulated emission. Geometrical parameters are optimized to demonstrate the amplified spontaneous emission with a threshold as low as 0.9 μJ and a line width as narrow as 2 nm.

KEYWORDS: *perylenediimide, ASE, amplifier, waveguide, PMMA*
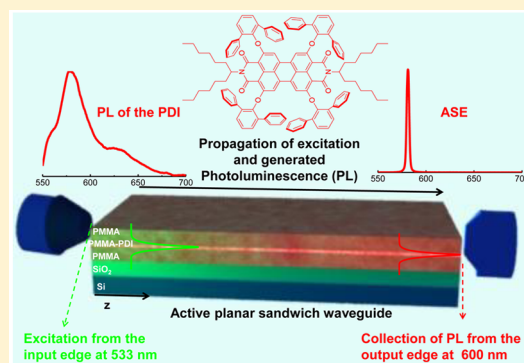
The incorporation of active materials processed in solution (luminescent organic molecules,[1−3] colloidal quantum dots,[4] colloidal quantum wells (nanoplateletes),[5] organic−inorganic semiconducting perovskites,[6] etc.) into optical waveguides provides a suitable platform for on-chip integration of amplifiers and lasers and an efficient geometry to inject/extract light into/from the waveguides. The most common approach in this way is to develop a planar film of a high enough concentration of the active material to overcome the stimulated emission threshold. The main problem of application of this geometry in integrated optical circuits is the method of pumping the active material. Indeed, the method of excitation usually consists of the stripe excitation technique,[7,8] in the framework of which an excitation beam has the shape of a strip on the planar waveguide surface and allows a uniform illumination of an active material along the whole length of the waveguide. However, this pumping geometry is not convenient for the waveguide on-chip integration (the excitation and emission beams propagate orthogonally), and besides, such pumping conditions usually require high peak energies to reach the amplified spontaneous emission (ASE) threshold due to the large excitation area

(∼100 μm × 1 mm).[7,8] The development of a full compact device in which the pump beam is coupled inside and propagates along the waveguide structure,[9,10] in analogy to the erbium-doped optic fiber amplifiers, usually cannot be realized because the pump beam propagation length is usually restricted to a few microns due to the strong absorption efficiency of active compounds embedded into a waveguide.[11] Here we propose an elegant strategy to overcome this problem with the use of a suitable waveguide design based on the combination of active layers with passive polymer films.[12,13] These structures allow a long distance propagation of the laser excitation beam together with an optimum generation of photoluminescence (PL). In addition, the technological feasibilities of polymers enable the deposition of the composite on several kinds of substrates or a posterior patterning by ultraviolet or e-beam techniques.[13]

Our active material consists of perylenediimides (PDIs).[14] These organic compounds represent an outstanding choice

because they exhibit not only good emission properties and wavelength tunability, but also good thermal and optical stabilities and high electron mobility.[15] In addition, optical and electronic properties of PDIs can be tailored by introducing the adequate substituents,[14,15] resulting in a broad range of applications, such as solar cells,[16] organic transistors,[17] optical sensors,[18] or solid state lasers.[19−22] For this purpose, the strategies to incorporate the material into a (solid state) device include assembling the compounds in a J-aggregated structure[19] or incorporating the PDIs in a polymer matrix, poly(methyl methacrylate) (PMMA)[20,21] or polystyrene.[22] The former strategy demonstrates hexagonal cavities with laser emission but requires a complicated design and technology to inject and extract light.[23] Incorporation of PDIs in polymers waveguides would provide a suitable platform of integration, but up to now, the studies have been limited to high doped thick films requiring surface excitation.[20−22]

Our waveguide consists of a thin (50−100 nm) PMMA layer doped with highly luminescent organic PDIs sandwiched between two PMMA thin layers. The low losses in the claddings allowed the propagation of the excitation beam along lengths longer than 1 mm, providing a high generation of PL with small pump powers. As a result, we obtain an ASE threshold as low as 0.9 μJ with a line width at half-maximum as narrow as 2 nm working at room temperature and ambient operation by using a novel PDI with bulky substituents in the ortho positions. To the best of our knowledge, this is the narrowest line width obtained up to now with PDI compounds without the aid of an optical resonator.[19−22] In addition, the proposed geometry has improved the stability of the emitting material up to 10^5 laser shoots, a 100-fold enhancement compared to previous reports on PDI composites.[14−16] Indeed, the optical pumping beam was produced by means of a nanosecond Q-switched pulsed laser at a moderated repetition rate of 100 Hz, a further improvement as compared to previous works using very low repetition rates (1−20 Hz) to reach stimulated emission in organic compounds.[24] These results pave the road for developing the next generation of low threshold active photonic devices based on organic materials.[25] Potential applications of optical sources based on organic compounds include sensors[26] or visible light communications, an emerging field for short-distance communications based on plastic optical fibers.[27]

■ SYNTHESIS AND FABRICATION OF THE COMPOSITE

The chemical structures of the two different PDIs studied in the present work are illustrated in Figure 1. PDI-1 presents four diphenylphenoxy substituents in the 2, 5, 8, and 11 positions, so-called ortho positions, and PDI-2 does not present any substituent either in the ortho or bay positions. PDI-1 has been synthesized for the first time, by using the methodology previously described by our group,[28] from 2,5,8,11-tetrabromoperylene-3,4:9,10-tetracarboxydiimide in the presence of 2,6-diphenylphenol, CsF, and 18-crown-6 (Scheme 1; see SI for the synthetic methodology and characterization). PDI-2 was prepared following the procedure previously described in the literature.[20]

Once the PDI compounds are properly prepared, PMMA composites were fabricated by dispersing the organic compound into the polymer with a concentration of 5% wt by mixing toluene solutions of PDI and PMMA (see
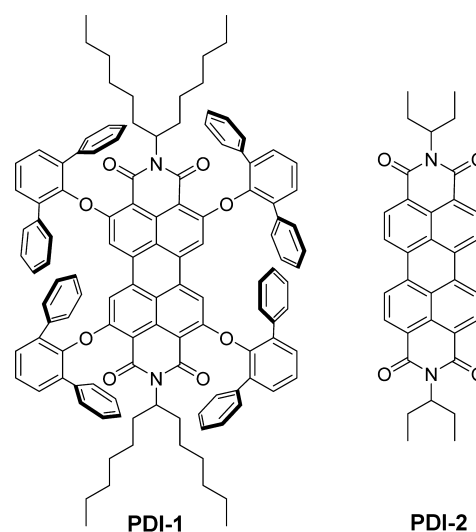

Figure 1. Chemical structure of the PDIs used in the present study.

Experimental Methods). The main photophysical properties of the PDIs used in this study are summarized in Table 1.

The absorption and PL spectra of PDI-1 and PDI-2 in toluene solution show the characteristic vibronic structure of PDIs[20−22] (see Figure 2, solid blue and red lines, respectively). The absorption spectrum of PDI-1 (10^{-5} M, solid blue line in Figure 2a) exhibits four peaks at 535, 498, 464, and 421 nm, corresponding to the 0−0, 0−1, 0−2, and 0−3 transitions, while PL (solid red line in Figure 1a) shows close to the mirror-reflection spectrum with peaks at 545, 590, and 641 nm (see section S2 in the Supporting Information for the Gaussian deconvolution of the PL spectrum), thus, indicating that PDI-1 is in a nonaggregated form. PDI-2 presents three absorption peaks at 457, 488, and 525 nm (1×10^{-5} M, solid blue line in Figure 2b), while the PL transitions are red-shifted at 542, 578, and 612 nm. Therefore, both compounds present similar absorption and PL spectra under low concentrated solutions. In addition, both PDI solutions exhibit similar recombination times (5.6−5.9 ns) with no influence on excitation fluence (0.3−30 μJ).

On the other contrary, the choice of the substituents plays an important role in the aggregation of PDIs in the polymer dispersions. In the PMMA−PDI-1 composite, the substituents do not alter the optical properties of the compound.[28] Indeed, although the absorption spectra experience a 10 nm blue shift (see blue dashed line in Figure 2a), its shape is not significantly modified, indicating the absence of aggregation in the film. In addition, the broader PL spectrum (see red dashed line in Figure 3a) shows the activation of new vibrational modes in the solid-state composite (see Figure S6b of the Supporting Information). However, the absorption and PL transitions in the PMMA−PDI-2 film (see blue and red dashed lines in Figure 2b) demonstrate different behaviors. Although both absorption and PL spectra does not show any shift when compared to the toluene solution, they are clearly broader, with an increase in the intensity of the 0−1 transitions. This is due to the fact that the absence of substituents in these derivates could lead to the formation of H-aggregates through $\pi-\pi$ stacking when a high concentration of PDI is incorporated in the film.[14,29]
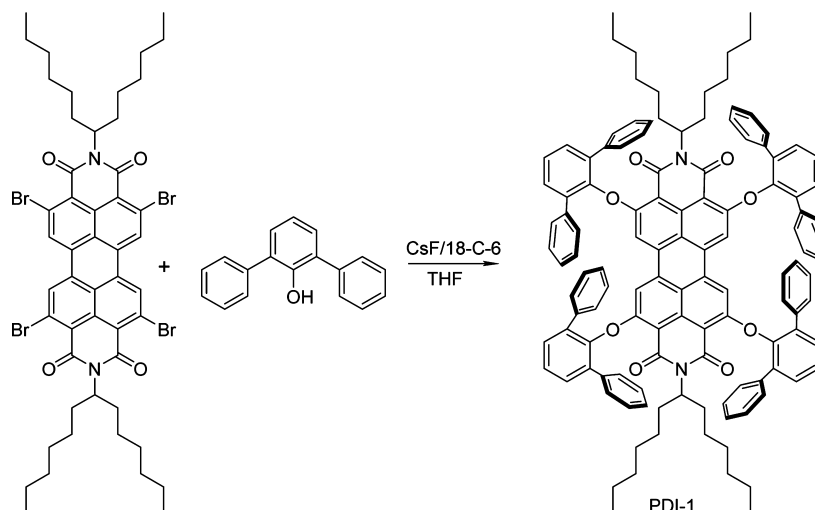
Scheme 1. Synthesis of PDI-1

Table 1. Photophysical Properties of the PDI Compounds Used in This Work

	solution (toluene)			
PDI	λ_{abs} (nm)	λ_{PL} (nm)	τ (ns)	QY (%)
PDI-1	464	546	5.6	95
	498	590		
	535	642		
PDI-2	457	542	5.9	92
	488	578		
	525	622		

■ RESULTS AND DISCUSSION

Design of the Waveguide. A thin PMMA–PDI film (50–200 nm) sandwiched between two PMMA layers (each one about 650 nm of thickness) has been deposited by spin-coating on a SiO_2/Si substrate (2 μm of SiO_2), as it is schematically illustrated in Figure 3a. Such a waveguide structure demonstrated an optimum generation of PL when it was previously applied to a PMMA composite film containing colloidal QDs as active medium.[13] The absence of losses in the claddings allows the propagation of the pump beam coupled at the input face of the structure, and the high confinement of the electric field at the fundamental optical mode within the active layer (see red solid line in Figure 3b) improves the generation

of PL measured at the output edge of the waveguide (see Figure 3a). Therefore, the structure proposed here allows an efficient excitation of the highly concentrated PMMA–PDI (5%) composite along the whole length of the waveguide (1–3 mm). At this doping concentration, the composite layer can provide a maximum gain as high as 2000 cm^{-1}, as estimated for the excitation wavelength at 533 nm, being the emission cross section $\approx 10^{-16}$ cm^2 and the concentration of PDI per unit volume $\approx 2 \times 10^{-19}$ cm^{-3}.[30] Moreover, the high concentration of the PMMA–PDI composite layer sandwiched by PMMA claddings not only enhances the generation of PL, but also improves the excitation of the PDI molecules by a local increase of the refractive index by 8% (see section S3 in Supporting Information). Under these conditions, the structure presents two propagating modes in each polarization at 533 (pump beam) and 580 nm (the wavelength of the 0–1 transition), as it has been deduced with a transfer matrix algorithm.[31] The fundamental TE_0 mode (similar distributions can be found for TM) is highly confined in the active PMMA–PDI layer (solid red line in Figure 3b) and the second mode, TE_1 (dashed red line in Figure 3b), is close to the cutoff and is highly delocalized in the SiO_2 region. As a consequence, the active material is efficiently pumped (at 533 nm) by the TE_0 mode, while the TE_1 reduces the losses of the excitation beam down to 6.3 cm^{-1} (169 cm^{-1} for the TE_0 mode), as estimated from the transfer
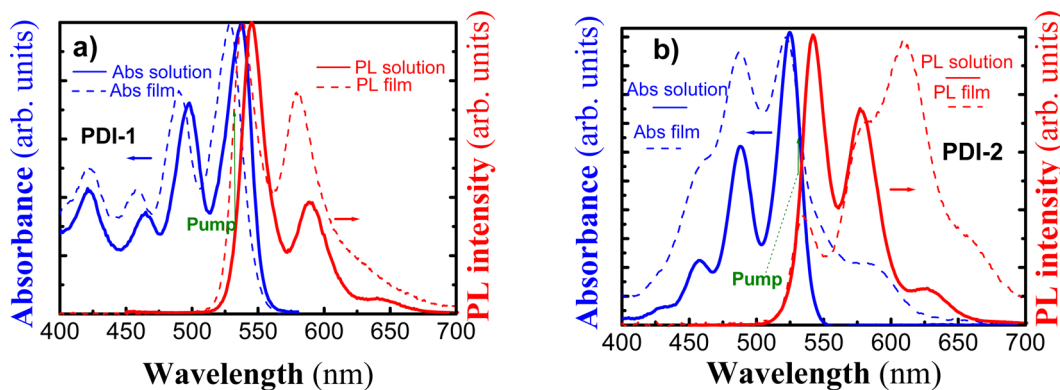

Figure 2. Absorption (blue line and left axis) at 10^{-5} M and photoluminescence (red line and right axis) spectra of the PDIs in toluene solution (solid line) and in PMMA film (dashed line): (a) PDI-1; (b) PDI-2.
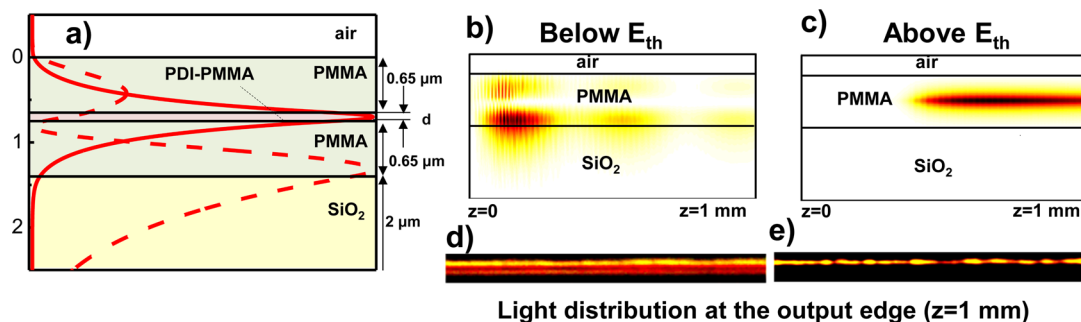
Light distribution at the output edge (z=1 mm)

Figure 3. (a) S_z distribution of the TE_0 (red solid line) and TE_1 (red dashed line) modes calculated at 580 nm (modes at 533 nm present similar distribution). (b, c) Simulations of the waveguided PL along the length of the waveguide (z) pumped below (b) and above (c) ASE threshold; in the first case, both modes are excited, whereas in the second, only the fundamental mode is amplified because it overlaps with the active medium. (d, e) Light distribution measured at the output edge of the waveguide below (d) and above (e) the ASE threshold; in the first case, both TE_0 and TE_1 are observed, whereas only the fundamental mode is present in the second case, as in the simulation (d, e).
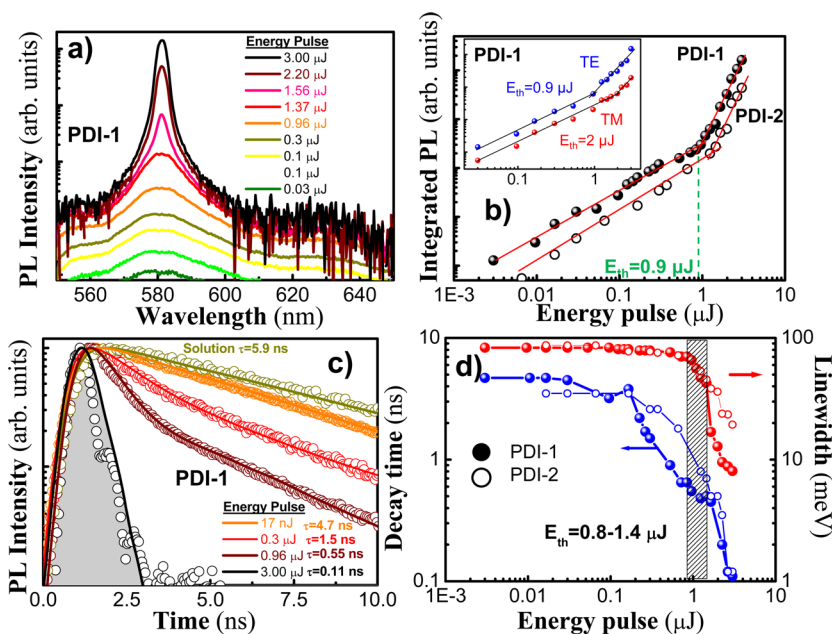

Figure 4. (a) PL spectra for different pump fluencies at the output of a waveguide containing PMMA−PDI-1 composite 100 nm thick sandwiched between 650 nm thick PMMA cladding layers on the top and the bottom of the nanocomposite. (b) Integrated PL of the 0−1 transition as a function of the pump fluence for PDI-1 (solid circles) and PDI-2 (hollow circles). The evolution for TE (blue symbols) and TM (red symbols) is shown in the inset for PDI-1. (c) TRPL spectra (open symbols) for PDI-1 under different laser pump fluencies and exponential fitting curves (continuous lines); gray shaded area corresponds to the temporal system response. (d) Fastest decay time (blue symbols and guide for the eyes) and line width (red symbols and guide for the eyes) as a function of the laser excitation fluence for PDI-1 (solid symbols) and PDI-2 (hollow symbols) compounds.

matrix algorithm. In addition, at the PL wavelength (580 nm), the high confinement factor (Γ) of the TE_0 within the active region ($\Gamma = 26\%$) improves the generation of PL, while the TE_1 has a negligible effect on the amplification because of the poor overlap with the active region.[32] Indeed, BPM simulations, based on a model developed elsewhere,[11−13] revealed that under low laser pumping both modes are excited in the waveguide (Figure 3c), while the TE_0 dominates under high excitation fluencies (Figure 3d). CCD micrographs registered at the output edge of the waveguide containing PDI-1 compound corroborate these simulations: two waveguided PL lines corresponding to the fundamental and first order modes (Figure 3e) are observed at the output face under low laser pumping conditions, while only one line is visible for high excitation fluencies corresponding to the fundamental mode (Figure 3f). At the excitation wavelength (533 nm) BPM

simulations predict the propagation of the TE_0 and TE_1 modes deduced by the transfer matrix method, and at $z = 1$ mm, the calculations reveal a reduction of the signal at $z = 0$ of about 2.7%.

ASE Demonstration. The PDI-1 waveguide exhibits ASE under sufficiently high laser pumping fluence by end fire coupling, as shown in Figure 4a for a structure containing a 100 nm PMMA−PDI-1 layer. Above a certain laser pumping threshold (E_{th}), the intensity of PL collected at the output of the waveguide grows superlinearly with the excitation power and the spectrum collapse into a narrow peak located at the maximum of the 0−1 vibronic transition, being both observations clear signatures of optical gain. Such a generation of inverted population on the 0−1 state is common in organic compounds,[19−22] because this transition corresponds to the excited state of the four-level scheme. Due to this fact, a large

Stokes shift of the PL spectrum is observed relative to the absorption spectra that prevents self-absorption losses.[20] Therefore, the integrated intensity of the 0−1 state PL (I_0) as a function of the laser pump fluence (I_P) clearly exhibits a threshold between the spontaneous and stimulated emission behaviors, as observed in the log−log plot of Figure 4b for waveguides containing the two PDIs described in Table 2. For

Table 2. ASE Properties of the PDI Compounds Used in This Work

	waveguide			
PDI	α_{533nm} (cm^{-1})	λ_{ASE} (nm)	E_{th} (μJ)	$\Delta\lambda$ (nm)
PDI-1	2000	580	0.9	2.5
PDI-2	2000	576	1.2	4.7

low laser pump fluencies, the PL intensity can be approximated by a linear law ($I_{0-1} \propto I_P$), while above E_{th}, we measure a superlinear increase, $I_{0-1} \propto I_P^{3.5}$, which is attributed to the ASE behavior. Following the approximation developed in ref 11, a gain of around 9 dB at the output edge of the waveguide ($\approx$1 mm) is deduced. This gain corresponds to an average modal gain along the 2 mm length of the structure of 20.6 cm^{-1} and a material gain (modal gain divided by the confinement factor) of 80 cm^{-1}. The reduction of the material gain as compared to the maximum calculated in the previous section (2000 cm^{-1}) is due to the attenuation of the pump beam along the structure and the gain saturation effects.[11] The value of E_{th} is observed at around 0.9 and 1.2 μJ for waveguides containing PDI-1 and PDI-2 derivatives, respectively (see Table 2). Here the laser pumping energies inside the waveguide are estimated by assuming $\approx$1% for the coupling efficiency of the laser pumping beam, at the input face and taking into account the overlap of the laser profile with the TE$_0$ mode (Figure 3b).[11] The lowest ASE threshold is found for the PDI-1 system, probably due to the absence of aggregation effects and hence its better emission efficiency, as compared to the case of PDI-2, where H-aggregates in the PMMA matrix were possibly formed as above-mentioned.[14,29] In this sense, although both compounds present similar QY in both solution (see Table 1) and film, PMMA−PDI-1 composite results for a better active purposes.

The laser pumping thresholds reported in Table 2 and Figure 4b correspond to PL signal traveling in TE polarization (see blue symbols in the inset of Figure 4b), because this particular geometry enhances the emission in the plane. Indeed, waveguided PL signal measured under TM polarization (red

symbols in the inset of Figure 4b) was 1 order of magnitude smaller than under TE and consequently exhibits a higher E_{th} ($\approx$2 μJ).

TRPL measurements (symbols in Figure 4c) at the output face of the waveguide are consistent with the discussed spontaneous/ASE transition above E_{th}. When the structure is pumped below E_{th}, the TRPL spectrum exhibits a single exponential decay (solid line), with a decay time $\tau \approx$ 5.9 ns, close to that measured for the toluene solution (see Table 1). However, above E_{th}, the TRPL spectra need to be fitted with two exponentials, where the fast decay component corresponds to the stimulated emission of the 0−1 transition and decreases with the laser pump fluence down to the response of the system (gray area).[19] Results plotted in Figure 4c correspond to the PDI-1 compound, but TRPL analysis for PDI-2 presents a similar behavior (see Supporting Information, S4). The evolution of τ with the laser pump fluence (red curves in Figure 4c) is the second signature of ASE production, with a sharp decrease of τ above E_{th} (shaded area in Figure 4c) for PDI-1 (filled symbols) and PDI-2 (empty symbols). Simultaneously to this decrease of τ with the laser pump fluence, a strong narrowing of the PL spectrum is observed above E_{th} (blue curves in Figure 4d). Here, the waveguides incorporating the PDI-1 compound presents the narrowest line width ($\Delta\lambda$) down to 8 meV (2.4 nm), in agreement with its slightly lower E_{th}. Again, such a narrow $\Delta\lambda$ corresponds to light traveling in TE polarization, while light propagating in TM shows a wider $\Delta\lambda$ (around 9.5 meV), see sections S4 and S5 of the Supporting Information. To the best of our knowledge, this is the narrowest $\Delta\lambda$ obtained with PDI compounds without the aid of an external resonator,[20−22] and it is achieved due to the low propagation losses and high confinement of light in the active layer provided by the particular sandwich geometry of the fabricated optical waveguides.[13]

Optimization of Geometrical Parameters. Stimulated emission was not obtained if a too thick PMMA−PDI layer was used as the core of the waveguide, under similar pumping conditions described above (see the case of a $\approx$1 μm thick PMMA−PDI layer represented by dark yellow symbols in Figure 5a). This is because the propagation of the excitation in this second structure is limited to few microns due to the strong absorption of the compound (2000 cm^{-1} for PDI-1 embedded in PMMA at 5 wt %) together with the high concentrations needed for optical amplification (0.5−5%).[20−22] In fact, in previous publications where the core of the waveguide consisted of a thick composite, surface optical pumping was
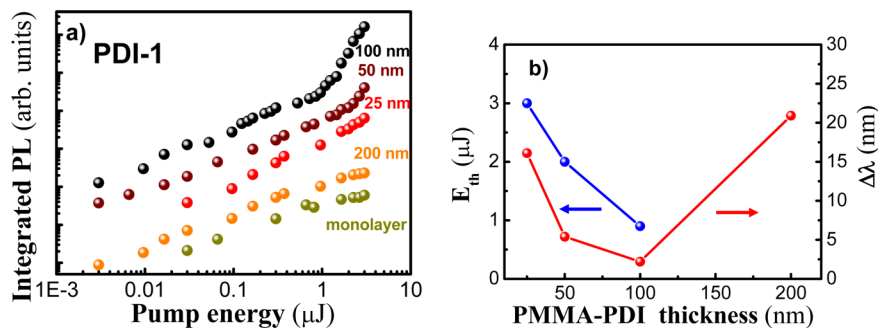
Figure 5. (a) Integrated PL of the 0−1 transition as a function of the laser pump fluence for different thicknesses of the PMMA−PDI-1 active layer. Black, brown, red, and orange colors refer to 100, 50, 25, and 200 nm thickness. Dark yellow show the results obtained with a PMMA−PDI monolayer waveguide, where no amplification was observed. (b) Energy threshold (blue and left axis) and line width (red and left axis) as a fluence function of the thickness of the PMMA−PDI-1 intermediate layer.

required in order to provide a uniform excitation along the whole length of the waveguide, resulting in higher pump thresholds (1.2−100 μJ)[20−22] and broader line widths (3.5−7 nm).[33] Indeed, as far as we know, there is only one publication where the concentration of PDI was properly optimized inside a polystyrene matrix leading to $E_{th} \approx 0.5~\mu$J[22] at the expense of an increase in the ASE line width.[33] By maintaining the same PDI concentration in PMMA, the thickness of the PMMA−PDI composite in our waveguide structures is thus a critical parameter to optimize the ASE conditions. In our waveguide structures, an intermediate layer of PMMA−PDI, 200 nm thick, seriously limits the propagation of the laser pumping beam and no ASE is observed (orange symbols in Figure 5a), exhibiting a production of waveguided PL light as low as a single monolayer of the composite (green symbols). If the layer is too thin (25 nm, red symbols), there are not enough molecules to overcome E_{th}, and ASE generation is observed for thicknesses in the range 50−100 nm (brown and black symbols, in Figure 5a). A PMMA−PDI layer 100 nm thick demonstrated the optimum ASE generation with the lowest E_{th} (0.9 μJ) and the narrowest line width (2.3 nm), as shown in Figure 5b.

Moreover, ASE is maintained over 2×10^4 and 6×10^3 laser shots for PMMA−PDI thicknesses of 50 and 100 nm, respectively (see Figure 6), while previous works on thicker
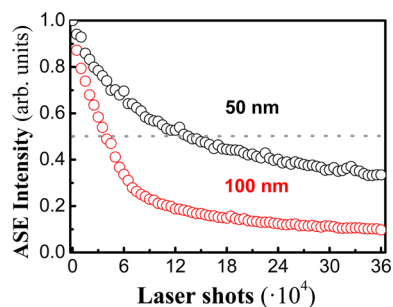

Figure 6. ASE intensity as a function of laser shots in waveguides containing 50 and 100 nm thick PMM−PDI-2 layers.

PMMA−PDI composites reported poorer stability down to 10^3 laser shots. Indeed, stimulated emission was generated with a repetition rate of 100 Hz, rather than the 10−20 Hz usually needed for similar organic compounds.[20−22,32,33] We suggest that this instability in ASE found in this kind of compound[20] is mainly due to their photochemical local bleaching. Indeed, usually there are photochemical reactions resulting in photo-induced modifications (usually oxidation) of organic molecules under air atmosphere conditions. Even if the reactions are of very low quantum yield, the bleaching effect will accumulate with the number of laser shots. Concerning the effect of the photostability decrease with the active layer thickness, we suggest that this effect may be due to the contribution of a temperature-dependent nonradiative deactivation channel: we believe that an increase of the sample temperature, which is evidently higher for the thicker (and more absorbing) layer, can activate additional nonradiative deactivation channels, which decrease amplification efficiency. Additional experiments are required to elucidate a mechanism of the observed effect, but following our preliminary observations, natural cooling of the thicker sample during a few hours partially restores the ASE efficiency.

CONCLUSIONS

In conclusion, we have proposed a new type of a polymer-based optically active planar waveguide providing unprecedented long-distance joint propagation of an excitation and PL beams. By properly optimizing the geometrical parameters it became possible to demonstrate the amplified spontaneous emission with a threshold as low as 0.9 μJ and a line width of 2.3 nm when highly luminescent and stable organic molecules such as PDIs are used as an active material. The device can be considered as a prototype of an efficient on-chip amplifier for optical integrated circuits, for example in visible light optical communications and disposable sensors.

EXPERIMENTAL METHODS

Synthesis. All chemicals were reagent grade, purchased from commercial sources, and used as received, unless otherwise specified. Column chromatography: SiO_2 (40−63 mm) TLC plates coated with SiO_2 60F254 were visualized by UV light. NMR spectra were measured with a Bruker AC 300. UV/vis spectra were recorded with a Helios Gamma spectrophotometer. Fluorescence spectra were recorded with a PerkinElmer LS 55 Luminescence Spectrometer. Mass spectra were obtained from a Bruker Microflex matrix-assisted laser desorption/ionization time-of-flight (MALDI-TOF).

Waveguide Fabrication. PMMA−PDI composites have been prepared by mixing PDI and PMMA solutions diluted in toluene with the appropriate proportion (5% wt of PDI in PMMA). Then, waveguides were fabricated by spin coating the PMMA (for cladding layers) and composite solutions on a SiO_2/Si substrate (2 μm SiO_2) supplied by CEMAT Silicon S.A. and baking the film at 80 and 150 °C for 2 min in both two-step baking temperatures. The thickness of the layers was controlled by the viscosity and speed of the spin coating machine. The sandwich waveguide structure was fabricated by a successive deposition of PMMA, PMMA−PDI, and PMMA layers.

Optical Experiments. Absorption experiments in the film and solution were carried out with a commercial a Shimadzu UV-2501PC spectrophotometer (UV-visible range). The PL characterization of the PDI solutions was carried out by using a continuous wave laser diode at 450 nm as excitation and backscattered emitted light detected by a HR4000 Ocean Optics spectrograph. Amplification experiments were performed by end fire coupling a Q-switch pulsed DPSS Nd:Yag laser doubled to 533 nm (100 Hz, 1 ns), CRYLAS 6FTSS355-Q4-S, at the input edge of the waveguide with the aid of a 40× microscope objective, and collecting the waveguided PL from the output edge of the structure with the same HR4000 Ocean Optics spectrograph (having an overall resolution better than 0.7 nm). Time-resolved PL was carried out by using the same pumping laser, but analyzing the PL with a Hamamatsu C5658−3769 avalanche photodetector connected to a BOXCARDPCS-150 electronics from Becker and Hickl GmbH.

ASSOCIATED CONTENT

Ⓢ Supporting Information

The Supporting Information is available free of charge on the ACS Publications website at DOI: 10.1021/acsphotonics.6b00666.

Additional information (PDF).

AUTHOR INFORMATION

Corresponding Authors

*E-mail: isaac.suarez@uv.es.

*E-mail: fdofdez@umh.es.

ORCID

Isaac Suárez: 0000-0002-2773-8801

Author Contributions

M.S. has made most of the experimental work related to the fabrication and optical characterization of films and photonic structures. N.Z.-L. has developed the synthesis of the molecular compounds and their spectroscopic characterization in solution.

Notes

The authors declare no competing financial interest.

REFERENCES

(1) Samuel, I. D. W.; Turnbull, G. A. Organic Semiconductor Lasers. *Chem. Rev.* **2007**, *107*, 1272−1295.

(2) Grivas, C.; Pollnau, M. Organic solid-state integrated amplifiers and lasers. *Laser Photonics Rev.* **2012**, *6*, 419−462.

(3) Chénais, S.; Forget, S. Recent advances in solid-state organic lasers. *Polym. Int.* **2012**, *61*, 390−406.

(4) Dang, C.; Lee, J.; Breen, C.; Steckel, J. S.; Coe-Sullivan, S.; Nurmikko, A. Red, G reen, and Blue Lasing enabled by Single-Exciton Gain in Colloidal Qu antum Dot Films. *Nat. Nanotechnol.* **2012**, *7*, 335−339.

(5) Grim, J. Q.; Christodoulou, S.; Di Stasio, F.; Krahne, R.; Cingolani, R.; Manna, L.; Moreels, I. Continuous-wave biexciton lasing at room temperature using solution-processed quantum wells. *Nat. Nanotechnol.* **2014**, *9*, 891−895.

(6) Xing, G.; Mathews, N.; Lim, S. S.; Yantara, N.; Liu, X.; Sabba, D.; Grätzel, M.; Mhaisalkar, S.; Sum, T. C. Low-temperature solution-processed wavelength-tunable perovskites for lasing Guichuan. *Nat. Mater.* **2014**, *13*, 476−480.

(7) Dal Negro, L.; Bettotti, P.; Cazzanelli, M.; Pacifici, D.; Pavesi, L. Applicability conditions and experimental analysis of the variable stripe length method for gain measurements. *Opt. Commun.* **2004**, *229*, 337−348.

(8) Gordillo, H.; Suárez, I.; Abargues, R.; Rodríguez-Cantó, P. J.; Martínez-Pastor, J. P. Color Tuning and White Light by Dispersing CdSe, CdTe, and CdS in PMMA Nanocomposite Waveguides. *IEEE Photonics J.* **2013**, *5*, 2201412.

(9) Grivas, C. Optically pumped planar waveguide lasers, Part I: Fundamentals and fabrication techniques. *Prog. Quantum Electron.* **2011**, *35*, 159−239.

(10) Grivas, C. Optically pumped planar waveguide lasers: Part II: Gain media, laser systems, and applications. *Prog. Quantum Electron.* **2016**, *45−46*, 3−160.

(11) Suárez, I.; Juárez-Pérez, E. J.; Bisquert, J.; Mora-Seró, I.; Martínez-Pastor, J. P. Polymer/Perovskite Amplifying Waveguides for Active Hybrid Silicon Photonics. *Adv. Mater.* **2015**, *27*, 6157−6162.

(12) Gordillo, H.; Suárez, I.; Abargues, R.; Rodríguez-Cantó, P. J.; Almuneau, G.; Martínez-Pastor, J. P. Quantum-Dot Double Layer PolymerWaveguides by Evanescent Light Coupling J. *J. Lightwave Technol.* **2013**, *31*, 2515−2525.

(13) Suárez, I.; Larrue, A.; Rodríguez-Cantó, P. J.; Almuneau, G.; Abargues, R.; Chirvony, V. S.; Martínez-Pastor, J. P. Efficient excitation of photoluminescence in a two-dimensional waveguide consisting of a quantum dot-polymer sandwich-type structure. *Opt. Lett.* **2014**, *39*, 4962−4965.

(14) Figueira-Duarte, T. M.; Mullen, K. Pyrene-based materials for organic electronics. *Chem. Rev.* **2011**, *111*, 7260−7314.

(15) Huang, C.; Barlow, S.; Marder. PeryleneS,R, −3,4,9,10-tetracarboxylic acid diimides: synthesis, physical properties, and use in organic electronics. *J. Org. Chem.* **2011**, *76*, 2386−2407.

(16) Fernández-Lázaro, F.; Zink-Lorre, N.; Sastre-Santos, A. Perylenediimides as non-fullerene acceptors in bulk-heterojunction solar cells (BHJSCs). *J. Mater. Chem. A* **2016**, *4*, 9336−9346.

(17) Usta, H.; Facchetti, A.; Marks, T. J. n-Channel semiconductor materials design for organic complementary circuits. *Acc. Chem. Res.* **2011**, *44*, 501−511.

(18) Morales-Vidala, M.; Bojb, P. G.; Quintana, J. A.; Villalvilla, J. M.; Retolazac, A.; Merinoc, S.; Díaz-García, M. A. Distributed feedback lasers based on perylenediimide dyes for label-free refractive index sensing. *Sens. Actuators, B* **2015**, *220*, 1368−1375.

(19) Yu, Z.; Wu, Y.; Liao, Q.; Zhang, H.; Bai, S.; Li, H.; Xu, Z.; Sun, C.; Wang, X.; Yao, J.; Fu, H. Self-Assembled Microdisk Lasers of Perylenediimides. *J. Am. Chem. Soc.* **2015**, *137*, 15105−15111.

(20) Ramírez, M. G.; Pla, S.; Boj, P. G.; Villalvilla, J. M.; Quintana, J. A.; Díaz-García, M. A.; Fernández-Lázaro, F.; Sastre-Santos, Á. Perylenediimide derivative with Outstanding Laser Performance. *Adv. Opt. Mater.* **2013**, *1*, 933−938.

(21) Cerdán, L.; Costela, A.; Durán-Sampedro, G.; García Moreno, I.; Calle, M.; Juan-y-Seva, M.; de Abajo, J.; Turnbull, G. A. New perylene-doped polymeric thin films for efficient and long-lasting lasers. *J. Mater. Chem.* **2012**, *22*, 8938−8947.

(22) Ramírez, M. G.; Morales-Vidal, M.; Navarro-Fuster, V.; Boj, P. G.; Quintana, J. A.; Villalvilla, J. M.; Reolaza, A.; Merino, S.; Díaz-García, M. A. Improved performance of perylenediimide-based lasers. *J. Mater. Chem. C* **2013**, *1*, 1182−1191.

(23) He, L.; Ozdemir, S. K.; Yang, L. Whispering gallery microcavity lasers. *Lasers Photonics Rev.* **2013**, *7*, 60−82.

(24) Amarasingue, D.; Ruseckas, A.; Turnbull, G. A.; Samuel, I. D. W. Organic Semiconductor Optical Amplifiers. *Proc. IEEE* **2009**, *97*, 1637−1650.

(25) Clark, J.; Lanzani, G. Organic photonics for communications. *Nat. Photonics* **2010**, *4*, 438−446.

(26) Scotognella, F.; Lanzani, G.; Antognazza, M. R. Breakthroughs in Photonics 2012: Breakthroughs in Organic Photonic Sensors. *IEEE Photonics J.* **2013**, *5*, 0701106.

(27) Koike, Y.; Asai, M. The future of plastic optical fiber. *NPG Asia Mater.* **2009**, *1*, 22−28.

(28) Zink-Lorre, N.; Font-Sanchis, E.; Sastre-Santos, A.; Fernández-Lázaro, F. Easy and mild fluoride-mediated direct mono- and dialkoxylation of perylenediimides. *Dyes Pigm.* **2016**, *127*, 9−17.

(29) Calzado, E. M.; Villalvilla, J. M.; Boj, P. G.; Quintana, J. A.; Gómez, R.; Segura, J. L.; Díaz-García, M. A. Effect of Structural Modifications in the Spectral and Laser Properties of Perylenediimide Derivatives. *J. Phys. Chem. C* **2007**, *111*, 13595−13605.

(30) Saleh, B. E. A.; Teich, M. C., Eds. In *Fundamentals of Photonics*; John Wiley & Sons, 1991.

(31) Lifante, G. *Integrated Photonics: Fundamentals*; John Wiley Sons, 2003.

(32) Calzado, E. M.; Ramírez, M. G.; Boj, P. G.; Díaz García, M. A. Thickness dependence of amplified spontaneous emission in low-absorbing organic waveguides. *Appl. Opt.* **2012**, *51*, 3287−3293.

(33) Calzado, E. M.; Villalvilla, J. M.; Boj, P. G.; Quintana, J. A.; Gómez, R.; Segura, J. L.; Díaz García, M. A. Amplified spontaneous emission in polymer films doped with a perylenediimide derivative. *Appl. Opt.* **2007**, *46*, 3836−3842.

Supporting Information

Efficient optical amplification in a sandwich-type active-passive polymer waveguide containing perylenediimides

Mattia Signoretto [1], Nathalie Zink-Lorre [2], Isaac Suárez [1]*, Enrique Font-Sanchis [2], Ángela Sastre-Santos [2], Vladimir S. Chirvony [1], Fernando Fernández-Lázaro [2]* and Juan P. Martínez-Pastor[1]

S1. Synthesis of 2,5,8,11-diphenylphenoxyperylene-3,4:9,10-tetracarboxydiimide (PDI-1)

A mixture of 206 mg (0.84 mmol) of 2,6-diphenylphenol, 91 mg (0.6 mmol) of CsF and 360 mg (2.4 mmol) of 18-crown-6 were added to a solution of 70 mg (0.06 mmol) of 2,5,8,11-tetrabromoperylene-3,4:9,10-tetracarboxydiimide in dry THF (2 mL). The reaction was refluxed 24 hours under argon atmosphere and, after cooling, it was extracted with dichloromethane and washed with water. The organic layer was dried over anhydrous sodium sulfate, filtered and evaporated. Purification was carried out by silica gel column chromatography using CH_2Cl_2: hexane 1:1 as eluent yielding 93 mg (90%) of **PDI-1** as an orange powder.

- ^{1}H NMR (300 MHz, CDCl$_3$) δ 0.93 (m, 12H), 1.35 (m, 32H), 1.85 (m, 4H), 2.31 (m, 4H), 5.24 (m, 2H), 6.25 (s, 4H), 7.11 (m, 25H), 7.45 (m, 15H), 7.55 (m, 8H) and 7.67 ppm (m, 4H)
- ^{13}C NMR (75 MHz, CDCl$_3$) δ 159.51, 146.69, 136.83, 136.82, 136.81, 135.51, 133.31, 132.78, 130.83, 129.33, 129.01, 128.82, 128.04, 127.52, 127.01, 116.20, 109.29, 53.29, 32.31, 31.99, 30.89, 29.43, 26.83, 22.72 and 14.18 ppm
- IR (KBr): 3078, 2921, 2845, 1689, 1654, 1549, 1404, 1369, 1299, 1188, 750 and 698 cm^{-1}.
- UV-Vis (CH_2Cl_2), λ_{max}/nm (log ε): 421 (4.3), 460 (4.2), 493 (4.6) and 532 (4.8)
- HRMS (MALDI-TOF): m/z for $C_{122}H_{110}N_2O_8$ calc. 1730.8256; found 1730.8291 (M$^+$).
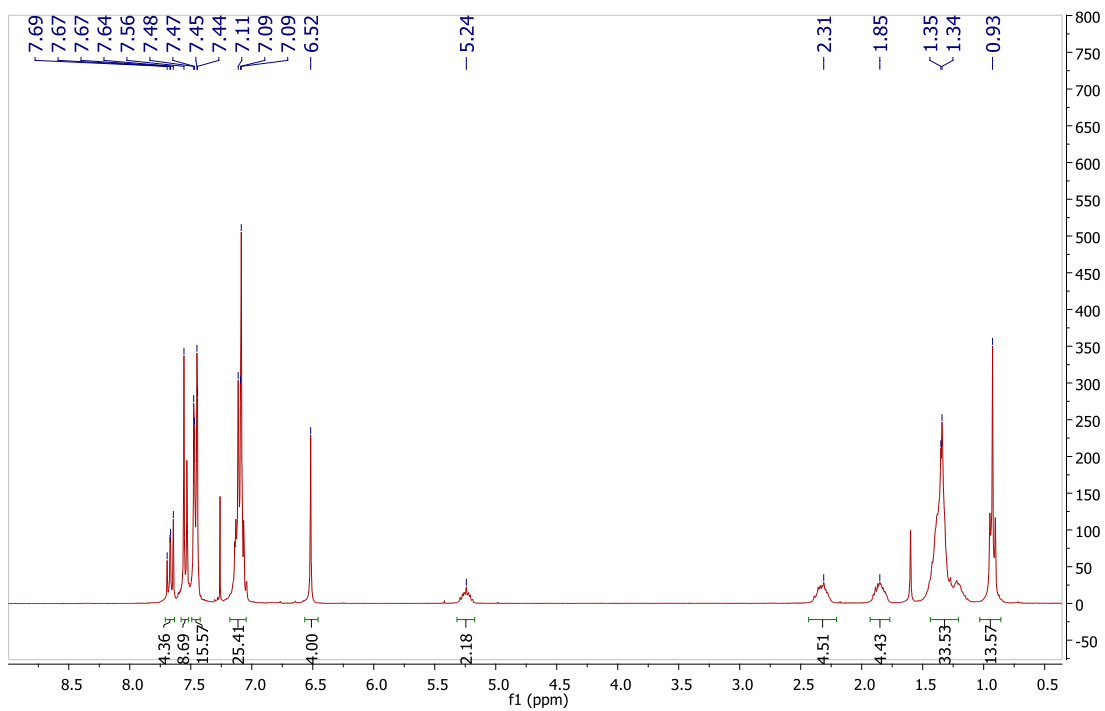
Figure S1:. ^{1}H NMR spectrum of **PDI-1** in CDCl$_3$.
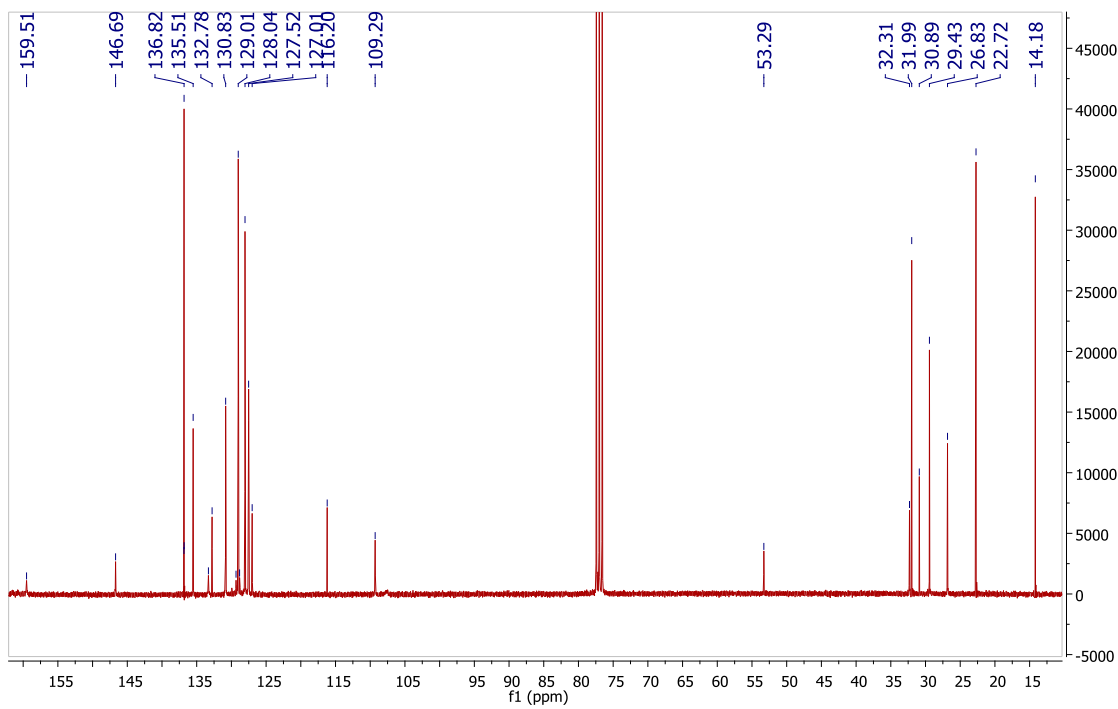
Figure S2: ^{13}C NMR spectrum of **PDI-1** in CDCl$_3$
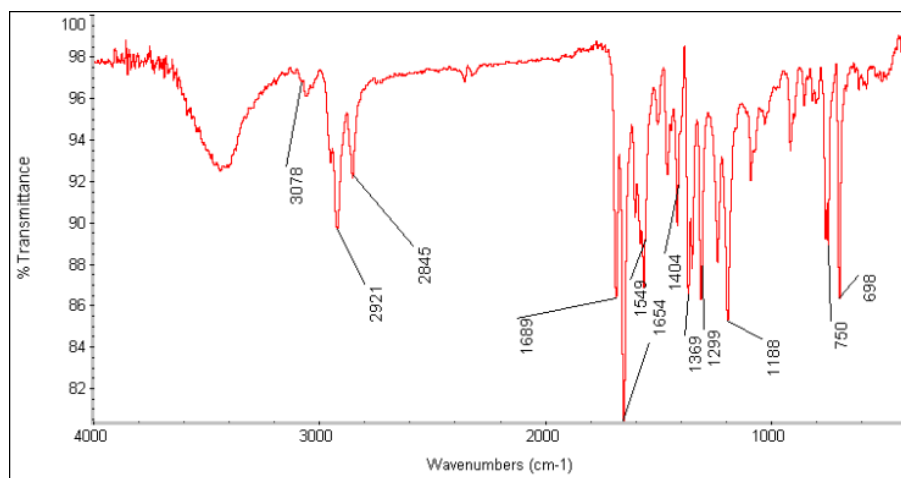
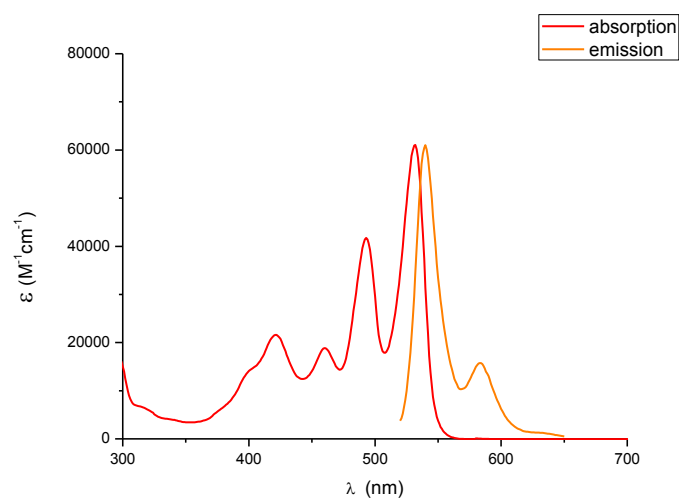**Figure S3** IR spectrum (KBr) of **PDI-1**

Figure S4: UV-vis spectrum of **PDI-1** in CH_2Cl_2
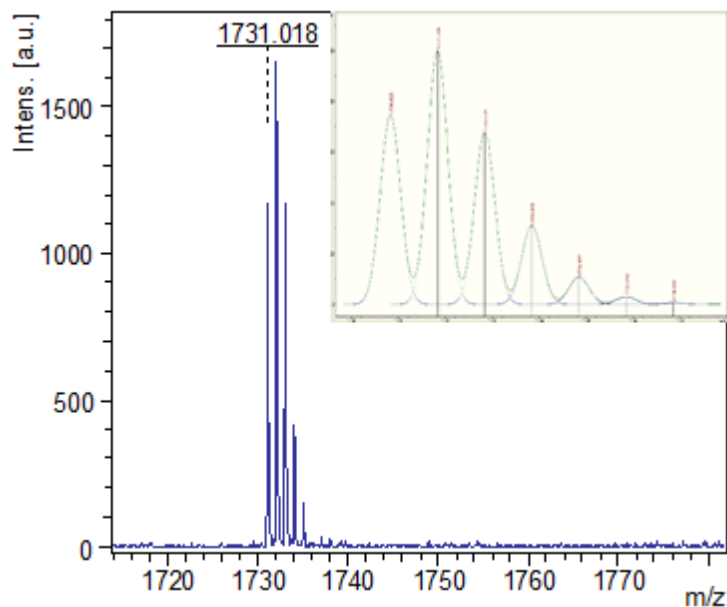
Figure S5: MALDI-TOF of **PDI-1**

S2. Deconvolution of waveguided PL spectra

Waveguided PL spectra have been deconvoluted as a function of energy in order to stablish the influence of each transition. At low excitation fluencies the PL spectra measured at the output edge of the waveguide can be deconvoluted into four Gaussian contributions (Figure S6a), while at high excitation fluencies, above the ASE threshold, the waveguided signal collapses into a narrow Lorentzian line (Figure S6b). The PL spectrum of the PMMA-PDI-1 film measured in backscattering configuration resembles to that shown in Figure S6b.

Figure S6. Deconvolution of PL spectra at the output edge of the waveguide. a) At an excitation fluence of 30 nJ measured PL spectra can be deconvoluted into four Gaussian contributions. b) At an excitation fluence of 3 μJ the spectra collapses into a dominant Lorentzian peak at the energy of the 0-1 transition.

4

S3. Refractive index of the PMMA-PDI composite.

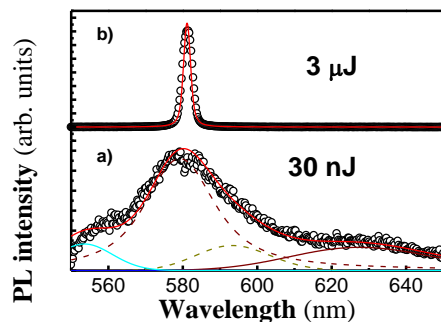Refractive index of the PMMA-PDI-1 (PMMA-PDI presents a similar refractive index) composite has been estimated from the reflectivity spectra of a 0.6 nm thick film deposited on a silicon substrate (Figure S7a) and the absorption of the film deposited on glass (Figure 2 of the text and S2). Then, real part of the refractive index (blue line in Figure S7b) has been estimated from the fringes in the reflectivity spectra, and the imaginary part of the refractive index (red line in Figure S7b) from the absorption spectra. Theoretical reflectivity calculated with this refractive index (red line in Figure S7a) agrees with the experimental results (symbols in Figure S7a).
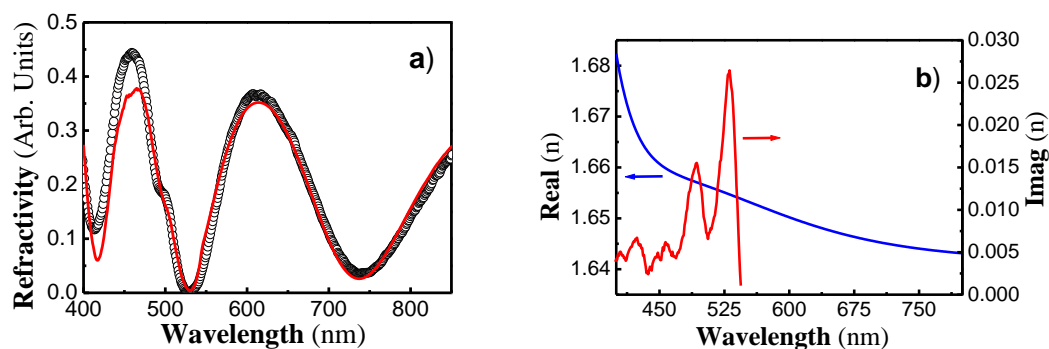

Figure S7. a) Experimental and theoretical reflectiviy of a PMMA-PDI-1 film deposited on silicon. b) Real part (blue line and left axis) and imaginary part (red line and right axis) of the extracted refractive index for the PMMA-PDI-1 composite.

S4. ASE results for PDI-2 derivative.

S4.1. Spectra.
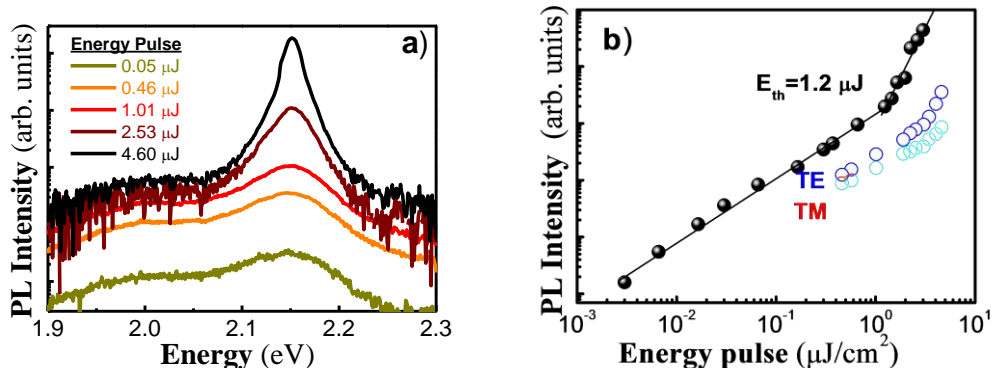
Figure S9. a) PL spectra for different pump fluencies at the output of a waveguide containing PMMA-PDI-2 composite 100 nm thick sandwiched between 650 nm thick PMMA cladding layers on the top and the bottom of the nanocomposite. b) Integrated PL of the 0-1 transition as a function of the pump fluence for the same device without polarization (black solid symbols) and TE (blue hollow symbols) and TM (cyan hollow symbols) polarizations.

S4.2. Decay time of waveguided PL with laser pumping energy.
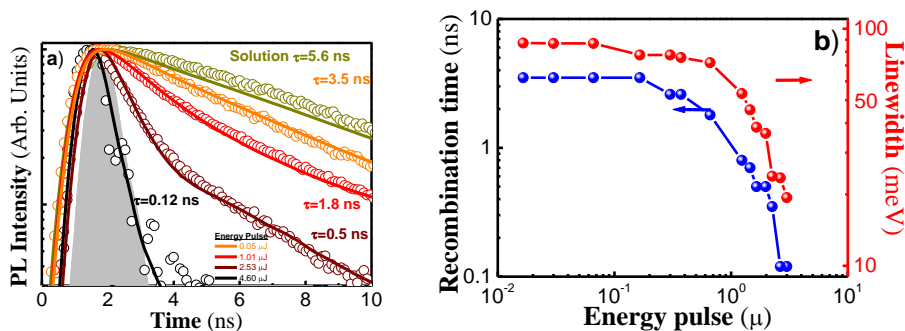
Figure S10. a) TRPL spectra registered for different pump fluencies at the output of a waveguide containing PMMA-PDI-2 composite 100 nm thick sandwiched between 650 nm thick PMMA cladding layers on the top and the bottom of the nanocomposite; the symbols correspond to the experimental data and continuous line to mono-/bi- exponential fitting curves; grey dashed area stands for the system temporal response. b) Fastest decay time (blue symbols and guide for the eyes) and linewidth (red symbols and guide for the eyes) in the same device as a function of the laser excitation fluence for PDI-2 compound.

6

S4.3. Stability.
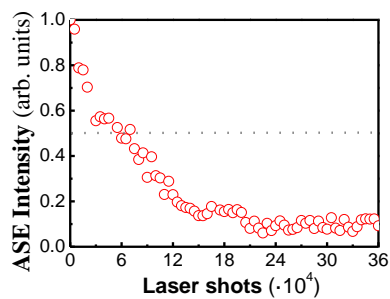
Figure S11. ASE intensity of a waveguide containing a 100 nm of PMM-PDI-2 layer as a function of laser shots.

S5. Polarization dependence of figures of merit for PDI-1 derivative.
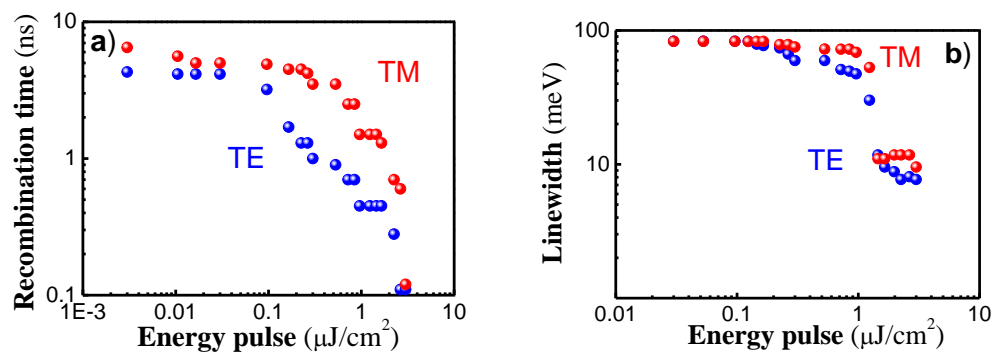
Figure S8. Fast decay time (a) and linewidth (b) as a function of the laser excitation fluence for PDI-1 compound in the same waveguide device studied in the body of the paper under TM (red symbols) and TE (blue symbols) polarizations.

Polymer waveguide couplers based on metal nanoparticle–polymer nanocomposites

**M Signoretto[1], I Suárez[1], V S Chirvony[1], R Abargues[2],
P J Rodríguez-Cantó[2] and J Martínez-Pastor[1]**

[1] UMDO (Unidad Asociada al CSIC-IMM), Instituto de Ciencia de Materiales, Universidad de Valencia,
PO Box 22085, 46007 Valencia, Spain
[2] Intenanomat S.L, C/Catedrático José Beltrán 2, 46980 Paterna, Spain

E-mail: isaac.suarez@uv.es

CrossMark

Abstract

In this work Au nanoparticles (AuNPs) are incorporated into poly(methyl methacrylate) (PMMA) waveguides to develop optical couplers that are compatible with planar organic polymer photonics. A method for growing AuNPs (of 10 to 100 nm in size) inside the commercially available Novolak resist is proposed with the intention of tuning the plasmon resonance and the absorption/scattering efficiencies inside the patterned structures. The refractive index of the MNP–Novolak nanocomposite (MNPs: noble metal nanoparticles) is carefully analysed both experimentally and numerically in order to find the appropriate fabrication conditions (filling factor and growth time) to optimize the scattering cross section at a desired wavelength. Then the nanocomposite is patterned inside a PMMA waveguide to exploit its scattering properties to couple and guide a normal incident laser light beam along the polymer. In this way, light coupling is experimentally demonstrated in a broad wavelength range (404–780 nm). Due to the elliptical shape of the MNPs the nanocomposite demonstrates a birefringence, which enhances the coupling to the TE mode up to efficiencies of around 1%.

Keywords: scattering, waveguide, metal nanoparticle, polymer

(Some figures may appear in colour only in the online journal)

1. Introduction

The interaction of light with noble metal nanoparticles (MNPs) provides the basis for such important applications as the confinement of an electromagnetic field and the redirection of photons [1]. These properties arise from the localized surface plasmon resonance (LSPR) produced when an incident beam is coupled to the free electrons located at the boundary of the metal [2]. As a consequence, a strong near field is manifested at the surface of these nanostructures, and it becomes possible to enhance and extremely confine the electromagnetic field [3]. Moreover, MNPs possess high scattering cross sections that have been widely used to improve the efficiencies of solar cells by light trapping [4, 5]. Besides, the redirection of light by MNPs has also been exploited in guided light applications. For example, the propagation of highly confined light in MNP chains [6] or thin films of disordered Au MNPs has been demonstrated [7]. In

addition, light scattering by MNPs has been exploited to couple light into different waveguide platforms. For these purposes, a grating of MNPs has been formed on a Si_3N_4 membrane [8], Yagi–Uda nanoantennas have been integrated into Si_3N_4 waveguides [9], an antenna consisting of two MNPs separated adequately has been used as a light coupler on a silicon waveguide [10], Au nanodisks have been deposited on a thick TiO_2 layer [11] or the coupling between MNP chain modes and silicon waveguides has been provided [12, 13]. However, in all these examples of MNP-based light coupling into waveguides, rather complex methods of MNP integration were exploited. For this reason, more simple and robust technologies are desirable for the incorporation of MNPs into different photonic structures. An interesting alternative is the incorporation of MNPs into a host matrix to form a nanocomposite in order to combine the properties of the nanoparticles with the technological feasibilities of a matrix [14]. However, the *ex situ* dispersion of colloidal

MNPs in a solid state matrix is usually rather complicated because it requires a ligand exchange to improve solubility and a careful surface treatment to avoid inhomogeneity problems.

Recently we proposed a technology which is able to overcome these limitations and consists of *in situ* synthesis of Ag and Au MNPs in poly(vinyl alcohol) (PVA) and the commercially available resist Novolak [15]. Then, the resulting nanocomposites consisting of MNPs homogeneously dispersed in the matrix were patterned by e-beam or UV lithography [16]. Moreover, MNPs embedded in the polymer can act as seeds if the nanocomposite is immersed into a solution of the precursor metal salt. As a consequence, the size of MNPs in the polymer can be increased even until a complete metallization [17]. In this way, the intensity and position of the MNP plasmonic resonance can be tuned by two degrees of freedom: the initial filling factor of MNPs inside a polymer and the final size controlled by the growing time. Such a possibility of controlling the process of fabrication, together with the lithographic properties of the matrix, make this nancomposite an interesting material for novel photonic and plasmonic devices.

In this work, AuNP-Novolak nanocomposite is proposed as a light coupler for poly(methyl methacrylate) (PMMA) waveguides fabricated on a silicon platform. For this purpose, fabrication conditions are experimentally optimized in order to maximize the scattering cross section by engineering the optical and plasmonic properties of the nanocomposite by tuning the filling factor and size of MNPs inside the film. When the nanocomposites are patterned before the fabrication of PMMA waveguides it becomes possible to couple normal incident light to dielectric modes propagating in PMMA in a broad wavelength range (400–780 nm). The nanocomposite exhibits a certain optical birefringence that is attributed to the elliptical shape of the MNPs. These modes can be coupled to the ones of the PMMA waveguide with coupling efficiencies reaching up to 1% in TE polarization when scattering becomes the dominant effect of MNPs as compared to absorption. These coupling efficiencies are directly measured from light leaving at the output face of the waveguide and the obtained values are competitive with the ones observed in the case of standard coupling methods, such as prism coupling, gratings, or end-fire coupling. The present coupling method is simpler in realization and demonstrates a wider wavelength operation range. Mie theory is used to estimate absorption and scattering cross sections in metal nanoparticles in order to support semiquantitatively the observed increase in waveguided light intensity when increasing the size of MNPs. A Maxwell–Garnett approach is used to estimate the volume fraction occupied by AuNPs in AuNP–Novolak nanocomposite films on the basis of the measured reflectance of the AuNP–Novolak nanocomposite deposited on Si.

2. Experimental methods

MNPs are integrated together with a PMMA waveguide following the scheme shown in figure 1. A thin PMMA layer
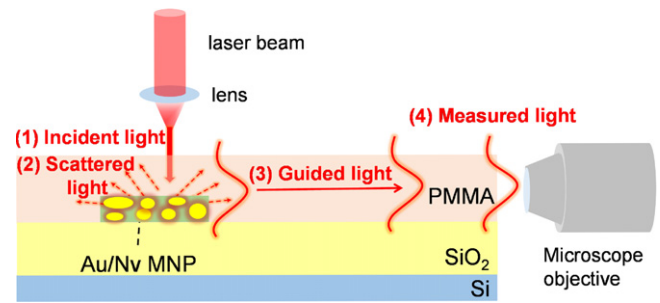

Figure 1. The sample structure and experimental setup. The AuNP–Novolak nanocomposite is patterned on a SiO_2/Si wafer and a PMMA film is deposited on the top. An incident laser beam (1) is focused on the surface of the nanocomposite to scatter the light by the AuNPs (2). Finally, the scattered light is coupled to the guided modes (3) of the $PMMA/SiO_2$ structure and collected at the output edge of the sample (4).

acts as a core of a planar waveguide when it is deposited on a SiO_2/Si wafer due to the high index contrast of the polymer relative to SiO_2 [14]. Then AuNPs are incorporated in the structure by two different methods. First, a AuNP–Novolak (Nv) nanocomposite can be patterned on the top of the PMMA, and second, the nanocomposite can be structured on the SiO_2/Si wafer prior to the PMMA deposition. Then, by controlling the size of the MNP in the polymer, it is possible to maximize the scattering of a vertically incident laser beam at a specific wavelength. Due to this scattering, the incident light is coupled into the PMMA waveguide.

2.1. Nanocomposite fabrication

AuNP–Nv nanocomposite films are prepared following the procedure explained in [17]. Initial gold seed solutions were made by mixing a Nv photoresist with 0.1 M Au(III), both dissolved in methoxy propil acetate (MPA). Then the Au-Nv suspension is spin coated on the appropriate substrate and post-baked at 180 °C for 10 min to initiate the formation of AuNPs in Nv. At the end of the process films of thickness 100–200 nm, containing AuNPs of around 10–20 nm in diameter, were synthesized. Films with different concentrations of AuNPs in Nv (volume ratios of initial solutions of Nv to Au salt of 1:1, 1:0.1, 1:0.01, where the initial Nv solution was the commercial ma-P1205 resist from microresist technology GmbH, and the initial Au solution was 0.197 g of Au(III) ($HAuCl_4$-$3H_2O$, 0.1 M) dissolved in 0.5 ml of MPA) were deposited on silicon and glass substrates in order to study the influence of the filling factor (*ff*), defined as the ratio of the volume occupied by AuNPs to the whole volume of the composite, on the plasmonic resonances. To increase the size of the seed gold nanoparticles the nanocomposite was immersed in a growing solution containing H_3NOHCl with Au in ethanol. The growth reaction is carried out at a controlled temperature of 45 °C from minutes to several hours until the desired nanoparticle size is reached.

2.2. Waveguide fabrication

AuNP–Nv nanocomposites were firstly patterned on a SiO_2/ Si (2 μm of SiO_2) substrate supplied by CEMAT Silicon S.A. in order to define the MNP-containing zones in the final waveguide. The procedure consisted of an initial bake at 65 °C for 2 min prior to the UV illumination for 4 s and the consequent development. At the end of the process AuNP–Nv patterns were post-baked at 180 °C to initiate the formation of MNPs. Then the samples were immersed in the growing solution until the MNPs reached the desired size.

Once an AuNP nanocomposite is properly prepared a PMMA layer is spin coated on the top of the sample and post baked at 80 °C and 150 °C for two minutes each bake [14]. The thickness of the PMMA was around 2 μm. Finally, the edges of the samples were cleaved for end-fire coupling purposes.

2.3. Characterization methods

Reflectivity and transmission measurements were carried out for AuNP–Nv films deposited on silicon and glass substrates, respectively, by using a commercial reflectometer (Nanocalc-2000 from Mikropak/Ocean).

Coupling of light into the waveguide was performed with the experimental set up shown in figure 1. A laser beam is focused on the surface of the sample under normal incidence with the aid of an aspherical lens (focal length 11 mm, numerical aperture 0.25). Incident light is carefully positioned in the region with AuNPs in order to maximize the scattering of light. Then a guided light travelling along the PMMA waveguide is collected at the output edge of the sample by using a 20x microscope objective (numerical aperture 0.35), which focuses the guided light into an HR4000 Ocean Optics spectrograph. The waveguide length (between the edge of the sample and the MNP region) was fixed at around 2 mm and different continuous wave (CW) lasers were used to test the light optical coupling by AuNPs into the PMMA waveguides in a broad range of wavelengths: 404 nm and 450 nm (semiconductor lasers), 533 nm (Nd laser), 590 nm and 633 nm (HeNe lasers), and 780 nm (semiconductor laser).

3. Nanocomposite characterization

Samples with different Au-precursor concentrations in the polymer (1:1, 1:0.1, 1:0.01 volume ratios of Nv to Au-precursor in solution) were prepared to study the influence of this parameter in the optical properties in the Nv–AuNP nanocomposite once the MNPs are formed. Under these conditions the prepared nanocomposite contained AuNPs with an initial average diameter of around 10 nm and an *ff* of $10^{-3}, 5 \cdot 10^{-4}$, 10^{-4}. Figure 2 shows SEM images of the AuNPs obtained at different growth times in a nanocomposite film deposited on a silicon wafer for the case of an initial *ff* of $5 \cdot 10^{-4}$ (the nanocomposites obtained for other concentrations demonstrate similar behaviors). When these nanocomposite films are immersed in the growing solution, the size of the AuNPs
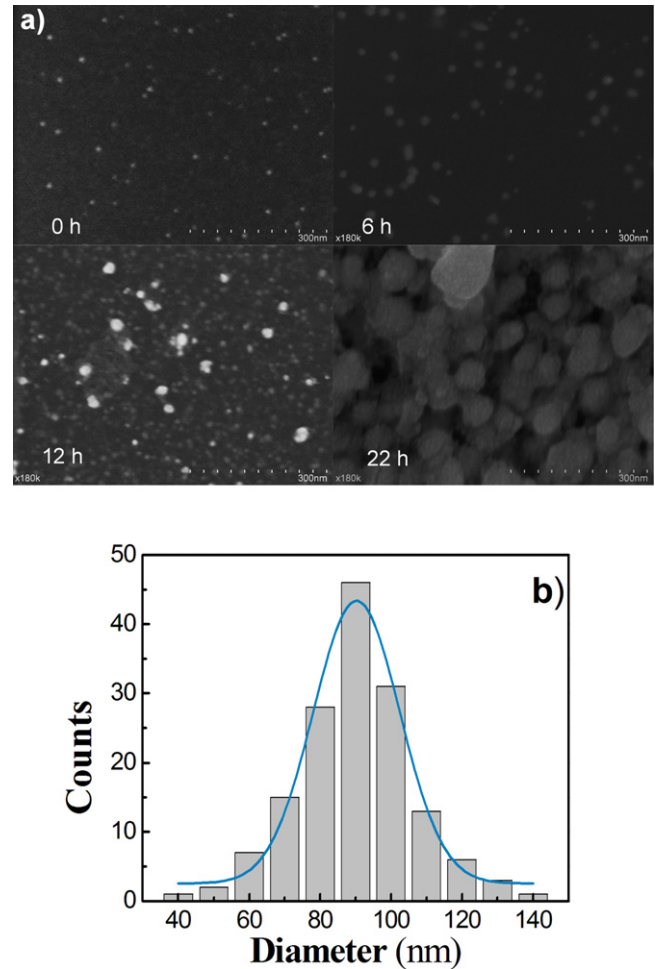
Figure 2. (a) SEM images of AuNPs obtained after different growing times. The initial *ff* was around $5 \cdot 10^{-4}$. (b) Histogram for the highest filling factor (22 h).

increase progressively with the immersion (growth) time (figures 2(a)–(c)) from 8 (initial nanocomposite) to 90 nm (practically completed Au layer), as estimated from their corresponding size histograms (figures 2(e)–(f)).

3.1. Transmission and reflectivity measurements

Optical properties of AuNP–Nv nanocomposites were carefully studied by analyzing after each growth step the transmission and reflectivity spectra of the films deposited on glass and silicon, respectively, in order to correlate with the morphology characterization shown above. Figure 3(a) plots the experimental absorbance spectra of a nanocomposite deposited on a 2.5 cm^2 glass substrate with an initial *ff* of $5 \cdot 10^{-4}$ and growth times between 1.5 and 64 h. The absorbance is negligible for short growth times (black curve), but it increases progressively with the growth time. It exhibits a maximum due to the LSPR phenomenon, which red-shifts with the size of the MNPs (controlled by the growing time) in accordance with other publications [2, 19, 20]. AuNP composite samples with $ff = 10^{-3}$ and $ff = 10^{-4}$ show similar curves. The symbols in figure 3(b) depict the reflectivity spectra measured for different growth times. Again, the

Figure 3. (a) Absorbance spectra of AuNP–Nv nanocomposite deposited on glass in a sample of 2.5 cm² for different growing times. (b) Reflectivity spectra of AuNP–Nv nanocomposite deposited on silicon in a sample of 1.5 cm² for different growing times. Symbols and red lines correspond to experimental data and simulations respectively. In both graphics the initial filling factor was $5 \cdot 10^{-4}$ (initial Au:Nv volume ratio was 0.1:1).

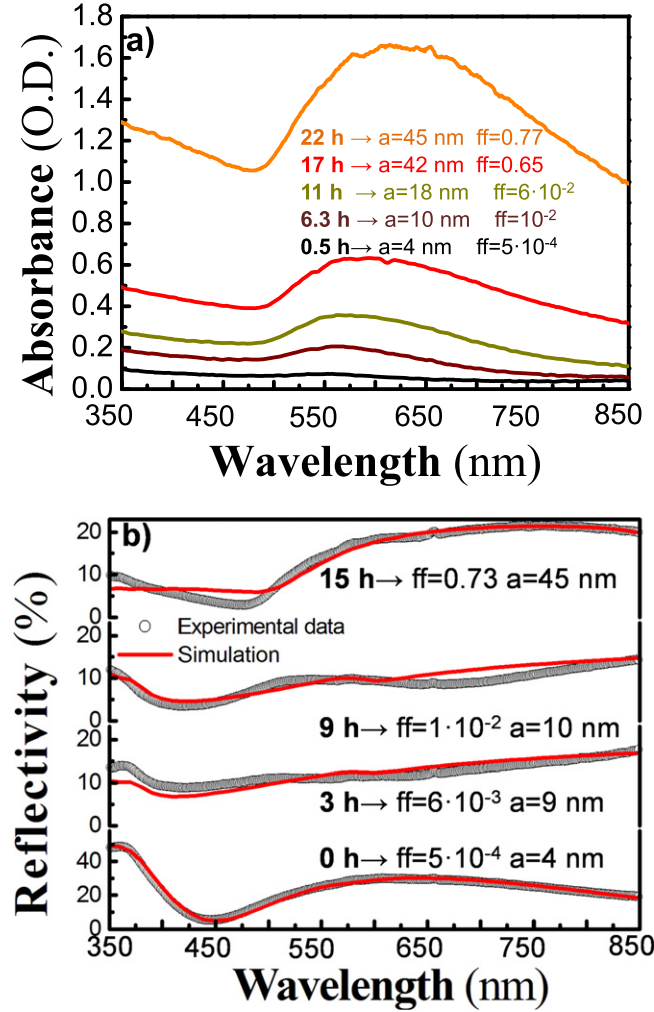influence of the MNP is negligible for small sizes and increases for bigger ones, and the curve reaches the behavior of a completed Au film for growing times longer than 15 h, as was observed before in figure 2.

3.2. Refractive index model

The refractive index of the MNP nanocomposite (n_{eff}) may be estimated with the use of the Maxwell–Garnett effective medium approximation [21]:

$$(n_{\text{eff}})^2 = \varepsilon_{\text{eff}} = \varepsilon_{\text{NV}}$$
$$\cdot \frac{L_i \cdot (\varepsilon_{\text{MNP}} - \varepsilon_{\text{NV}}) + \varepsilon_{\text{NV}} + ff \cdot (\varepsilon_{\text{MNP}} - \varepsilon_{\text{NV}}) \cdot (1 - L_i)}{L_i \cdot (\varepsilon_{\text{MNP}} - \varepsilon_{\text{NV}}) + \varepsilon_{\text{NV}} - ff \cdot (\varepsilon_{\text{MNP}} - \varepsilon_{\text{NV}}) \cdot L_i}$$
(1)

where ε_{NV}, ε_{MNP} *and* ε_{eff} are the dielectric constants of the surrounding medium (Nv), MNP and the nanocomposite, respectively. L_i refers to the depolarization factors along each

axis (1/3 in spherical shape) [2, 20]. The refractive index of the Nv resist has been experimentally obtained by fitting the reflectivity of Nv films of thicknesses between 0.5 and 2 μm on silicon substrates:

$$n_{\text{Nv}}(\lambda) = 1.6 + 65e^{-\lambda/47} + 0.29e^{-\lambda/400}$$
(2)

where λ is the wavelength in nm. The dielectric constant of MNP is approximated by taking into account the free and the bound electrons of the metal [18, 22–26]:

$$\varepsilon_{\text{MNP}} = \varepsilon_{\text{free}-e^-} + \varepsilon_{\text{bound}-e^-}$$
(3)

The first term is usually calculated by Drude's model and the second term by the expression proposed in [22, 23]:

$$\varepsilon_{\text{free}-e}(\omega) = 1 - \frac{\omega_p^2}{\omega^2 + i(\Gamma_{\text{bulk}} + C \cdot v_f/a) \cdot \omega}$$
(4)

$$\epsilon_{\text{bound}-e}(\omega) = Q_{\text{bulk}} \int_{\omega_g}^{\infty} \frac{\sqrt{x - \omega_g}}{x} \left[1 - F(x, E_F, T) \right]$$
$$\times \frac{\left(x^2 - \omega^2 + \gamma_b^2 - i2\omega\gamma_b\right)}{\left(x^2 - \omega^2 + \gamma_b^2\right)^2 + 4\omega^2\gamma_b^2} dx$$
(5)

where ω_p is the plasma frequency set to $13 \cdot 10^{15}$ Hz [22–24], Γ_{bulk} the bulk damping constant considered to be $1.1 \cdot 10^{14}$ Hz [24], v_f the electrons velocity at the Fermi surface (14.1 nm s^{-1}) [22], C a constant set to 1 [26], $F(x, EF, T)$ the Fermi energy distribution function at the temperature T and the Fermi energy $E_F = 2.5$ eV [21], E_g the energy gap of Au ($E_g = 2.1$ eV) [22], γ_b the damping constant in the intraband transitions ($2.4 \cdot 10^{14}$ Hz) and Q_{bulk} a proportionality factor ($Q_{\text{bulk}} = 2.3 \cdot 10^{24}$) [22]. Due to the fact that Au is an absorbing material, the dielectric constant of the MNP, as well as the dielectric constant of the effective medium (equation (1)), is a complex number. In this way, the experimental reflectivity of the nanocomposite deposited on silicon substrates can be approximately reproduced by choosing average values of *ff* and of the AuNPs radius, and hence deduce an approximate curve of n_{eff}. The red lines in figure 3(b) plot the results of such a fitting for different growing times. Clearly, the model reproduces quite well the experimental data, from which an approximated value for *ff* can be obtained, which is represented in figure 4 as a function of the growing time for the three initial concentrations studied here (initial *ff* of 10^{-3}, $5 \cdot 10^{-4}$ and 10^{-4}). Rather surprisingly, the results obtained within Maxwell–Garnett approximation give reasonable results even in the case of moderately big sizes of NPs (50–100 nm diameters). For high concentrations (*ff*'s > 0.5) Maxwell–Garnett is no longer used because the reflectivity of the film approximates to the one of bulk Au. The average size of AuNPs (right axis in figure 4) at each concentration was estimated from the experimental radius measured by SEM (around 45 nm from figure 2) when the maximum *ff* = 0.77 is reached by considering a perfectly compact layer of AuNPs. The size of the MNPs starts to increase slowly with the growing time until it overcomes a certain threshold where the regrowth accelerates. Then the size grows fast and reaches saturation when a complete Au
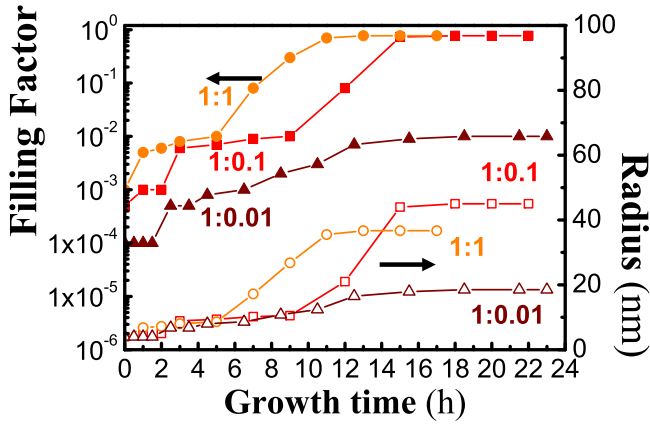
Figure 4. Filling factor (left axis and filled symbols) and radius deduced from the Maxwell–Garnett modeling as a function of the growth time. Orange, red and brown colors refer to an initial Nv/Au volume radius of 1:1, 1:0.1 and 1:0.01 respectively (*ff* of 10^{-3}, $5 \cdot 10^{-4}$, 10^{-4}).

film is formed. This threshold time decreases with the concentration, and it is probably related to the ease that the nanocomposite film incorporates neighboring Au atoms when there is a high amount of metal on its surface. Thus, the growth is slower at the beginning of the process due to the low quantity of MNPs presented in the nanocomposite. Nevertheless, once this threshold time is reached the growth accelerates because the surface is able to incorporate more metal atoms. Indeed, the regrowth saturates to a radius of around 20 nm for the lowest initial concentration used here (wine line) after 24 h without overcoming this threshold and hence to form a completed Au film. However, higher concentrations in the Nv (red and orange lines) show a faster growth and can provide a control of the size (diameter) between 10 nm, before the growing process, and 100 nm, when a complete Au film is reached (see figure 2). The size at which the complete Au layer is formed in the film decreases with the initial concentration (red line with respect to the orange one) due to the large amount of Au in the nanocomposite layer.

3.3. Absorption and scattering cross sections

Experimentally measured plasmonic resonance curves shown in figure 3(a) can be calculated on the basis of the Mie theory where the extinction (σ_{ext}), scattering (σ_{scat}) and absorption (σ_{abs}) cross sections can be calculated as follows [26]:

$$\sigma_{\text{ext}} = \frac{\lambda^2}{2 \cdot \pi \cdot n_{\text{m}}} \sum_{l=1}^{\infty} (2 \cdot l + 1) \cdot \left[\text{Im}\left(t_l^{\text{E}}\right) + \text{Im}\left(t_l^{\text{M}}\right) \right] \quad (6)$$

$$\sigma_{\text{scat}} = \frac{\lambda^2}{2 \cdot \pi \cdot n_{\text{m}}} \sum_{l=1}^{\infty} (2 \cdot l + 1) \cdot \left[\left|t_l^{\text{E}}\right|^2 + \left|t_l^{\text{M}}\right|^2 \right] \quad (7)$$

$$\sigma_{\text{abs}} = \sigma_{\text{ext}} - \sigma_{\text{scat}} \quad (8)$$

where n_{m} is the refractive index of the medium surrounding the MNPs, t_l^{E} and t_l^{M} the electric and magnetic scattering coefficients whose expressions can be found in [26]. The index l accounts for the contribution of the partial modes: $l = 1$ corresponds to the dipole mode, $l = 2$ to the

quadrupole, $l = 3$ to the octupole and so on. When small nanoparticles (diameter $\ll \lambda$) are considered only the electric dipole presents a significant contribution. However, when larger MNPs are considered high order terms need to be taken into account. Figure 5 plots absorption (red line), scattering (orange line) and extinction (wine line) cross sections calculated for MNPs with radius $a = 25$ nm (figure 5(a)) and $a = 45$ nm (figure 5(b)). The scattering cross section is negligible for small AuNPs, but it is significant when the MNP radius is 25 nm (figure 5(a)) and dominates in the extinction coefficient for a radius of 45 nm (figure 5(b)). This is due to the fact that scattering grows superlinearly with the size while absorption grows linearly (see equations (6)–(8)). These estimates are in agreement with others in the literature [25–29] and with published experimental data [2, 19, 20, 29]. In addition, our experimental absorbance data presented in figure 3(a) for different nanocomposites (different AuNP sizes) are in qualitative agreement with the Mie calculated extinction coefficients in figure 5. The main discrepancy arises for small MNPs where the experimental results exhibit wider LSPR and peaked at longer wavelengths as compared to the calculations. The longer wavelength in the experimental extinction LSPR peak can be explained by considering an ellipsoidal shape of the MNPs [25–28], also suggested from SEM measurements (figure 2) as well as of intuitive expectations from the fabrication method proposed, where the size of the MNP tends to grow asymmetrically along the substrate interface plane directions.

The broader linewidth measured in the experiment (figure 3(a)) as compared to the calculated data (figure 5) is attributed to the dispersion in the MNP size, which is about 10% of the average size, as deduced from the size histograms presented in figure 2. Nevertheless, this dispersion is helpful for scattering purposes since a broad wavelength bandwidth for light coupling into the waveguide will be attained. Figure 6 plots a bidimensional map of the scattering cross section as a function of the average NP radius and the scattering wavelength. In the case that AuNP size distribution is not included in the calculations, the bandwidth of the scattering resonance increases with the AuNP size for NPs with a radius larger than 35 nm (figure 6(a)). When the size dispersion (10% of the average size following SEM measurements) is included in the calculations (figure 6(b)), the effect of broadening with size starts even for very small NPs.

4. Waveguide characterization

4.1. Analysis of the waveguide

The waveguide studied in this work (depicted in figure 1) can be analyzed by dividing the problem into two different regions. The first one consists of a dielectric waveguide structure composed of four layers: air, PMMA, SiO$_2$ and Si. Since the refractive index of PMMA is larger than the one of SiO$_2$ (dot lines in figures 7(a)–(b)) this waveguide can support propagating modes at a certain wavelength if the thickness of the PMMA is sufficiently large. Dashed lines of figures 7(a)–
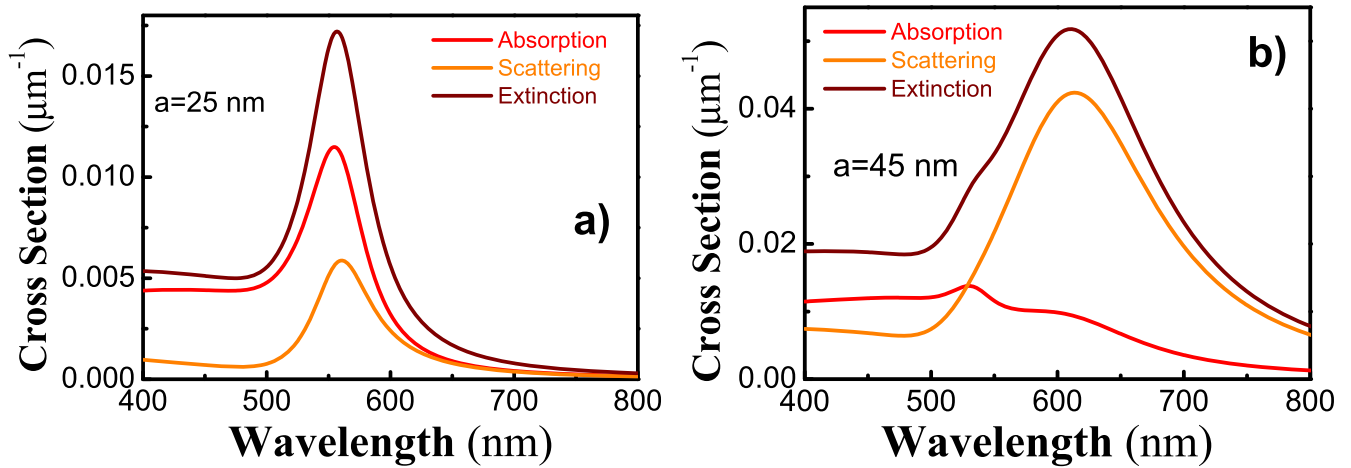
Figure 5. Extinction (wine), absorption (red) and scattering (orange) cross sections calculated from Mie theory for spherical AuNPs with 25 (a) and 45 nm (b) radii.
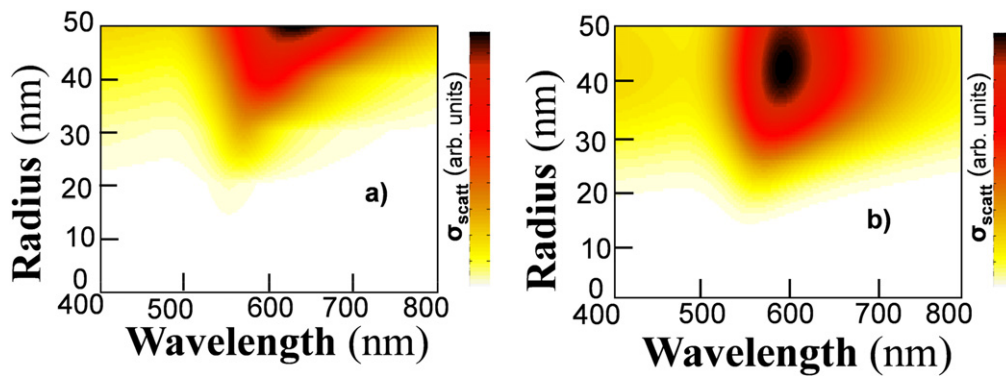
Figure 6. 2D plot of the scattering cross sections as a function of the NP size and scattering light wavelength. (a) Considering a size-dispersion-free NP size. (b) Taking into account a 10% dispersion of the NP size.
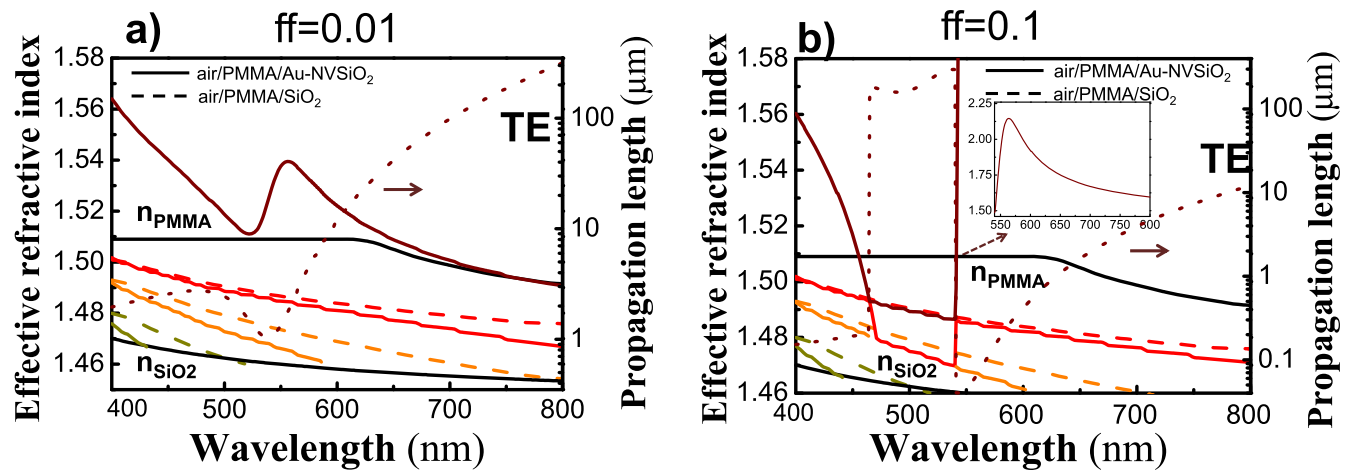
Figure 7. Effective refractive index propagating modes in the waveguides in TE polarization (TM show similar behaviour). Dashed and continuous lines refer to air/PMMA/SiO$_2$ and air/PMMA/AuNP–Nv/SiO$_2$ structures, respectively. Effective refractive indexes between PMMA and SiO$_2$ (indicated with black lines) are confined in the PMMA layer. Effective refractive indices longer than that of PMMA are confined in the nanocomposite, and their real and imaginary parts are depicted with wine lines in the right (continuous) and left (dot) axis, respectively. (a) *ff* = 0.01 (*a* ≈ 12 nm), (b) *ff* = 0.1 (*a* ≈ 25 nm).
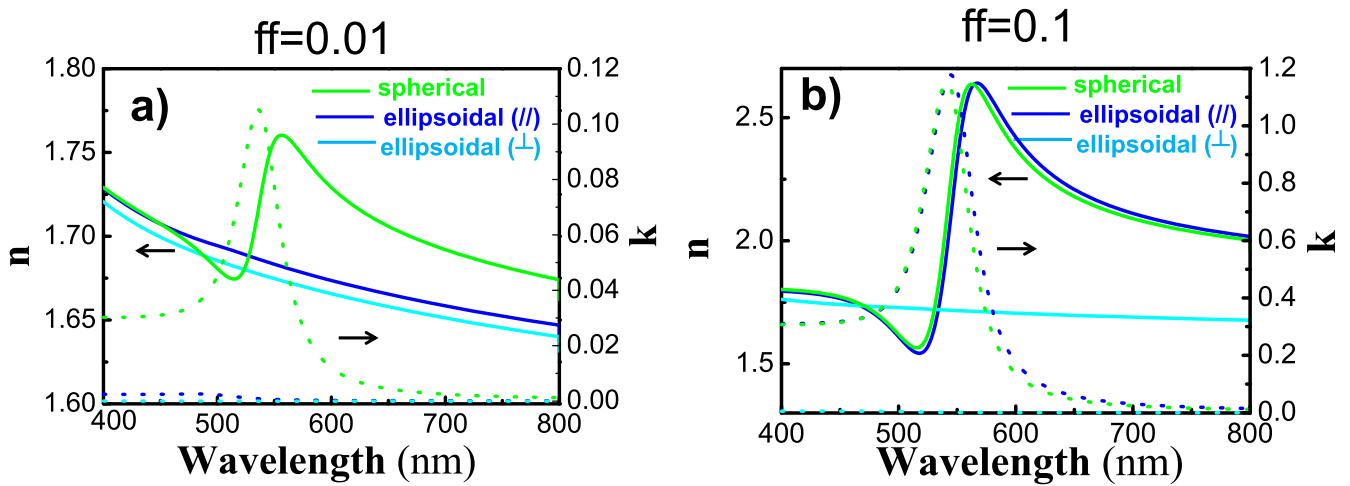
Figure 8. (a) Effective refractive index of the nanocomposite considering ellipsoidal shape of the nanoparticles (semiaxis a, a, a/3). Blue and cyan lines correspond to the axis parallel (TE) and perpendicular to the waveguide (TM). The spherical shape is plotted as a reference (green line). Left (continuous lines) and right (dotted lines) axes refer to real and imaginary parts, respectively. (a) $ff = 0.01$ ($a \approx 10$ nm), (b) $ff = 0.1$ ($a \approx 25$ nm).

(b) show the propagating modes in this structure in transverse electric (TE) polarizations (transverse magnetic, TM, shows similar results) calculated by the transfer matrix method [29] in the 400–800 nm range for PMMA and SiO$_2$ thicknesses of 2 μm. The second region includes a AuNP–Nv nanocomposite of 100 nm between the SiO$_2$ and the PMMA. Optical properties of this layer depend on the concentration, size and shape of AuNP in the Nv as has been discussed in the previous section. In this way, the n_{eff} of the nanocomposite can be enlarged in the plasmonic resonance region by an appropriate ff value selection (see figure 8), allowing the propagation of highly confined modes (plotted with wine lines in figure 7) in the nanocomposite, as has been deduced in [7]. The green lines in figures 8(a) and (b) plot the real (left axis and continuous line) and imaginary (right axis and dotted line) parts of the effective refractive index of the nanocomposite considering spherical nanoparticles with $ff = 0.01$ and $ff = 0.1$, respectively, calculated with a transfer matrix method [30]. The imaginary part shows a similar shape of the absorption cross section (shown in figure 5) with a maximum placed at the plasmonic resonance wavelength. As a consequence, the real part exhibits a particular shape with an inversion point at this wavelength due to Kramers–Kroning dependence, in accordance with this kind of nanocomposites [7, 31]. The TE$_0$ mode for $ff = 0.01$ (wine line in figure 7(a)) follows this particular shape of the n_{eff} and presents a short propagation length (dot line and right axis in figure 7(a)) due to the absorption of the MNPs. The TE polarization for $ff = 0.1$ (figure 7(b)) shows an anticrossing behavior with the TE$_0$ (wine) and TE$_1$ (red) modes around 500 nm. For shorter wavelengths the TE$_0$ represents the mode confined in the nanocomposite and the TE$_1$ the first order mode confined in the PMMA, while for longer wavelengths this assessment is inverted. Nevertheless, for wavelengths longer than 550 nm a new anticrossing is observed and again the TE$_0$ and TE$_1$ modes return to their initial representation. In the 500–550 nm wavelength range the TE$_0$ is strongly coupled to the

fundamental mode of the PMMA waveguide (red dash line), while the TE$_1$ mode is coupled for the wavelengths shorter than 500 nm and it is being decoupled for the wavelengths longer than 560 nm. This coupling is similar to the one observed with MNP chains [12, 13] and it can be used to enhance the launch of a high amount of light in the PMMA film. Then, the short propagation length of this mode (wine dotted line and right axis in figure 7(b)) doesn't present a limitation because this mode is used to couple light on the PMMA region, where light is propagated with low losses (red, orange and yellow continuous lines in figure 7). TM polarization exhibits a similar behavior for spherical shape of MNPs.

4.2. Coupling efficiency

The final target of the work was to couple normal incident light into the PMMA waveguide when AuNPs are integrated in the structure (figure 1). The requirement to couple light into a waveguide is to match the momentum of the incident light to one of the waveguides modes [29]. Evidently, this condition is initially not fulfilled for normal incident light because wave vectors of the incoming light and modes are completely mismatched. On the contrary, the scattering properties of MNPs redirect this light in all directions, and hence a certain portion will fulfill moment conservation and be coupled into the AuNP–Nv/PMMA waveguide structure (figure 1). Similar experiments have been carried out with layers of MNPs [8, 11], chains [12, 13] or antennas [9, 10] deposited on the top of a waveguide. However, in the present work MNPs are deposited in such a way that backward scattering provides a higher intensity of scattering than forward scattering [32]. In this way, waveguides fabricated as described in section 2.1 were characterized by focusing an incident laser beam onto the surface of the sample and directly measuring waveguided light at the output edge of the structure. Here, it is interesting to say that only in reference [11] was coupled
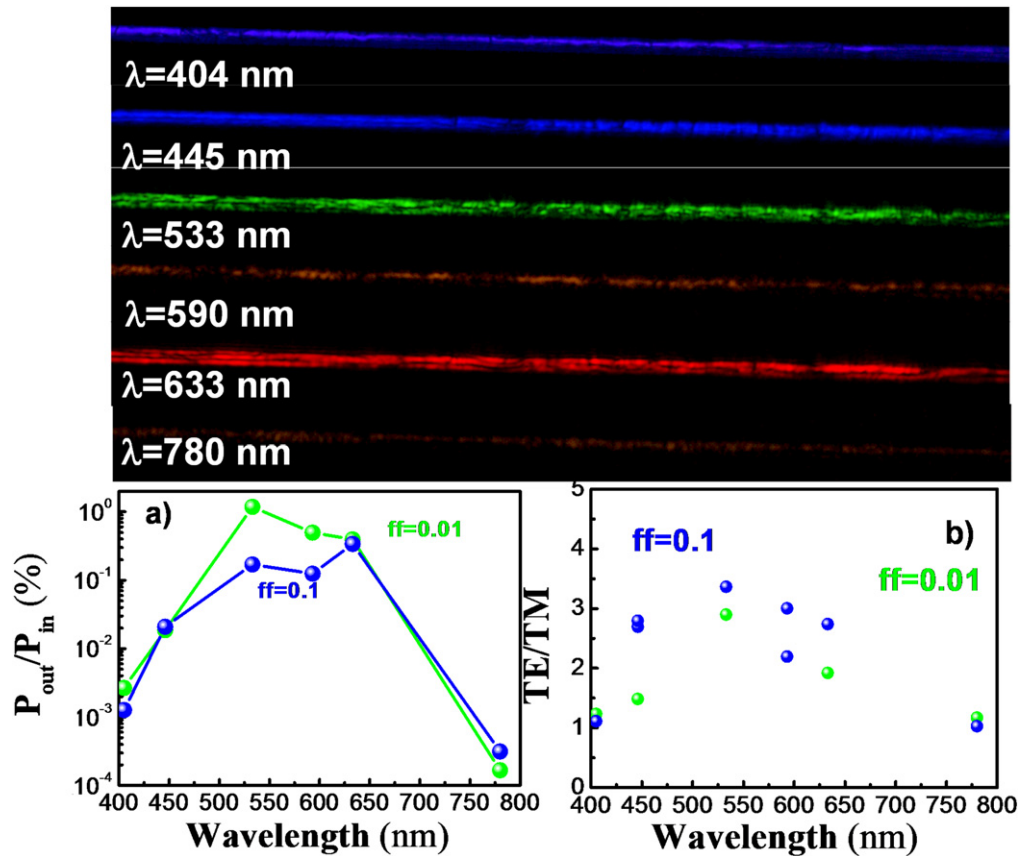
Figure 9. (a) Coupling efficiency at the output of the waveguide as a function of the incident light wavelength. (b) Ratio between TE and TM light at the output of the waveguide. Top panel: photographs of light coupled at different wavelengths. Filling factors were around 0.01 (radius 10 nm) and 0.1 (radius around 25 nm). These sizes were achieved with a growth time of 3 and 6 h, respectively.

light measured from the end face of the waveguide. Six different laser wavelengths (404, 450, 533, 590, 633 and 780 nm) were tested to corroborate the theoretical results. Figure 9(a) shows the coupling efficiency (ratio of the optical power density at the output to that at the input) where light was collected by a microscope objective in a sample with filling factors $ff = 0.01$ (green) and $ff = 0.1$ (blue), that corresponds to the estimated radius of the AuNPs of around 10–15 and 20–25 nm, respectively. Higher concentrations were not used to avoid the nanocomposite acting as complete continuous Au film. Light from such a broad range of wavelengths, 404–780 nm, is coupled into the structure (top panel of figure 9 shows a photograph of guided light collected at the output face of the waveguide). The efficiency is around 1% for wavelengths closer to the plasmonic resonance shown in figure 6(b) (550 nm for $ff = 0.01$ and 650 nm for $ff = 0.1$) and drops down to 0.01% for shorter and longer wavelengths (figure 9(a)).

For $ff = 0.1$, efficiency in the 500–560 nm region doesn't present a significant drop with respect to the maximum at the plasmonic resonance (650 nm), probably due to the strong coupling of the nanocomposite and PMMA modes studied in the last section. Indeed, for this concentration ($ff = 0.1$) the optical coupling is significantly better in TE than in TM polarization (a three-fold decrease in the 550–650 nm range

and about two-fold out of this range), while for $ff = 0.01$ the coupling does not show a strong dependence on the polarization (the decrease out of the maximum is between 1–2 times), as is shown in figure 9(b). This is due to the fact that the AuNPs are not perfectly spherical but ellipsoidal, generating optical birefringence that can increase the scattering and the confinement of the light in a particular direction. Figure 8 plots the real (left axis and continuous line) and imaginary (right axis and dotted line) parts of the n_{eff} of the nanocomposite containing MNPs with ellipsoidal shape. The blue and cyan lines refer to the n_{eff} in the plane (semiaxis a) and perpendicular to the plane (semiaxis a/3), respectively, while the green line refers to the case of the spherical shape (with no dependence on polarization). Clearly, the horizontal polarization (TE) demonstrates higher values for both the imaginary and real parts of the effective refractive index, in agreement with [7]. Indeed, the effective refractive index in vertical polarization (TM) for $ff < 0.01$ approximates to the one of Nv. Anisotropy increases strongly with the concentration, explaining the polarization dependence presented in figure 9. Moreover, the coupling also depends on the excitation polarization in a similar way (larger signal in TE than in TM), but with a smaller dependence on the wavelength. In the sample with $ff = 0.1$ the light scattered by TM excitation is about two to three times smaller with respect to

the TE excitation, while in the sample with *ff* = 0.01 the decrease is between one to two times. Again, this is due to the fact that the ellipsoidal shape of the MNPs induces a better scattering in TE rather than in TM polarizations, and this anisotropy increases with the size of the MNPs. In previous publications it was found as well selectivity in polarization in TE [12, 13] and TM [10], but due to the design of the dielectric waveguide and not to the MNPs' properties. Finally, it is worth mentioning that although the scattering efficiency significantly increases with the size of the MNP, here we obtain similar coupling efficiencies for the two sizes studied. This is probably because of higher roughness and ohmic losses (dotted line in figure 7) that are characteristics of the nanocomposite with larger AuNPs.

Maximum efficiencies obtained here (∼1%) are one order of magnitude smaller than the one obtained in [10] with a nanoantenna (10–20%), but here it is important to point out that our efficiencies are calculated measuring the light at the output face without taking into account Fresnel reflection at the end face or losses in the PMMA structure. The obtained efficiency in the worse case (∼1%) is of the same order of magnitude as the ones obtained by end-fire coupling techniques, but without the requirement of an accurate positioning of the incoming laser beam. Prism coupling or diffraction gratings achieve higher efficiencies (∼20%), but they are limited by the propagation derived from the operation wavelength and the incident angle. Therefore, the optical couplers described in the present work show a good efficiency and simple operation, together with a cheap and trouble-free fabrication process as compared with other coupling methods.

5. Conclusions

In this work Au nanoparticles were integrated into polymer waveguides by their *in situ* growth in Novolak photoresist, which is on-top-deposited and commercially available. The size of the AuNPs in the resist is carefully controlled by growing conditions in order to design the optical properties of the nanocomposite by two degrees of freedom (AuNP size and filling). Then, the nanocomposite is patterned inside a PMMA waveguide with the intention of exploiting the scattering properties to couple normal incident light to the PMMA film. Due to the elliptical shape of the MNPs the nanocomposite demonstrates birefringence in the plasmonic resonance spectral region. By choosing an appropriate concentration and TE polarization it is possible to obtain reasonably strong coupling efficiencies (about 1%) between the nanocomposite and PMMA fundamental modes in the spectral region where scattering is maximal. This coupling efficiency is of the same order of magnitude as the one obtained under end-fire coupling conditions. The present work is a step forward in the development of optical chips based on organic photonics technology on an Si-platform, but also in cheaper platforms using flexible substrates.

References

[1] Lal S, Link S and Halas N J 2007 *Nat. Photonics* **1** 641
[2] Mulvaney P 2001 *MRS Bull.* 1009
[3] Schuller J A, Barnard E S, Cai W, Chul Jun Y C, White J S and Brongersma M L 2010 *Nat. Mater.* **9** 193
[4] Akimov Y A, Koh W S and Ostrikov K 2009 *Opt. Express* **17** 10195
[5] Beck F J, Mokkapati S and Catchpole K R 2011 *Opt. Express* **19** 25230
[6] Maier S A, Kik P G, Atwater H A, Meltzer S, Harel E, Koel B E and Requicha A A G 2003 *Nature* **2** 229
[7] Otte M A, Estévez M C, Regatos D, Lechuga L M and Sepúlveda B 2011 *ACS Nano* **5** 9179
[8] Eurenius L, Hägglund, Olsson E, Kasemo B and Chakarov D 2008 *Nat. Photonics* **2** 360
[9] Aranjo F B, Kwadrin A and Koenderink A F 2012 *ACS Nano* **6** 101516
[10] Sidiropoulos T H P, Nielsen M P, Roschuk T R, Zayats A V, Maier S A and Oulton R F 2014 *ACS Photonics* **1** 912
[11] Pennanen A M and Toppari J J 2012 *Opt. Express* **21** A23
[12] Février M, Gogol P, Aassime A, Mégy R, Delacour C, Chelnokov A, Apuzzo A, Blaize S, Lourtioz J M and Dagens B 2012 *Nano. Lett.* **12** 1032
[13] Apuzzo A, Février M, Salas–Montiel R, Bruyant A, Chelnokov A, Lérondel G, Dagens B and Blaize S 2013 *Nano Lett.* **13** 1000
[14] Suárez I, Gordillo H, Abargues R, Albert S and Martínez-Pastor J P 2011 *Nanotechnology* **22** 435202
[15] Abargues R, Marqués-Hueso J, Canet-Ferrer J, Pedrueza E, Valdés J L, Jiménez E and Martínez-Pastor J P 2008 *Nanotechnology* **19** 355308
[16] Marqués-Hueso J, Abargues R, Valdés J L and Martínez-Pastor J P 2010 *J. Mater. Chem.* **20** 7436
[17] Abargues R, Martínez-Marco M L, Rodríguez-Cantó P J, Marqués-Hueso J and Martínez-Pastor J P 2013 *Proc. SPIE* **8682** 1
[18] Pedrueza E, Valdés J L, Chirvony V, Abargues R, Hernández-Saz J, Herrera M, Molina S I and Martínez-Pastor J P 2011 *Adv. Funct. Mater.* **21** 3502–7
[19] Huang X and El-Sayed M A 2010 *J. Adv. Res.* **1** 13
[20] Chen H, Kou X, Yang Z, Ni W and Wang J 2011 *Langmuir* **24** 5233
[21] Salski B and Celuch M 2012 *IEEE Trans. Microw. Theory* **60** 2352
[22] Scaffardi L B and Tocho J O 2006 *Nanotechnology* **17** 1309
[23] Inouye H, Tanaka K, Tanahashi and Hirao K 1998 *Phys. Rev. B* **57** 11334
[24] Johnson P B and Christy R W 1972 *Phys. Rev. B* **6** 4370
[25] Noguez C 2007 *J. Phys. Chem. C* **111** 3806
[26] Myroshnychenko V, Rodríguez-Fernández J, Pastoriza-Santos I, Funston A M, Novo C, Mulvaney P, Liz-Marzán L M and García de Abajo F J 2008 *Chem. Soc. Rev.* **37** 1792
[27] Ghosh S K and Pal T 2007 *Chem. Rev.* **107** 4797
[28] Jain P K, Lee K S, El-Sayed I H and El-Sayed M A 2006 *J. Phys. Chem. B* **110** 7238

[29] Rodríguez-Fernández J, Pérez-Juste J, García de Abajo J and Liz-Marzán L M 2006 *Langmuir* **22** 707–10

[30] Lifante G 2003 *Integrated Photonics: Fundamentals* (New York: Wiley)

[31] Kubo S, Diaz A, Tang Y, Mayer T S, Choon Khoo I and Mallouk T E 2007 *Nano Lett.* **7** 3418

[32] Beck F J, Verhagen E, Mokkapati S, Polman A and Cathpole K R 2011 *Opt. Express.* **19** A146

Purcell-enhancement of the radiative PL decay in perylenediimides by coupling with silver nanoparticles into waveguide modes

Mattia Signoretto, Nathalie Zink-Lorre, Juan P. Martínez-Pastor, Enrique Font-Sanchis, Vladimir S. Chirvony, Ángela Sastre-Santos, Fernando Fernández-Lázaro, and Isaac Suárez

Articles you may be interested in

Switchable polarization rotation of visible light using a plasmonic metasurface
APL Photonics **2**, 016103 (2016); 10.1063/1.4968840

Broadband convergence of acoustic energy with binary reflected phases on planar surface
Applied Physics Letters **109**, 243501 (2016); 10.1063/1.4971795

Tunable, omnidirectional structural color on reflection based on metal-SiO_X-metal structure
Applied Physics Letters **109**, 241104 (2016); 10.1063/1.4972240

Broadband optical magnetism in chiral metallic nanohole arrays by shadowing vapor deposition
Applied Physics Letters **109**, 251102 (2016); 10.1063/1.4972789

Sensing with toroidal metamaterial
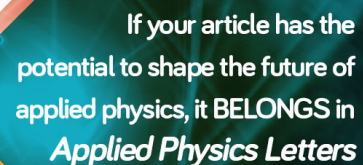Applied Physics Letters **110**, 121108 (2017); 10.1063/1.4978672

Broadband metamaterial for optical transparency and microwave absorption
Applied Physics Letters **110**, 143511 (2017); 10.1063/1.4979543

Purcell-enhancement of the radiative PL decay in perylenediimides by coupling with silver nanoparticles into waveguide modes

Mattia Signoretto,[1] Nathalie Zink-Lorre,[2] Juan P. Martínez-Pastor,[1] Enrique Font-Sanchis,[2] Vladimir S. Chirvony,[1] Ángela Sastre-Santos,[2] Fernando Fernández-Lázaro,[2] and Isaac Suárez[1,a)]

[1]UMDO, Instituto de Ciencia de los Materiales, Universidad de Valencia, 46071 Valencia, Spain
[2]Área de Química Orgánica, Instituto de Bioingeniería, Universidad Miguel Hernández de Elche, Avda. de la Universidad s/n, Elche 03202, Spain

In this work, an interesting approach to enhance the coupling between excitons and plasmons is proposed by integrating highly luminescent perylenediimides (PDIs) and Ag metal nanoparticles (MNPs) in the core of a multilayer dielectric waveguide. The combination of the weak plasmonic coupling and the high scattering of MNPs gives rise to a significant improvement of the PDI photoluminescence and Purcell factor (PF) in forward-scattering geometry. Furthermore, when the PDI-MNP system is used as the core of a multilayer waveguide, a Purcell factor enhancement larger than 10 is observed, which is explained by an increase in the exciton-plasmon coupling under the light confinement in the waveguiding structure as compared to a single layer of PDI emitters. *Published by AIP Publishing.* [http://dx.doi.org/10.1063/1.4999325]

The interaction of excitons with metal nanostructures has attracted significant interest in the last few years as a way to manipulate light at the nanoscale.[1] A coupled exciton-plasmon system may be obtained by means of a semiconductor nanostructure or organic molecule positioned in close proximity to a metal nanoparticle (MNP), and it is characterized by different optical properties than the individual components. In a weak coupling regime, the strong near field of the MNP increases the radiative rates or absorption cross section of the emitter,[2] and in a strong coupling interaction, the system should manifest a Rabi splitting between new quasiparticle states (exhibiting mixed exciton-plasmon character)[3] or plasmonic energy transfer between the plasmonic and exciton states.[4] Both weak and strong coupling regimes have been demonstrated by using an appropriate technology to deposit the active material at a few nanometers from the MNPs. Strategies developed up to now include scanning probe technology of individual emitters,[5,6] layer by layer assembly,[7–12] metal nanopatterns,[13–15] or coating a shell of emitters on the MNPs.[16–23] For these purposes, the exciton-plasmon interaction has been mostly analyzed in layers or individual nanoparticles by microscopy techniques (transmittance or backscattering). Meanwhile, the incorporation of an exciton-plasmon interacting system into a photonic device has been elusive although an enhancement of this interaction under high light confinement conditions has already been demonstrated.[10,11] In this paper, we propose the integration of an active material and MNPs into a common polymer waveguide in order to improve the coupling between both elements in the core of such a photonic structure and provide a direct extraction of light from its output edge.

For this purpose, we propose perylenediimides (PDIs)[24] as an active material to interact with plasmonic nanostructures. Organic compounds of this type possess outstanding properties for optoelectronics such as a high quantum yield (QY) emission at room temperature, high thermal and optical stabilities, and relatively high electron mobility.[25] Indeed, PDIs have been recently revealed as a potential gain media in both the monomer[26] and aggregated compounds.[27]

In the present work, we have analyzed the Purcell enhancement due to exciton-plasmon coupling in the system formed by PDI molecules embedded in a poly(methyl methacrylate) (PMMA) film, which is separated by an optimum distance of around 6.5 nm to a layer of Ag nanoparticles. For this distance, the (average) coupling between the emitters and MNPs resulted in a significant increase in the measured photoluminescence (PL) intensity. This enhancement is consistent with precedent works in the literature where organic compounds[6,7] or semiconductor nanocrystals[14] were used, and it is attributed to a shortening of the radiative exciton lifetime (e.g., the Purcell effect) and the additional far field emission produced by the high scattering of the metal nanoparticle. Moreover, in the present work, a more important enhancement of the exciton-plasmon coupling is measured at the output edge of the PMMA-PDI multilayer waveguide due to the noticeable confinement of the electromagnetic field in the core of the waveguide as compared to the case of a single PMMA-PDI layer. Our conclusions are corroborated by time resolved photoluminescence (TRPL) experiments in spite of the fact that the majority of works just provide a comparison of PL intensities. The kinetics of the PL light give us a direct estimate of the Purcell factor that was greater than 10 in the case of exciton-plasmon coupling inside the waveguide, while it was around 5 in the case of the single PMMA-PDI layer interacting with MNPs. Our approach provides a useful geometry to integrate the unique properties of the exciton-plasmon system in a full compact photonic device and can be easily extended to other kinds of active/plasmonic materials.

The PDI compound used in this work, o-(Ph$_2$PhO)$_4$PDI [chemical structure depicted in Fig. 1(a)], was synthetized

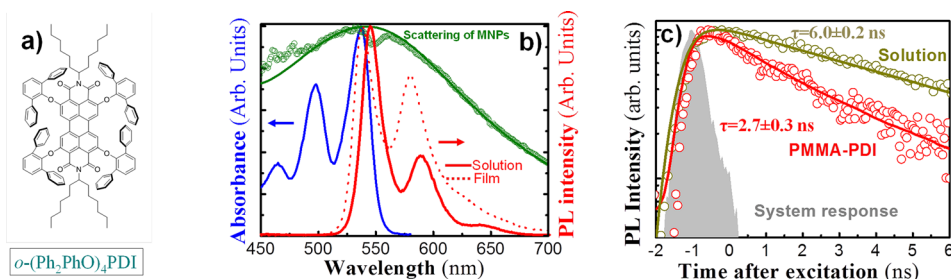a)Author to whom correspondence should be addressed: isaac.suarez@uv.es

FIG. 1. (a) Chemical structure of the o-(Ph$_2$PhO)$_4$PDI PDI used in this work. (b) Absorbance (blue continuous curve and left axis) and PL intensity (red continuous curve and right axis) of this molecule; the red dotted line corresponds to the PL spectrum of the PDI embedded in PMMA; the measured light scattering spectrum of the layer formed by Ag nanoparticles (green hollow circles) is in good agreement with the theoretical curve (green continuous line). (c) PL decay kinetics of the PDI in the colloidal solution (dark yellow symbols) at 590 nm and the PMMA-PDI film (red symbols) at 580 nm and exponential decay fitting (continuous dark yellow and red continuous lines); the gray shaded area corresponds to the system time response.

following the procedure explained elsewhere.[26] The o-(Ph$_2$PhO)$_4$PDI presents four bulky triphenylphenoxy groups in the ortho position and exhibits not only a high quantum yield (QY) of emission (>90%) at room temperature but also good thermal and optical stabilities, and we have recently exploited to demonstrate optical amplification.[26] The PDI was dispersed in the PMMA by mixing toluene solutions of PDI and PMMA. The resulting PMMA-PDI solution is then spin coated on glass (forward-scattering experiments) and Si-SiO$_2$ (waveguides) substrates and baked at 80 °C and 150 °C for two minutes at each temperature. Commercial silver colloidal nanoparticles were supplied by NanoComposix and consisted of Ag nanospheres of 100 nm in diameter capped with poly(vinylpyridine) (PVP) organic ligands and diluted in water at 0.02 mg/ml. The UV-VIS absorption spectrum of the colloidal solution was measured with a commercial Shimadzu UV-2501PC spectrophotometer. The PL spectra of the colloidal solution and solid thin films were excited by using a continuous wave 450 nm laser diode module and analyzed with an HR4000 Ocean Optics spectrograph. Time Resolved PL (TRPL) experiments on liquid solutions, single thin films, and multilayer waveguide structures were carried out by means of a Nd:Yag laser doubled at 532 nm (20 kHz, 1 ns, average power of around 3 mW) as an excitation source and a Hamamatsu C5658-3769 avalanche photodetector connected to a BOXCAR PCS-150 electronics from Becker & Hickl GmbH to analyze the PL transients. The particular geometry details for laser excitation and PL collection in the case of the PMMA-PDI films and optical waveguides are described and illustrated below. All measurements were performed at room temperature.

The UV-VIS absorption spectrum of the o-(Ph$_2$PhO)$_4$PDI compound diluted in toluene shows a characteristic vibronic structure with four peaks at 535, 498, 464, and 421 nm (the last one not shown), corresponding to the 0-0, 0-1, 0-2, and 0-3 transitions in the absorption spectrum [blue curve in Fig. 1(b)].[26] The PL exhibits a mirror-spectrum of absorption with peaks at 545, 590, and 641 nm [red curve in Fig. 1(a)]. The PDI embedded into the PMMA film deposited on glass exhibits a 10 nm blue-shift in both absorption (not shown) and PL (dotted red curve) spectra, when compared to PDI in solution. Furthermore, no modification of the PL spectrum shape is observed, and hence, we believe that there are no significant PDI aggregation effects in the film, which could seriously affect the emission efficiency. Indeed, the QY in the film

measured with a commercial system (Hamamatsu C9920-02) remained very high 30.6%, indicating a minimization of non-radiative decay channels when the PDI is incorporated in the PMMA-PDI solid thin film. This QY is consistent with decay times deduced from TRPL spectra registered at 580 nm [Fig. 1(c)], which demonstrates a faster PL transient in the film (red symbols) than in the solution (dark yellow symbols). In both cases, the PL transients can be fitted with single exponential decay functions [solid lines in Fig. 1(c)] whose best fitting decay times were 6.0 ± 0.2 ns and 2.7 ± 0.2 ns for the solution and film, respectively. This reduction in the decay time can be attributed to some nonradiative channel present in the PMMA-PDI film that was absent or negligible in solution. The effective recombination decay time (τ_{eff}) deduced from TRPL is the combination of radiative (τ_r) and nonradiative (τ_{nr}) contributions $1/\tau_{eff} = 1/\tau_r + 1/\tau_{nr}$. If τ_r is assumed to be close to that of the solution (6 ns), τ_{nr} would be around 5 ns. From these values, a QY $= \tau_{nr}/(\tau_{nr} + \tau_r) \approx 45\%$ can be estimated for the film, which is very close to the QY measured with the commercial system.

The interaction of the PDI with MNPs has been firstly studied in the multilayer structure schematically illustrated in Fig. 2(a). First, a low concentrated (0.06 wt. %) PMMA-PDI nanocomposite thin film of 50 nm was deposited on a glass substrate using the procedure explained below. Then, before depositing the Ag MNPs, an intermediate layer of the commercially available polymer electrolyte Omnicoat (Microchem Corporation) was spin coated on the top of the nanocomposite and baked at 180 °C for 1 min. This layer was included for several purposes. The most direct ones regard the adhesion of MNPs to the substrate (Omnicoat is commonly used as a linker for the commercially available resist SU-8) and the promotion of their homogenous dispersion on the substrate. In fact, layer by layer assemblies of metal nanoparticles using polymer electrolytes have been already reported in the literature.[28] In this way, MNPs dispersed in H$_2$O (20 µg/ml) were dropped on the substrate surface that was treated with Omnicoat and baked at a controlled temperature of 50 °C for 30 min with the intention to prevent aggregation of MNPs in the process of solvent evaporation. A filling factor (the ratio of the surface occupied by MNPs to the whole surface) of around 10% with a reasonably good dispersion of MNPs onto the sample surface was achieved by repeating this process sequentially one more time; the aspect of the layer can be observed by SEM
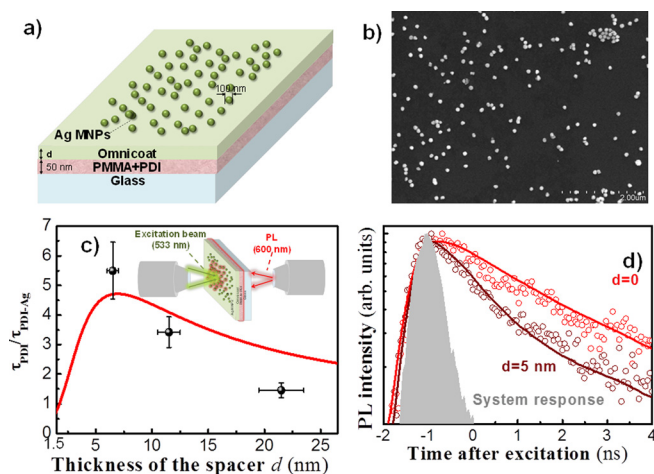
FIG. 2. (a) Multilayer structure to study the interaction between o-(Ph$_2$PhO)$_4$PDI and MNPs. (b) SEM image of a small zone of the surface sample where Ag nanoparticles were dropped. (c) Experimental (symbols with error bars) and theoretical (red curve) dependences of the Purcell factor as a function of a distance between a molecule and MNP surface. Experimentally, the Purcell factor was calculated as a ratio of the PL radiative lifetime measured in the absence of MNPs to that measured in their presence. Theoretically, we calculated the gain in the radiative recombination rate following the model proposed in Ref. 9. (d) TRPL measured spectra at 580 nm without (red symbols) and with (brown symbols) MNPs, in this case measured by using a spacer of d = 5 nm; solid lines correspond to exponential decay fitting curves; the gray shaded area corresponds to the temporal response of the system.

[Fig. 2(b)]. Then, the design of the experiment is such that the thin PMMA layer containing randomly distributed PDI molecules at a very low concentration is separated from a relatively high concentrated MNP layer (10% of the surface occupied by Ag nanoparticles) by the Omnicoat spacer plus 1.5 nm corresponding to the length of the MNP surface ligands, referred to as distance d. In these conditions, most of the PDI molecules should be at a sufficiently short distance from a neighbour MNP, and hence the emitter-plasmon coupling must be measurable. In addition, the size of the region occupied by MNPs was around 0.5 cm^2, three times smaller than that of the PMMA-PDI film sample ($\sim$1.5 cm^2); in this way, two distinguishable regions, with and without MNPs, were defined by our fabrication procedure for studying the influence of MNPs on the emission of PDI molecules referred to the region without nanoparticles. Here, it is worth mentioning that spherical MNPs of Ag 100 nm in diameter were chosen as good light scattering nanostructures whose localized surface plasmon resonance should overlap the PL spectrum of the PDI compound, as calculated by the Mie theory[29] [green solid line in Fig. 1(a)]. Experimentally, the measured light scattering spectrum [green symbols in Fig. 1(a)] nicely agrees with the theoretically calculated curves, thus corroborating the good homogeneity of MPNs dispersed on the substrate surface by the above described deposition method.

Another important mission of the Omnicoat layer (+ the MNP ligand length = 1.5 nm) is to provide the appropriate dielectric spacer d to optimize the electromagnetic coupling between the metal nanoparticle and the emitter (i.e., the exciton-plasmon coupling), because for d lower than the optimal value, the emitter would begin to quench by non-radiative ohmic losses in the metal.[9] For some finite optimum d, the non-radiative quenching is absent and the

reduction of the emitter radiative lifetime begins due to exciton-plasmon coupling that gives rise to an increase in the PL intensity and a maximum Purcell factor, as it has been found both theoretically[9] and experimentally.[6,7,9,14] We calculated the effect of MNPs on the recombination rate of molecules as a function of d with the model proposed in Ref. 9 [red curve in Fig. 2(c)]. To assess the Purcell factor experimentally, we measured both PL intensities (not shown here, but commented below) and PL lifetimes of molecules subjected and not subjected to plasmonic interaction with MNPs.

PL and TRPL measurements of the PMMA-PDI without/with a layer of MNPs separated by the Omnicoat-spacer were carried out in a forward-scattering configuration [see the illustration as an inset in Fig. 2(c)] using an excitation power density of about 100 W/cm^2. Such forward- or back-scattering geometries are commonly used to characterize the enhancement of the PL signal from different emitters by metal nanostructures.[6,7,9,10,14,17] The geometry allows us to study the influence of MNPs on the light emitting by PDI molecules by selecting the illuminated region on the surface of the sample (without or with MNPs on top of the PMMA-PDI film). It is worth mentioning that PL and TRPL spectra recorded at five different positions on the sample surface with MNPs were very similar; hence, we do not find any influence of the local inhomogeneity on the spatial distribution of MNPs observed in Fig. 2(b) when averaged over the excitation area defined by a laser spot of around 60 μm in diameter.

In the case of our steady-state PL measurements, we found that the PL intensity experiences a 4–5 fold enhancement for intermediate thicknesses (d = 5–10 nm, data not shown), in agreement with previous results found with organic compounds[6,7] or semiconductor nanocrystals.[14] This enhancement can be explained by the influence of scattering mechanisms or a modification of the radiative spontaneous emission rate.[7] Although the high scattering cross section of the Ag MNPs (3×10^{-10} cm^2 at 620 nm) is expected to provide some contribution to the experimental PL enhancement,[7,11,15] the dependence of PL intensity with the thickness of the spacer layer should be mainly attributed to a modification of the radiative recombination rate, i.e., to the Purcell effect.[30]

As our TRPL measurements show, the PMMA-PDI film separated from MNPs with an Omnicoat layer with a distance of 5 nm (d = 6.5 nm) is characterized by two-exponential decay components [see brown symbols in Fig. 2(d)]. The faster PL decay component with the lifetime of as short as 0.8 ± 0.1 ns is associated with the Purcell-reduced exciton lifetime produced by the exciton-plasmon coupling, whereas the slower decay component with the lifetime of around 3 ns is explained by a remaining portion of organic molecules which are located far from MPNs. These shorter and longer decay components have relative amplitudes of around 70% and 30% in favor of the former, that enables us to measure the shorter component in TRPL with sufficiently high accuracy. If we suggest that the nonradiative recombination time for PDI molecules in the layer is the same as in the case of solution, 5 ns (see above), then the radiative lifetime for PDI molecules in the layer with MNPs is τ_{r1}

≈ 0.95 ns. Similarly, we can obtain that the experimentally measured PL decay time of 2.7 ± 0.3 ns in the PMMA-PDI films without MNPs [red data symbols and the corresponding exponential curve fit in Fig. 2(d)] corresponds to $\tau_{r2} = 6$ ns. In the case of weak coupling of an emitter with a localized surface plasmon resonance, the gain in the spontaneous emission rate (or Purcell Factor) can be calculated as the τ_{r2}/τ_{r1} ratio. Indeed, we have measured the τ_{r2}/τ_{r1} ratio at several distances d [at 6.5, 11.5, and 21.5 nm, see symbols in Fig. 2(c)] and found that the maximum value takes place for $d = 6.5$ nm. It is worth noting that two more experimental points were obtained for $d = 1.5$ and 4 nm where the τ_{r2}/τ_{r1} ratio was about 1.0. However, we did not include these points in Fig. 2(c) because in these cases, the PL decay belongs to molecules non-interacting with MNPs, the others being quenched.

If we suggest that the Purcell effect influences only the rate of the radiative decay, for the optimum thickness of $d = 6.5$ nm [Fig. 2(c)], the Purcell factor, PF $= \tau_{r2}/\tau_{r1}$ r $= 5.5$. If it would influence both radiative and nonradiative decay rates, in this case, PF $= \tau_2/_{r1}$ r $= 3.4$.[31] The first hypothesis is more plausible, given that PF $= 5.5$ is very close to the measured intensity enhancement (4–5) and to the theoretical prediction for PF obtained by using the model proposed in Ref. 9 [red curve in Fig. 2(c)].

The multilayer waveguides were fabricated on a commercial SiO$_2$ (2 μm)/Si wafer (Active Business Company GmbH) by capping the PMMA-PDI/Omnicoat/MNPs structure with a 700 nm thick PMMA layer, as illustrated in Fig. 3(a). These optical waveguides confine a propagating mode in both TE and TM polarization at 620 nm in the PMMA-PDI/Omnicoat/MNPs active multilayer [see Fig. 3(b)], as predicted by a transfer matrix algorithm.[32] In these simulations, Ag MNPs were calculated by Drude's model and the effective refractive index of the MNPs surrounded by PMMA was found to be $1.9329 - 0.0046i$ by a Maxwell Garnett approximation.[28]

The waveguide was examined by focusing the excitation laser beam at 532 nm into a line 1 mm × 100 μm (power density of about 3 W/cm^2) on the top of the sample and collecting the waveguided PL with a microscope objective [see inset in Fig. 3(c)] or Variable Stripe Line (VSL) method.[33] In these conditions, a uniform laser excitation at 532 nm is guaranteed along the whole length of the waveguide and the PL remains confined in the waveguide core until decoupled from the exit face of the structure. Thus, PL spectra [Fig. 3(c)] measured at the output edge of the sample show the characteristic spectra of PDIs in the presence (brown line) or absence (red line) of MNPs. Again, although there is no change in the shape of the PL spectra, their maximum (or integrated) intensity was enhanced by a factor 5, approximately. However, in the waveguide configuration, the PL intensity is influenced not only by exciton-plasmon effect but also by the propagation of light along the whole length of the waveguide. In this way, although PL is uniformly generated along the entire length of the excitation line by this set-up, the losses introduced by the MNPs reduce the intensity of light measured at the output edge of the sample. Then, the fact that the intensity enhancement is close to that found by forward-scattering geometry (not limited by losses)
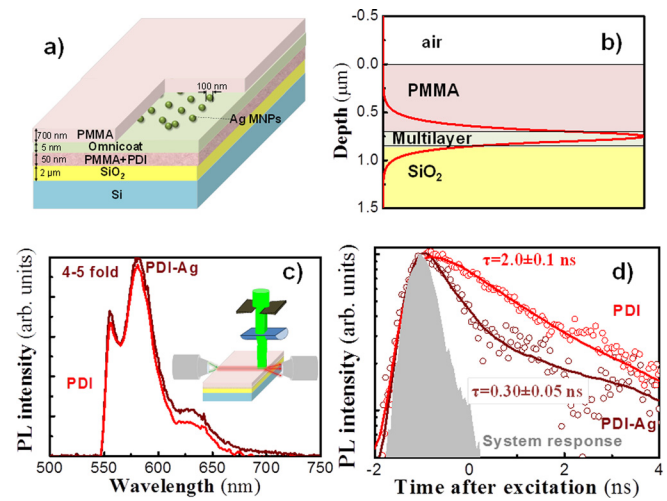

FIG. 3. (a) Structure of the multilayer optical waveguide. (b) TE$_0$ mode allowed in the structure calculated by a multilayer algorithm. (c) PL intensity measured at the edge of the waveguide with (wine) and without MNPs (red); the inset shows the experimental set-ups [end fire coupling and variable stripe line (VSL) method] used to characterize the waveguide. (d) TRPL spectra recorded at 580 nm and measured at the edge of the waveguide with the PMMA-PDI without (red) and with (brown) top layer of Ag MNPs separated by Omnicoat (5 nm); data symbols correspond to the experimental data and solid lines to the exponential fitting, with the gray shaded area being the system response.

discussed above indicates that exciton-plasmon feedback overcomes the additional attenuation in the structure. Furthermore, TRPL experiments in Fig. 3(d) reveal a stronger exciton-plasmon coupling as compared to that found with the transmission forward-scattering geometry [Fig. 2(d)]. Experimental kinetics in the presence of MNPs [brown symbols in Fig. 3(d)] needs to be fitted (brown solid line) with a shorter decay time of 0.30 ± 0.05 ns, while the region without MNPs presented a decay time of around 2.00 ± 0.10 ns [red symbols and solid line in Fig. 3(d)], close to the previous measurements in PMMA-PDI films under forward-scattering geometry, but slightly reduced by the light confinement in the waveguide.[34] Again, these decays correspond to radiative exciton lifetimes $\tau_r = 0.32$ ns and $\tau_r = 3.4$ ns with and without MNPs, respectively, by taking into account the nonradiative recombination $\tau_{nr} = 5$ ns. Let us note that the experiment without MNPs was carried out by end fire coupling the excitation laser at the input edge of the waveguide [see inset in Fig. 3(c)] in order to increase the signal to noise ratio to perform TRPL measurements properly in waveguides filled with low density emitters.[35] Nevertheless, since the experimental conditions for TRPL are far away from the threshold of stimulated emission, we believe that decay times should be the same in both geometries, VSL and end-fire coupling. In fact, to reach the Amplification of the Stimulated Emission (ASE) threshold, we needed to increase the laser excitation fluency and the concentration of the PDI compound in PMMA up to 1 μJ and 5 wt. %, respectively.[26] Therefore, the exciton-plasmon coupling in the waveguide geometry leads to a Purcell factor as high as 10.5, i.e., a factor two larger than that obtained in forward-scattering geometry [Fig. 2(c)]. Although previous experimental works dealt mostly in PL signal enhancement rather than the Purcell effect, theoretical predictions agree quite well with our

results. For example, calculations in similar systems, such as Au (Ag) nanoparticles of 80 (100) nm in diameter[36,37] (9) yielded a Purcell factor of around 4–5 (7), very close to our result found in forward-scattering geometry. Therefore, the further enhancement of the Purcell effect in the waveguide geometry can be attributed to the high confinement of the light in the core of the waveguide, as it has been proposed in metal-insulator-metal structures,[11] which demonstrates the benefit of the proposed waveguide geometry not only to study the photon-plasmon interaction but also to exploit it in integrated photonic devices.

In conclusion, the exciton-plasmon interaction is significantly enhanced by incorporating the organic PDI compound and Ag MNPs in the core of a planar multilayer waveguide. By combining experimental measurements and modeling, the waveguide structure was properly engineered in order to maximize the coupling between the active and plasmonic materials and to allow the propagation of light. The relatively high confinement of light in the core of the waveguide led to a stronger exciton-plasmon coupling as compared to the vacuum-coupled system. This was reflected by a Purcell factor as high as 10.5, around 2 times larger than that characterized by transmission forward-scattering geometry. This interesting approach can be extended to other kinds of active materials or metal nanostructures and hence provide a different approach to study the coupling between optical emitters and plasmonic nanostructures.

[1]M. Acchermann, J. Phys. Chem. Lett. **1**, 2837–2843 (2010).
[2]K. Q. Le, Plasmonics **10**, 475–482 (2015).
[3]P. Törma and W. L. Barnes, Rep. Prog. Phys. **78**, 013901 (2015).
[4]H. Chen, L. Shao, K. C. Woo, J. Wang, and H. Q. Lin, J. Phys. Chem. C **116**, 14088–14095 (2012).
[5]S. Kühn, U. Häkanson, L. Rogobete, and V. Sandoghdar, Phys. Rev. Lett. **97**, 017402 (2006).
[6]P. Bharadwaj and L. Novotny, Opt. Express **15**, 14266–14274 (2007).
[7]F. Tam, G. P. Goodrich, B. R. Johnson, and N. Halas, Nano Lett. **7**, 496–501 (2007).
[8]D. E. Gómez, K. C. Vernon, P. Mulvaney, and T. J. Davis, Nano Lett. **10**, 274–278 (2010).
[9]D. V. Guzatov, S. V. Vaschenko, V. V. Stankevich, A. Y. Lunevich, Y. F. Glukhov, and S. V. Gaponenko, J. Phys. Chem. C **116**, 10723–10733 (2012).
[10]A. V. Sorokin, A. A. Zabolotskii, N. V. Pereverzev, I. I. Bespalova, S. L. Yefimova, Y. V. Malyukin, and A. I. Plekhanov, J. Phys. Chem. C **119**, 2743–2751 (2015).
[11]G. M. Akselrod, C. Argyropoulos, T. B. Hoang, C. Ciraci, C. Fang, J. Huang, D. R. Smith, and M. H. Mikkelsen, Nat. Photonics **8**, 835–840 (2014).
[12]T. B. Hoang, G. M. Akselrod, C. Argyropoulos, J. Huang, D. R. Smith, and M. H. Mikkelsen, Nat. Commun. **6**, 7788 (2015).
[13]J. H. Song, T. Atay, S. Shi, H. Urabe, and A. V. Nurmikko, Nano Lett. **5**, 1557–1561 (2005).
[14]L. Shi, T. K. Hakala, H. T. Rekola, J. P. Martiaken, R. J. Moerland, and P. Törmä, Phys. Rev. Lett. **112**, 153002 (2014).
[15]P. F. Guo, S. Wu, Q. J. Ren, J. Lu, Z. Chen, S. J. Xiao, and Y. Y. Zhu, J. Phys. Chem. Lett. **1**, 315–318 (2010).
[16]R. Bardhan, N. K. Grady, J. R. Cole, A. Joshi, and N. J. Halas, ACS Nano **3**, 744–752 (2009).
[17]K. L. Gurunatha and E. Dujardin, J. Phys. Chem. C **117**, 3489–3496 (2013).
[18]A. V. Sorokin, A. A. Zabolotskii, N. V. Perverzev, S. L. Yefimova, Y. V. Malyukin, and A. I. Plekhanov, J. Phys. Chem. C **118**, 7599–7605 (2014).
[19]G. Zengin, G. Johansson, P. Johansson, T. J. Antosiewicz, M. Käll, and T. Shegai, Sci. Rep. **3**, 3074 (2013).
[20]A. M. Fales, S. J. Norton, B. M. Crawford, B. G. DeLacy, and T. Vo-Dinh, Phys. Chem. Chem. Phys. **17**, 24931–24936 (2015).
[21]B. G. DeLacy, O. D. Miller, C. W. Hsu, Z. Zander, S. Lacey, R. Yagloski, A. W. Fountain, E. Valdes, E. Anquillare, M. Soljacic, S. G. Johnson, and J. D. Joannopoulos, Nano Lett. **15**, 2588–2593 (2015).
[22]D. Melniakau, R. Esteban, D. Savateeva, A. Sánchez-Iglesias, M. Grzelczak, M. K. Schmidt, L. M. Liz-Marzán, J. Aizpurua, and Y. P. Rakovich, J. Phys. Chem. Lett. **7**, 354–362 (2016).
[23]B. L. Darby, B. Auguié, M. Meyer, A. E. Pantoja, and E. C. Le Ru, Nat. Photonics **10**, 40–45 (2016).
[24]T. M. Figueira-Duarte and K. Mullen, Chem. Rev. **111**, 7260–7314 (2011).
[25]C. Huang, S. Barlow, and S. R. Marder, J. Org. Chem. **76**, 2386–2407 (2011).
[26]M. Signoretto, N. Zink-Lorre, I. Suárez, E. Font-Sanchis, A. Sastre-Santos, V. S. Chirvony, F. Fernández-Lázaro, and J. P. Martínez-Pastor, ACS Photonics **4**, 114–120 (2017).
[27]Z. Yu, Y. Wu, Q. Liao, H. Zhang, S. Bai, H. Li, Z. Xu, C. Sun, X. Wang, J. Yao, and H. Fu, J. Am. Chem. Soc. **137**, 15105–15111 (2015).
[28]T. Placido, E. Fanizza, P. Cosma, M. Striccoli, M. L. Curri, R. Comparelli, and A. Agostiano, Langmuir **30**, 2608–2618 (2014).
[29]M. Signoretto, I. Suárez, V. S. Chirvony, R. Abargues, P. J. Rodríguez-Cantó, and J. P. Martínez-Pastor, Nanotechnology **26**, 475201 (2015).
[30]E. M. Purcell, Phys. Rev. **69**, 681 (1946).
[31]G. Colas des Francs, S. Derom, R. Vincent, A. Bouhelier, and A. Dereux, Int. J. Opt. **2012**, 175162.
[32]G. Lifante, *Integrated Photonics. Fundamentals* (John Wiley and Sons, 2003).
[33]H. Gordillo, I. Suárez, R. Abargues, P. J. Rodríguez-Cantó, and J. P. Martínez-Pastor, IEEE Photonics J. **5**, 2201412 (2013).
[34]C. Creatore, L. Claudio Andreani, M. Miritello, R. Lo Savio, and F. Priolo, Appl. Phys. Lett. **94**, 103112 (2009).
[35]I. Suárez, H. Gordillo, R. Abargues, S. Albert, and J. P. Martínez-Pastor, Nanotechnology **22**, 435202 (2011).
[36]P. Anger, P. Bharadwaj, and L. Novotny, Phys. Rev. Lett. **96**, 113002 (2006).
[37]T. V. Shahbazyan, Nano Lett. **13**, 194–198 (2013).

Europass Curriculum Vitae

Personal information

Surname(s) / First name(s)	**Signoretto Mattia**
Address(es)	Via della libertà, 32 F - 37135 Cadidavid (VR)- Italy
Telephone(s)	+34 633125564 / +39 3495854831
Email(s)	signoretto88@hotmail.it
Nationality(-ies)	Italian
Date of birth	18 Dicembre 1988 - Verona
Gender	Male

Work Experiences

Dates (from-to)	December 2012 - February 2013
Name and address of employer	**Hikari s.r.l.** Via Macello 37121 Verona
Business	Production of illumination system with LED.
Occupation	Construction and design of an illumination system with high efficiency LED coating with high reflectivity.
Main activities and responsibilities	I had two main activities. The first one was a laboratory work on the technology of remote phosphor on LED in collaboration with the laboratory on the Veneto Nanoteck of Venice. The second activity was to write the SAL for the project PMI 2015. This project was about the development of new high performance white LED whit the use of the technology of remote phosphors that will be used as light source in the hood.
Dates (from-to)	December 2013 - January 2014
Name and address of employer	**UCI movies** Via Monte Amiata, 37057 San Giovanni Lupatoto Verona
Business	Movie Industry.
Occupation	My role was to do the mask.
Main activities and responsibilities	I had two main activities. The first one was to check the tickets and the entrance. The second one was to clean the theater and the bathroom.

Education and Training

Dates (from-to)	September 2014 - November 2017
Qualification	**Doctor's degree in physics**
Specialization	Experimental Physics - optoelectronic and plasmonic
	This doctoral project was centered in optoelectronic and plasmonic. Experimental measurements were done together with theoretic simulation to corroborate them. For the experimental part techniques like spin coating, Dr. blade, chemical vapor deposition (CVD), UV lithography, scanning electron microscopy (SEM), perfilometry and optical microscopy were used to fabricate and characterized the samples. For the theoretical part tools like matlab, origin, COMSOL were used to perform the simulation. Four main experiment were perform: metal nanoparticles as a coupler for waveguide, metal nanoparticles for enhancing photon-luminescence (PL) of molecule, Random laser, Plasmonic waveguide. During these experiments I learn how to couple the light and how to measure losses in waveguide and different methods to measure the PL and Absorption spectra of molecule and their quantum yield and electron - hole recombination time. The ability that i have developed during this doctoral program can be easy applied in the field of telecommunication (otical fiber, Laser, LED, etc) and informatics (optical circuit, waveguide, etc)
Organization	Photonics and Semiconductors group of the Materials Science Institute (IC-MUV) of the University of Valencia - Spain
Research project	OPTONANO - ministerial of economy and competition - 2015/2018 - UV, UPV, UCA
Coordinate Professor	Prof. Dr. Juan P. Martínez Pastor
Graduation Date	-
Vote Degree	-
Thesis work	-
Dates (from-to)	October 2010 - September 2012
Qualification	**Master's degree in physics**
Specialization	Experimental Physics - optoelectronic
	The course, taught in English, was centred on issues related to *optoelectronic*. The address courses were devoted to the study of frontier technologies and materials in the field of Electro-optic and optical applications. The hours spent in the laboratory were characterized by a work on the experimental apparatus in the first person.
Erasmus	From September 2011 to April 2012 I have done an Erasmus. In these eight months I have study at the university of Groningen (Netherlands). During this time I followed courses in the fields of Nano science, optics and organic electron. All the courses were touch in English.
Organization	University of Trento - Italy
Graduation Date	26 September 2012
Vote Degree	106/110
Thesis work	*INTEGRATED OPTICAL DISK RESONATOR FOR BIOSENSING*

The work, written entirely in English, is a study of micro optical resonators, which can be easily integrated on a chip. These devices may find practical applications in the fields of telecommunications, biological analysis, manufacture of new types of lasers and optical filters. The main objective of this my Master Thesis was to investigate optical microdisk resonator as elements in label-free biosensing devices.

Laboratory NL, University of Trento, Italy

Supervisor	Prof. Lorenzo Pavesi
Co-Supervisor	Doc. Aparicio Rebollo Francisco Javier

Dates (from-to)	September 2007 - September 2010
Qualification	**Degree in physics**
Organization	University of Trento - Italy
Thesis work	*CELLE FOTOVOLTAICHE DI PRIMA E TERZA GENERAZIONE A CONFRONTO*

A fast description of the first and third generation of solar cells was done. Where with first generation is mean the standard solar cell base on the p-n junction. While with third generation we mean solar cell with a tandem structure. Then experiments to determine the performance of this third generation were done. And at the end a comparison between first and third generation was made. This work provided me a general background in solar cell.

Supervisor	Prof. Lorenzo Pavesi
Vote Degree	105/110

Dates (from-to)	September 2002 - July 2007
Qualification	high school diploma
Organization	high school "Galileo Galilei" - Verona - Italy
Diploma grade	85/100

Language

Mother tongue(s) | **Italian**

Self-assessment
European level[*]

	Understanding		Speaking		Writing
	Listening	Reading	Spoken interaction	Spoken production	
English	B2 Independent user	B2 Independent user	B2 Independent user	B2 Independent user	B2 Independent user
Spanish	B2 Independent user	B1 Independent user	B2 Independent user	B2 Independent user	A2 Basic user

[*]*Common European Framework of Reference (CEF) level*

Personal Skills and Competences

Good knowledge in *optical resonators, optical fiber, waveguide and Laser*.

Good knowledge in the techniques of *spectroscopy*, *SEM*, *mass spectrometry*, gas and liquid *chromatography*, *Raman* spectroscopy and various techniques of analysis of optical spectra, with a fair knowledge of related equipment for these types of analyzes.

Excellent ability to work in a scientific laboratory in autonomy.

Excellent ability to work with a group of work or research.

Organizational Skill and Competences

Skilled in *problem solving* thanks to my university career and my thesis work that was carried out for about five months in a university laboratory.

During my experience in Erasmus I have acquired an excellent ability to relate to other people, even from different cultures.

Habit to make decisions and to take responsibility, developed in university.

Informatics Competences

OS	Windows
Programming	C, Matlab, Comsol
Scientific	Origin, LaTeX
Tools	Microsoft Office Suite, Open Office Suite

Hobbies and Interests

A lover of fantasy

I like going to the moves

Blood donor

Other

Car license.

Availability for work experience and intern-ships outside the region and abroad. I am interested in working as a researcher in one of the following fields: optics, photonic, electronic and green energy.

I give private lesson of mathematics and physics

In reference to the law 196/2003, I expressly authorize the use of my personal and professional information given in my resume.

2017   Mattia Signoretto

Publications

Authors	M. Signoretto, I. Suárez, V.S. Chirvony, R. Abargues, P.J. Rodríguez-Cantó and J. Martínez-Pastor
Title	"Organic waveguide couplers based on metal nanoparticle - polymer nanocomposites"
Journal	Nanotechnology, Vol. 26, no. 47, pp.47501-47210, 2015
Authors	Mattia Signoretto, Nathalie Zink-Lorre, Isaac Suárez, Enrique Font-Sanchis, Ángela Sastre-Santos, Vladimir S. Chirvony, Fernando Fernández-Lázaro and Juan P. Martínez-Pastor
Title	Effcient Optical Amplification in a Sandwich-Type Active-Passive Polymer Waveguide Containing Perylenediimides
Journal	ACS Photonics,Vol. 4, no. 1, pp. 114-120, 2017
Authors	Mattia Signoretto, Nathalie Zink-Lorre, Juan P. Martínez-Pastor, Enrique Font-Sanchis, Vladimir S. Chirvony, Ángela Sastre-Santos, Fernando Fernández-Lázaro and Isaac Suárez
Title	Purcell-enhancement of the radiative PL decay in perylenediimides by coupling with silver nanoparticles into waveguide modes
Journal	Applied physics letterers,Vol. 111, no. 8, p. 081102, 2017

Conferences

Authors	M. Signoretto; I. Suárez; V. S. Chirvony; R. Abargues; P. J.Rodríguez-Cantó and J. Martínez-Pastor
Title	Integration of metal nanoparticles in organic waveguides
Type of presentation	Poster
Conference	PTOEL 2015
National / International	National
Location	Salamanca, Spain
Year	2015
Authors	M. Signoretto; I. Suárez; V. S. Chirvony; R. Abargues; P. J. Rodríguez-Cantó and J. Martínez-Pastor
Title	Waveguide couplers based on the integration of metal nanoparticles in organic waveguides
Type of presentation	Poster
Conference	OPTICS 2015
National / International	International
Location	Valencia, Spain
Year	2015

Authors	M. Signoretto, I. Suárez, N.Zink-Lorre, E. Font-Sanchis, A. Sastre-Santos, Fernando Fernández-Lázaro, R. Abargues, P. Rodríguez-Cantó, V. Chirvony and J. Martínez-Pastor
Title	Integration of metal nanoparticles in polymer waveguides: enhancement and redirection of light in photonic structures
Type of presentation	Poster
Conference	CEN2016
National / International	National
Location	Valencia, Spain
Year	2016
Authors	M. Signoretto; I. Suárez; V. S. Chirvony; R. Abargues; P. J. Rodríguez-Cantó and J. Martínez-Pastor
Title	Concentration and redirection of light in in metal nanoparticle/polymer nanocomposites waveguides
Type of presentation	Poster
Conference	META 2016
National / International	International
Location	Malaga, Spain
Year	2016